Lehrstuhl für Biomedizinische Physik
Technische Universität München

X-ray Phase-Contrast and Dark-Field Imaging of Small Animals: Contrast Enhancement and In Vivo Imaging

Astrid Velroyen

Dissertation

March 2015

Supervisors:
Dr. Martin Bech
Prof. Dr. Franz Pfeiffer

Technische Universität München

Technische Universität München
Physik Department
Lehrstuhl für Biomedizinische Physik

X-ray Phase-Contrast and Dark-Field Imaging of Small Animals: Contrast Enhancement and *in vivo* Imaging

Astrid Velroyen

Vollständiger Abdruck der von der Fakultät für Physik der Technischen Universität München zur Erlangung des akademischen Grades eines

Doktors der Naturwissenschaften (Dr. rer. nat.)

genehmigten Dissertation.

Vorsitzender:	Univ.-Prof. Dr. M. Zacharias
Prüfer der Dissertation:	1. Univ.-Prof. Dr. F. Pfeiffer
	2. Senior University Lecturer Dr. M. Bech, Lund University, Schweden

Die Dissertation wurde am 29.01.2015 bei der Technischen Universität München eingereicht und durch die Fakultät für Physik am 06.03.2015 angenommen.

Abstract

Recently, x-ray phase-contrast and dark-field imaging have proven to show superior soft-tissue contrast and to provide complementary information compared to attenuation-based imaging. Their feasibility with a conventional incoherent x-ray tube source in combination with a Talbot-Lau interferometer has rendered this novel imaging technique a promising candidate for translation into a clinical environment. Currently, research efforts address technological challenges that have to be overcome for this translation. A first phase-contrast and dark-field small-animal computed tomography (CT) scanner with a Talbot-Lau interferometer installed on a rotating gantry had been developed and commissioned previously. In the framework of this thesis, the methodological development concerning this scanner was pursued further: A data processing and reconstruction chain was built up that includes several algorithms to cope with image artifacts arising from technological shortcomings and instabilities of the scanner. The performance of the algorithms was evaluated by means of phantom scans and a measurement of an *ex vivo* mouse sample.

Facilitated by the novel processing and reconstruction algorithms, the first *in vivo* phase-contrast and dark-field images of mice were recorded. Radiographic projection images of a healthy mouse demonstrate the complementarity of the three imaging signals. They were published in Bech et al., "In-vivo dark-field and phase-contrast x-ray imaging", Scientific Reports (2013). Moreover, first dark-field and phase-contrast CT scans were acquired of a healthy mouse and two mice with pulmonary disorders, namely emphysema and fibrosis. In particular, the iteratively reconstructed dark-field images provide excellent volumetric information on the distribution of pathological structural changes of the pulmonary tissue, without directly resolving the lung alveoli. The results were submitted for publication as Velroyen et al., "X-ray dark-field computed tomography of living mice". The demonstrated feasibility of *in vivo* projection and CT imaging opens up for a wide field of preclinical applications of the new imaging technique.

As a large fraction of today's x-ray based clinical imaging relies on the administration of specific contrast agents to the patient, the question about dedicated contrast media for the new imaging technique was addressed in this thesis. The potential of microbubbles as a scattering contrast agent for dark-field projection imaging was evaluated in *in vitro* studies, and in the presence of realistic background noise structures provided by a mouse carcass. The first study was published in Velroyen et al., "Microbubbles as a scattering contrast agent for grating-based x-ray dark-field imaging", Physics in Medicine and Biology (2013), and the second study was submitted for publication as Velroyen et al., "Ex-vivo perfusion-simulation measurements of microbubbles as a scattering contrast agent

for grating-based x-ray dark-field imaging". It was found that microbubbles scatter x-rays. However, optimization of the contrast agent as well as the setup for a possible application to living animals remains necessary.
In conclusion, the work pursued in the framework of this thesis pushed x-ray dark-field and phase-contrast imaging towards its clinical translation. The important milestone of preclinical applicability was reached and valuable insights into agent-based contrast enhancement for dark-field imaging were obtained.

Kurzzusammenfassung

In den vergangenen Jahren wurde gezeigt, dass Phasenkontrast- und Dunkelfeldbildgebung mit Röntgenstrahlung einen besseren Weichgewebekontrast als die rein schwächungsbasierte Bildgebung ermöglichen und komplementäre Informationen liefern. Dadurch, dass diese neuen Bildgebungsmodalitäten mit einer konventionellen, inkohärenten Röntgenröhre in Kombination mit einem Talbot-Lau-Interferometer umsetzbar sind, ist diese Methode vielversprechend für die Überführung in eine klinische Umgebung. Die derzeitige Forschung befasst sich mit den technologischen Herausforderungen, die für diesen Schritt bewältigt werden müssen. Im Zuge dessen wurde bereits im Vorfeld der vorliegenden Arbeit ein erster Kleintier-Phasenkontrast- und Dunkelfeldcomputertomograph (CT) entwickelt und getestet.
Im Rahmen dieser Dissertationsarbeit wurde die Methodenentwicklung hinsichtlich dieses Tomographen weiter vorangetrieben: Es wurde ein Datenprozessierungs- und Rekonstruktionsablauf erarbeitet, der verschiedene Algorithmen zum Ausgleich von Bildartefakten beinhaltet, welche von technologischen Mängeln und Instabilitäten des Messaufbaus herrühren. Die Wirksamkeit der Algorithmen wurde anhand von Phantommessungen und mit Hilfe einer *ex vivo* Maus-Probe ausgewertet.
Die neu eingeführten Prozessierungs- und Rekonstruktionsalgorithmen ermöglichten die ersten Phasenkontrast- und Dunkelfeldaufnahmen von lebenden Mäusen. Die Komplementarität der drei Bildsignale konnte anhand radiographischer Projektionsbilder einer gesunden Maus gezeigt werden. Diese wurden in Bech et al., "In-vivo dark-field and phase-contrast x-ray imaging", Scientific Reports (2013), veröffentlicht. Zudem wurden erste Dunkelfeld- und Phasenkontrast-CT-Aufnahmen von einer gesunden Maus und zwei Mäusen mit Lungenemphysem bzw. -fibrose erstellt. Insbesondere die iterativ rekonstruierten Dunkelfeldbilder bieten exzellente volumetrische Informationen über die Verteilung der pathologischen Strukturveränderungen im pulmonalen Gewebe, ohne dabei die Lungenbläschen direkt aufzulösen. Die Ergebnisse dieser Studie wurden als Velroyen et al., "X-ray dark-field computed tomography of living mice" zur Publikation eingereicht. Die gezeigte Durchführbarkeit von *in vivo* Projektions- und CT-Bildgebung erschließt ein weites Feld möglicher präklinischer Anwendungen der neuen Bildgebungsmethode.
Da ein großer Anteil der heutigen klinischen Röntgenbildgebung auf der Anwendung spezifischer Kontrastmittel im Patienten basiert, behandelt diese Arbeit die Frage nach dezidierten Kontrastmitteln für die neue Bildgebungsmethode. Das Potential von Mikrobläschen als streuendes Kontrastmittel für die Dunkelfeld-Projektionsbildgebung wurde anhand von *in vitro* Studien und in Anwesenheit

von realistischen Hintergrundrauschstrukturen in einem Mauskadaver evaluiert. Die erste Studie wurde in Velroyen et al., "Microbubbles as a scattering contrast agent for grating-based x-ray dark-field imaging", Physics in Medicine and Biology (2013), veröffentlicht. Die zweite Studie wurde als Velroyen et al., "Ex-vivo perfusion-simulation measurements of microbubbles as a scattering contrast agent for grating-based x-ray dark-field imaging" zur Publikation eingereicht. Es konnte gezeigt werden, dass Röntgenstrahlen an Mikrobläschen gestreut werden. Allerdings ist für die Anwendung am lebenden Tier eine weitere Optimierung sowohl des Kontrastmittels als auch des Messaufbaus notwendig.

Diese Dissertationsarbeit hat dazu beigetragen, die Röntgen-Dunkelfeld- und Phasenkontrastbildgebung weiter in Richtung klinischer Translation voranzutreiben. Mit der präklinischen Anwendbarkeit der Methode wurde ein wichtiger Meilenstein in diesem Prozess erreicht. Zudem konnten wertvolle Erkenntnisse über die Kontrastverstärkung durch Kontrastmittel für die Dunkelfeldbildgebung gewonnen werden.

Table of Contents

Chapter 1

Introduction

This chapter provides a brief motivation of the work performed in the context of this thesis. Moreover, an overview over the contents of the following chapters is given.

1.1 Motivation

Since their discovery by Wilhelm Conrad Röntgen in 1895, x-rays have found a broad range of applications because of their ability to penetrate most kinds of materials. Aside from their use in industry and research, x-rays are in particular utilized to depict inner structures of the human body in daily practice of diagnostic medical imaging.
In clinical application, two-dimensional radiographic projection images as well as three-dimensional volume images of the human body acquired by computed tomography (CT) are obtained using x-rays. Up until now, the contrast generation in both of those imaging modalities solely relies on the varying degree of attenuation of x-rays occurring in different types of tissue. Differences in density and elemental composition of the tissues are the cause for the variance in x-ray transmission. For example, calcium-rich skeletal structures absorb x-rays more strongly than muscle tissue, resulting in bones being highly visible in a conventional x-ray image. However, different soft-tissue types, such as the inner organs, tumors or cartilage, usually contain only minor density differences, so that the contrast in soft tissue generated by x-ray attenuation is poor. This poses limitations on the detectability of pathological changes in soft tissue, for example in breast imaging. Moreover, some disorders cause drastic structural changes, but only weak variation in the overall amount of attenuating tissue and are therefore

difficult to detect on conventional x-ray images, for example pulmonary diseases such as emphysema or fibrosis.
More advanced x-ray imaging techniques that exploit physical phenomena other than mere attenuation are the phase-sensitive imaging methods. Here, image contrast is generated from perturbations of the x-ray wave front that are caused by a phase shift imposed on the x-ray wave when it traverses the material. Generally speaking, materials with elemental compositions containing low atomic numbers, as found in body tissue, usually exhibit stronger differences in phase-shifting ability than in the attenuation of x-rays. Consequently, in many cases, phase-sensitive techniques provide an improved soft-tissue contrast and complementary information, compared to conventional attenuation-based imaging. Moreover, some phase-sensitive techniques also give access to information on the location of x-ray scattering at interfaces in the sample, thus adding structural information to the imaging output.
Because the phase of a wave front cannot be measured directly, the imaging method in question has to provide a translation from phase to intensity differences. There are various approaches to measure the phase shift, or equivalently the refraction, of x-rays passing through matter. They can be mainly classified into free-space propagation techniques (Snigirev et al., 1995; Cloetens et al., 1999), analyzer-crystal–based methods (Davis et al., 1995; Chapman et al., 1997) and interferometric methods (Bonse and Hart, 1965; Momose, 2003). For a concise review of the different approaches, the reader is referred to Bech (2009).
The method applied in this thesis belongs to the latter approach and is called *grating-based Talbot-Lau interferometry* (Weitkamp et al., 2005; Pfeiffer et al., 2007a, 2008). Here, a grating is used as an optical element to generate an interferometric pattern as a spatial reference. The changes of this pattern induced by a phase-shifting, scattering, and attenuating object in the beam can be measured with a conventional imaging detector and a rasterizing mask. The contrast types generated from the measured physical quantities in addition to attenuation-based contrast are called *phase contrast*, which maps the refraction in the sample, and *dark-field contrast*, which shows the structures that induce small-angle x-ray scattering. One of the advantages of Talbot-Lau interferometry over the other phase-sensitive x-ray imaging methods is its feasibility with conventional polychromatic, incoherent x-ray tube sources. As this allows for reasonably high flux and short detector exposure times, it renders Talbot-Lau interferometry a promising candidate for a possible translation into the clinical environment.
When placing the technique in question into context with existing medical whole-body imaging techniques, one has to note that excellent soft-tissue contrast can also be achieved in the clinics by use of magnetic resonance imaging (MRI). Additionally, MRI has the advantage that it does not expose the patient to any sig-

nificant dose of potentially harmful radiation, in contrast to x-ray CT. However, drawbacks are a limited spatial resolution (inferior to the submillimeter resolution in CT), long scan times, and high cost. Phase-sensitive x-ray imaging may have the potential to ultimately provide both the excellent spatial resolution of CT and good soft-tissue contrast, however with the drawback of the use of ionizing radiation.

The first benchmarking experiments of grating-based interferometry with highly brilliant synchrotron radiation sources showed that phase-contrast and dark-field imaging (PCI, DFI) provide improved soft-tissue contrast and complementary information on small biomedical specimens. Meanwhile, studies showed successful identification of disorders where PCI or DFI gave access to additional information compared to conventional attenuation-based imaging. Also, the technological developments have advanced further towards clinical implementation. In the course thereof, a preceding doctoral thesis by Tapfer (2013) dealt with the development and commissioning of a first PCI and DFI computed tomography (CT) scanner with stationary sample and rotating gantry, which is a necessary prerequisite for imaging of living specimens. The commissioning results included an evaluation of the stability of the interferometer on the rotating gantry and successful quantitative imaging of a calibration phantom with the scanner. As a human-size CT scanner is a complex and highly-optimized system and several technological limitations still apply to PCI and DFI, this CT system was laid out for small rodents. Nonetheless, it serves for two important scientific purposes: First, as challenges posed by the rotating gantry onto the interferometric setup are present, but can be overcome, the experiences may serve as a starting point for the transfer to human-size rotating gantry systems. Second, PCI and DFI with living animals at the scanner opens up a wide field of possible preclinical research. Medical research strongly relies on the investigation of diseases and therapeutic approaches in small-animal models. Thus, complementary information provided by PCI and DFI possibly provides novel opportunities in this area. Many disorders have been studied on excised and/or fixated *ex vivo* samples with PCI and DFI before, but some pathological cases can only be studied in a reliable manner *in vivo*, or may require longitudinal disease monitoring, i.e. repeated scans of the same animal specimen over a longer period of time such as days or weeks.

The present work has to be seen in the context described above, as it directly follows up on the work of Tapfer (2013). The first and main part of this thesis is dedicated to the quest of overcoming setup limitations by algorithmic signal-retrieval corrections and obtaining a higher robustness in processing the data that was acquired by the PCI/DFI rotating-gantry CT scanner, and consequently performing the first *in vivo* imaging, both in radiography and CT. Imaging of living animals with Talbot-Lau interferometry and compatible radiation dose and ac-

quisition duration represents one of the remaining milestones before translation of PCI and DFI into the clinics.
The second part of this thesis is also to be understood in the context of the development of PCI and, more importantly, DFI towards their (pre-)clinical applicability. In conventional x-ray CT imaging, about half of the clinical CT scans are performed with the administration of contrast agents to the patients in order to enhance the achieved contrast by increased absorption of x-rays due to the injected pharmaceutical. With a new contrast modality at hand, the search for further improvement of the provided image contrast by a dedicated agent is the logical next step. Therefore, dark-field contrast enhancement by the use of microbubble-based contrast agents is investigated.
For in-depth introductions into the two specific fields covered by this thesis and a placement of this work into the context of other existing studies in the areas, the reader is referred to the individual introduction sections of the main results chapters, i.e. Section 3.1 and 4.1.

1.2 Outline

In Chapter 2, the theoretical background necessary to understand the applied imaging methods is presented. First, the basic properties of x-rays and the underlying physical phenomena of interaction between x-rays and matter are introduced. Second, the means of x-ray generation and detection that are utilized in this work are described briefly. Third, the principle of grating-based interferometry and its implementation with polychromatic and divergent illumination is outlined. Moreover, the basics of tomographic reconstruction with a filtered backprojection algorithm for parallel and divergent beam geometry are provided, and a short introduction to the principle of iterative reconstruction is given. At last, a concise overview over the use of contrast agents in the clinics is provided.
Chapter 3 is the first one of two chapters presenting the scientific results of this thesis. Its methodological part deals with advanced signal recovery algorithms to overcome shortcomings of the small-animal CT scanner and the resulting artifacts. Effects and improvements of the algorithms are demonstrated on phantoms and an *ex vivo* mouse specimen. Furthermore, the chapter contains the most important scientific contribution of this thesis: the first *in vivo* imaging results of phase-contrast and dark-field imaging with a Talbot-Lau interferometer. Radiographic imaging of a healthy mouse, as well as CT imaging of a healthy mouse and two mice with pulmonary disorders are presented.
In Chapter 4, three *in vitro* studies on the applicability of microbubbles as a dedicated x-ray dark-field contrast agent are presented. Here, first existing preclinical

and clinical microbubbles are investigated. Subsequently, a study with an experimental contrast agent in the context of subtraction imaging with a mouse carcass as background structure is shown. The third study investigates the question of the influence of coating of the microbubbles onto the measured signal.
Chapter 5 concludes this work with a summary of the main results and a short outlook on further research perspectives.

Chapter 2

Theoretical background

When x-rays were first discovered by W. C. Röntgen in 1895 (Stanton and Röntgen, 1895), he noticed certain similarities between the new kind of rays and light in the visible or ultraviolet regime. However, as his approaches to prove refraction of x-rays failed, he was not sure about their nature, which lead him to name them 'X-Strahlen'. Today, we know that x-rays are part of the spectrum of electromagnetic waves, and that Röntgen's failed attempts to demonstrate their refraction were due to their rather high energies and consequently minimal refraction angles and an index of refraction smaller than unity in contrast to that for visible light. Since the technique that this thesis is built on exploits the various means of interaction between x-rays and matter, their properties and interaction principles are briefly summarized in Section 2.1. Section 2.2 provides a short introduction to the relevant mechanisms of x-ray generation and detection. The working principle of grating-based interferometry and its signal retrieval are introduced in Section 2.3. In Section 2.4, basic principles and algorithms for tomographic reconstruction are presented. A small introduction to the current use and future trends of contrast agents in x-ray imaging is given in Section 2.5.

2.1 Properties of x-rays and their interaction with matter

As x-rays are electromagnetic waves, they can be described as such by oscillating electric and magnetic fields, propagating through space. In the following, description and formulas are adapted from Als-Nielsen and McMorrow (2011) and Willmott (2011). For simplicity, only the electric field is considered here. A

propagating plane wave at point $\mathbf{r}$ in space can be denoted by:

$$\psi(\mathbf{r}, t) = \boldsymbol{\varepsilon}\, E_0\, e^{i(\mathbf{k}\cdot\mathbf{r}-\omega t)}, \tag{2.1}$$

where E_0 denotes the amplitude of the electric field vector and $\boldsymbol{\varepsilon}$ its polarization direction. The spatial (regarding $\mathbf{r}$) and temporal (regarding t) variation of the propagating wave is included in the expression $i(\mathbf{k}\cdot\mathbf{r}-\omega t)$. $\mathbf{k}$ denotes the wave vector along the direction of propagation, and ω the oscillation frequency. The wave vector is connected to the wavelength λ via the wave number $|\mathbf{k}| = k = 2\pi/\lambda$. This classical description of a linearly polarized, electromagnetic plane wave is complemented by the quantum-mechanical particle description. Here, x-rays are seen as quantized energy portions, i.e. photons with an energy $\hbar\omega$ and a momentum $\hbar\mathbf{k}$, with $\hbar = h/2\pi$ and $h \approx 4.135667516 \cdot 10^{-15}\text{eV}\cdot\text{s}$ being the Planck constant. In common practice, classical and quantum-mechanical description are chosen freely depending on which one provides the clearest understanding of the problem at hand.
X-rays have wavelengths in the order of 1 Ångström, or in the energy range between 1 keV and 100 keV. In this energy regime, the main interactions of x-rays with matter are absorption, and elastic and inelastic scattering.

2.1.1 Absorption, refraction, and scattering

The total interaction cross section of x-rays with matter in the energy range of interest in this work can be described as follows:

$$\sigma_{\text{Total}} = \sigma_{\text{Photo}} + \sigma_{\text{Rayleigh}} + \sigma_{\text{Compton}} \tag{2.2}$$

As an example, the interaction cross sections of carbon over a wide photon energy range are given in Figure 2.1.
σ_{Photo} denotes the interaction cross section for the *photoelectric effect*, which is the common description of absorption of photons in the particle picture: Here, the energy of the incoming photon is fully absorbed by an electron close to the core of an atom. The electron, called photoelectron, is expelled from its shell. Only photons with energies above the binding energy of the electron in the atom contribute to photoelectric absorption with a certain cross section. This results in the shell-specific edges in the absorption cross section at characteristic energies, see Figure 2.1 blue line.
σ_{Rayleigh} stands for the interaction cross section for elastic scattering of x-rays. Elastic scattering can be understood in the classical picture as a process where the electric field of the incoming x-ray wave excites an electron to oscillate harmonically. Thereby, the electron itself emits a wave with identical wavelength, so

the energy is preserved. The form of the scattered intensity distribution follows the dipole radiation. This process is described by *Thomson scattering* for free electrons and *Rayleigh scattering* for electrons in a bound state.
Above approximately 30 keV, the contribution of inelastic scattering, denoted as *Compton scattering*, becomes relevant and is therefore considered in the cross section by σ_{Compton}. Here, the energy of the incoming photon is partially transferred to the electron, resulting in the emittance of a photon with longer wavelength. This process requires a description in the relativistic particle picture with conservation of energy and momentum. The spatial distribution of the scattered intensity is described by the Klein-Nishina formula given for example in Weinberg (1995).

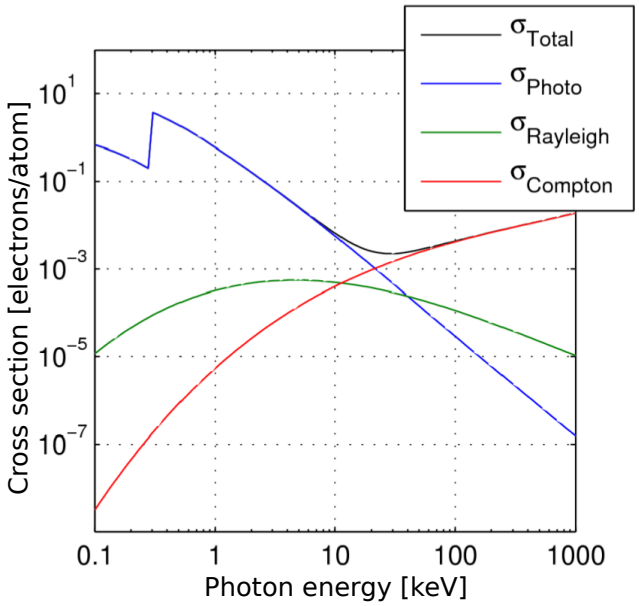

Figure 2.1: The interaction cross sections for photoelectric effect σ_{Photo}, Rayleigh scattering σ_{Rayleigh}, Compton effect σ_{Compton}, and the total interaction cross section σ_{Total} are shown for carbon. The graph is adapted from Chabior (2011).

For the experiments performed in this work, the elastic Rayleigh scattering is what contributes to the phase-contrast and dark-field signal. Photoelectric absorption is the main cause for the attenuation signal, however scattering also contributes to it.

The quantitative effect of absorption and scattering of x-rays can be described phenomenologically via the *complex index of refraction*:

$$n = 1 - \delta + i\beta. \tag{2.3}$$

Considering the propagation of the plane electromagnetic wave introduced in

Equation 2.1 in direction of z through a medium with refractive index n, we obtain:

$$\psi_m(z,t) = E_0\, e^{i(nkz-\omega t)} \tag{2.4}$$

$$= E_0 \cdot e^{i(kz-\omega t)} \cdot e^{-k\beta z} \cdot e^{-ik\delta z}. \tag{2.5}$$

It can be easily seen that the amplitude E_0 together with the first exponential expression constitutes the respective wave in vacuum, which will be called $\psi_\mathrm{v}(z,t)$. The second exponential term denotes an amplitude decay, whereas the third exponential expression introduces a relative phase shift. Thus, δ describes the elastic processes, i.e. the refraction that an x-ray undergoes when passing through matter, while β is responsible for the attenuation.

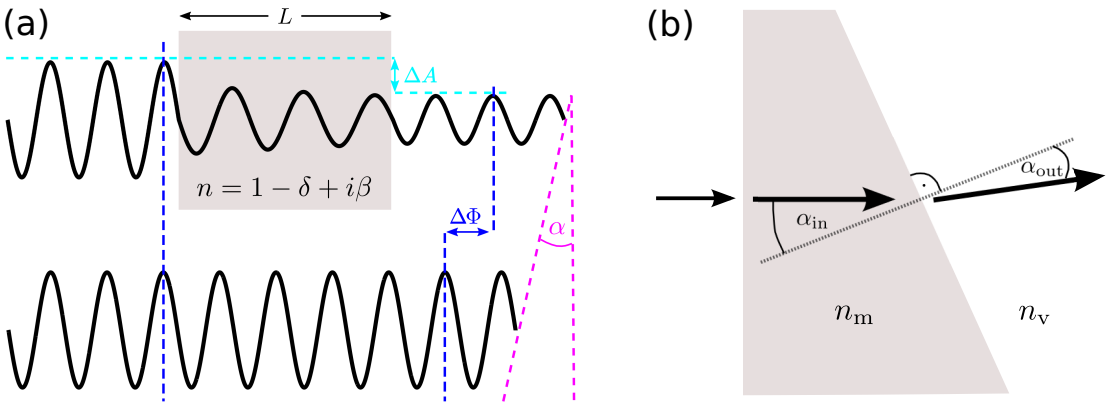

Figure 2.2: (a) Attenuation and phase shift of a wave passing through a material with complex refractive index n. The amplitude is decreased by ΔA, and the phase is shifted by $\Delta\Phi$, resulting in a wave front inclined by α at edges or areas where the sample thickness changes. (b) Refraction of x-rays when passing through a wedge with refractive index n_m. The ray enters the material orthogonal to the first surface. Refraction happens when the x-ray leaves the material through the inclined surface. With x-rays $\alpha_\mathrm{out} < \alpha_\mathrm{in}$, with visible light $\alpha_\mathrm{out} > \alpha_\mathrm{in}$. n_v is the refractive index of vacuum. Figures adapted from Tapfer (2013).

Phase shift and refraction: The real part of the complex refractive index $1-\delta$ is smaller than unity and contains the *refractive index decrement*:

$$\delta = \frac{2\pi\rho_\mathrm{e} r_0}{k^2}, \tag{2.6}$$

where $r_0 = 2.82 \cdot 10^{-5}$Å denotes the Thomson scattering length. It can be understood as the ability of an electron to scatter an x-ray and can be pictured by

being the radius of a free electron in the classical picture. Equation 2.6 shows that δ represents a direct measure for the electron density ρ_e of the traversed material material. Via the wavenumber k, its energy dependence is $\delta \sim E^{-2}$. With $\rho_\mathrm{e} = N_i \cdot Z$ and N_i being the number of atoms per unit volume, δ depends linearly on the atomic number Z.
From Equation 2.5 it is apparent, that δ causes a phase shift of the wave in the medium, relative to the wave propagating outside of the material in direction of z, with a phase velocity $c/(1-\delta)$ larger than the speed of light c. The phase shift $\Delta\Phi$ is given by (Paganin, 2006):

$$\Delta\Phi = \delta\, k\, z. \tag{2.7}$$

As Figure 2.2a illustrates by the line through the wave crests, this results in a change of direction of the wave front, i.e. a refraction of the x-ray, at edges or areas where the sample thickness changes. A small-angle approximation yields the corresponding angle α by which the x-ray direction changes, when the x-rays traverse an object that is extended in the direction x perpendicular to the propagation direction (Paganin, 2006)*:

$$\alpha = \frac{\lambda}{2\pi}\frac{\partial\Phi}{\partial x}. \tag{2.8}$$

The method used in this work measures the refraction angle of the x-rays, which means the first derivative of the phase change is obtained.

Via *Snell's law*, the refraction angle α_r for a wedge (see Figure 2.2b) with refractive index n_m can be estimated:

$$\begin{aligned} n_\mathrm{v}\,\sin\alpha_\mathrm{in} &= n_\mathrm{m}\,\sin\alpha_\mathrm{out} && (2.9)\\ \alpha_\mathrm{in} &\approx n_\mathrm{m}\,\alpha_\mathrm{out} && (2.10)\\ \alpha_\mathrm{r} &= \alpha_\mathrm{out} - \alpha_\mathrm{in} && (2.11)\\ &\approx \alpha_\mathrm{in}\,(n_\mathrm{m}-1) && (2.12)\\ &\approx -\delta\,\alpha_\mathrm{in}. && (2.13) \end{aligned}$$

Here, the small-angle approximation $\sin\alpha \approx \alpha$ and the refractive index of vacuum $n_\mathrm{v} = 1$ was used. See Figure 2.2b for the definition of angles α_in and α_out. For the energy range of x-rays, δ covers a regime from of 10^{-8} to 10^{-6} (Chantler, 1995), which leads to typical refraction angles in the nano-radian or micro-degree range or smaller (Bech, 2009; Tapfer, 2013). This illustrates how challenging it is to experimentally measure this physical quantity, explaining Röntgen's first failed attempts in 1895.

*Here, the projection approximation was applied, i.e. it was assumed that x-rays travel in a straight path through a medium and that multiple scattering events can be neglected (Paganin, 2006).

Attenuation: While $e^{-k\beta z}$ describes the attenuation of the wave's amplitude, what is measured is the intensity decay of the wave with the original incoming intensity I_0:

$$\frac{I_\mathrm{m}(z)}{I_0} = \frac{|\psi_\mathrm{m}(z,t)|^2}{|\psi_\mathrm{v}(z,t)|^2} = e^{-2k\beta z}. \tag{2.14}$$

With the relation

$$\beta = \frac{\mu}{2k}, \tag{2.15}$$

the linear attenuation coefficient $\mu = 2k\beta$ is defined and the *Lambert-Beer law* for the attenuation of a wave that travels a distance z through the medium is obtained:

$$I_\mathrm{m}(z) = I_0\, e^{-\mu z}. \tag{2.16}$$

The linear attenuation coefficient μ, as commonly measured, contains contributions from absorption as well as scattering processes:

$$\mu = \mu_\mathrm{Photo} + \mu_\mathrm{Rayleigh} + \mu_\mathrm{Compton}. \tag{2.17}$$

Therefore, the energy and atomic number dependency of β is more complicated over the whole range of energies than that of δ, as the various interaction mechanisms contribute differently. Above all absorption edges, the dependency can be approximated by $\beta \sim \frac{Z^4}{E^4}$ (Als-Nielsen and McMorrow, 2011), as long as the Compton contribution is still small. Consequently, δ decreases less quickly with energy than β or μ, which allows for increased image contrast especially for low atomic numbers as present in biomedical specimens at higher energies. This is only valid at energies below approximately 40 keV, where the Compton contribution is still negligible.

In the application cases in this thesis, the x-rays traverse multiple materials on their way through a sample. In this case, Equations 2.7, 2.8, and 2.16 require an integral extension, so that the following set of equations is gained:

$$\Delta\Phi = k \int \delta(x,z)\,\mathrm{d}z, \tag{2.18}$$

$$\alpha = \frac{\partial}{\partial x} \int \delta(x,z)\,\mathrm{d}z, \tag{2.19}$$

$$I_\mathrm{m}(z) = I_0\, e^{-\int \mu(x,z)\,\mathrm{d}z}. \tag{2.20}$$

2.1.2 Coherence

One property of x-rays that is crucial for interferometric imaging as applied in this work, is their degree of coherence. Coherent waves are waves with the same wavelength that are 'in phase' with each other, while propagating in the same direction. As this is an ideal state that no real x-ray source can fulfill, the concept of longitudinal and transverse coherence length as a measure for coherence is introduced according to the definition by Als-Nielsen and McMorrow (2011).

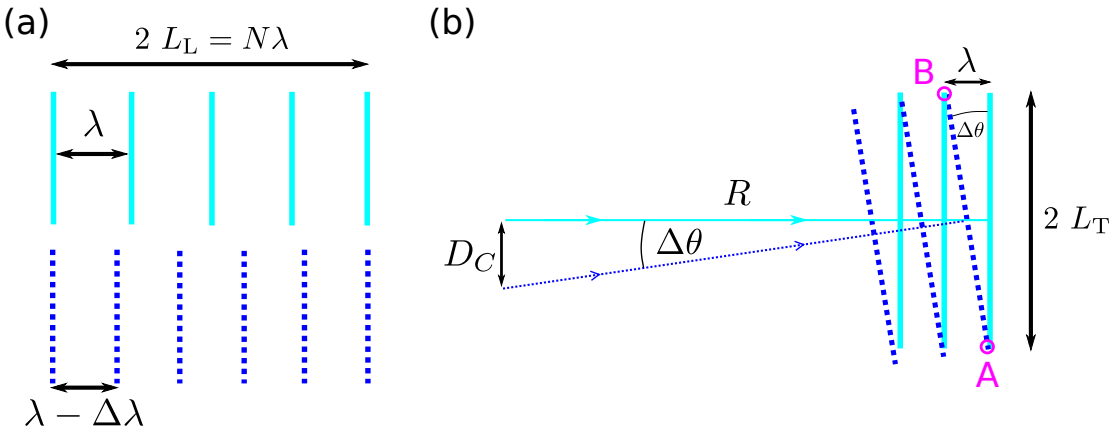

Figure 2.3: (a) Illustration of the concept of the longitudinal coherence length L_L. Two plane waves with wavelengths λ and $\lambda - \Delta\lambda$ are in phase again after propagating $2L_L$. (b) Illustration of the concept of the transverse coherence length L_T. Two plane waves with identical wavelengths have propagation directions differing by $\Delta\theta$, because they originate from two points that are a distance D_C apart in the source. After L_T along the wave front they are exactly out of phase. Figures adapted from Als-Nielsen and McMorrow (2011).

We assume two waves whose wavelengths are λ and $\lambda - \Delta\lambda$ with $\Delta\lambda$ being small, propagating in the same direction. The distance between the point where they are exactly in phase to the point where they are exactly inversely phased is called longitudinal (or temporal) coherence length L_L. After twice this distance, the waves are in phase again (see Figure 2.3(a)):

$$2\,L_L = N \cdot \lambda \quad = (N+1)\,(\lambda - \Delta\lambda) \tag{2.21}$$

From the second equation it follows that $(N+1)\,\Delta\lambda = \lambda$ and thus $N \approx \lambda/\Delta\lambda$. Consequently, the longitudinal coherence length can be written as

$$L_L = \frac{1}{2}\frac{\lambda^2}{\Delta\lambda}. \tag{2.22}$$

The transverse (or spatial) coherence length L_T can be deduced from the scenario of two waves with identical wavelength, but slightly diverging propagation direction. The transverse coherence length denotes the distance one has to travel from

a point A where the waves are exactly in phase along the wave front to a point where they are exactly out of phase. At point B they coincide and are exactly in phase again. From Figure 2.3(b), we can see that $\lambda = 2\,L_\mathrm{T}\,\Delta\theta$, with $\Delta\theta$ being the inclination angle between the two propagation directions. In reality, the cause for spatially incoherent waves is often the extended size of the source. If the two waves originate from two points in the source that are the distance D_C apart and the source is located at a distance R, we obtain $\Delta\theta = D_C/R$ and finally yield

$$L_\mathrm{T} = \frac{\lambda}{2}\frac{R}{D_C}. \tag{2.23}$$

In consequence, a small source size and a large distance between source and point of interaction act in favor for the coherence.

2.1.3 Free-space propagation

As documented by Als-Nielsen and McMorrow (2011), Chapter 9, different x-ray imaging methods can be classified by the distance R between the x-ray detector and the object to be imaged, and the size a of the detail to be resolved with the wavelength λ. In conventional attenuation-based x-ray imaging, as e.g. so far applied in the medical field, the detector is placed right behind the sample in the so-called contact region. It is characterized by $R \ll a^2/\lambda$. In this region, attenuation of x-rays is the only relevant cause for contrast generation. However, when the distance between object and detector is increased, the x-rays that have traversed the sample propagate freely through space before being detected. In this case, diffraction phenomena in the form of interference between undeviated and refracted x-ray waves occur and contribute to the recorded signal. In their description, it is distinguished between far-field or Fraunhofer regime ($R \gg a^2/\lambda$) and near-field or Fresnel regime ($R \approx a^2/\lambda$). In the far-field, the waves can be approximated as plane and parallel, whereas the near-field demands a more accurate description.
The method used in this work, grating-based interferometry, requires a certain distance between source and detector plane, which corresponds to the Fresnel regime. Therefore it should be noted that, in a complete theoretical description of the method, free-space propagation of the x-ray waves has to be considered using the Huygens-Fresnel principle, where the wave front is described by a superposition of spherical wavelets originated by point sources distributed on the wave front at an earlier point. It can be described by the Fresnel diffraction integral:

$$\psi(x,y,z,t) = \frac{e^{i(kz-\omega t)}}{i\lambda z}\int\int \psi(x_0,y_0,0)\, e^{\frac{ik}{2z}[(x-x_0)^2+(y-y_0)^2]}\,\mathrm{d}x_0\mathrm{d}y_0. \tag{2.24}$$

x_0 and y_0 are the x and y values in the plane where $z = 0$. Hence, the propagation behind an object can be expressed as a convolution of the wave-function exiting the object with a so-called propagator function $h(x, y) = (e^{ikd}/i\lambda d)\, e^{ik(x^2+y^2)/2d}$. By using the convolution theorem, the propagation can be further calculated by simple multiplication of the Fourier transforms of the wave function and the propagator.
However, a detailed derivation and the necessary approximations of the free-space propagation theory is beyond the scope of this thesis. It can be found in Goodman (1996) and was also comprehensively summarized by Bech (2009). It shall only be mentioned here that the theory of free-space propagation is the basis for the calculation of the intensity distributions caused by interference as presented in Section 2.3.1 on the Talbot effect and for the wave-optical simulation package by Malecki et al. (2012) that was used to simulate dark-field signal of bubbles shown in Chapter 4.

2.2 Generation and detection of x-rays

The basic components of an x-ray imaging system are a source that generates x-rays and a detector that measures the x-ray intensity behind the object that is to be imaged. A review on the various ways of x-ray generation and source types can be found in Schleede (2013). The working principles of different types of photon detectors are given for example by Willmott (2011). Here, only a short introduction to the devices that are found in the experimental setup used in this thesis is given: a conventional x-ray tube and an integrating detector.

2.2.1 X-ray tube

In a conventional x-ray tube source, electrons are emitted from a glowing filament, the cathode, and accelerated towards the anode (Figure 2.4a), also referred to as the target. When the electrons hit the target material, they are decelerated by atoms in the target, which gives rise to x-rays with a broad energy spectrum – called *Bremsstrahlung*. The maximum energy of the spectrum is defined by the highest kinetic energy of the electrons $E_{\mathrm{kin}}^{\mathrm{max}} = e\,U$ with $e = 6.02{\cdot}10^{-19}$ C being the elementary charge and U being the acceleration voltage in the tube. Additionally to the continuous deceleration process, x-ray fluorescence occurs, when a bound electron relaxes to its ground state after the atom was excited by an incoming electron. The fluorescence appears as characteristic spectral lines with significantly higher intensity than the broad Bremsstrahlung spectrum (Figure 2.4b).

The efficiency of converting kinetic energy into Bremsstrahlung is below 1 % and scales with the atomic number Z of the anode material. The largest part of the energy is lost to heat, which is the limiting factor to the flux of an x-ray tube. Advanced cooling systems as well as rotating anodes, where the heat dissipation is spread over a larger target area, have been developed to cope with this drawback. Typical anode materials are tungsten and molybdenum due to their high atomic numbers and high melting points.
The focal spot size of the tube, which contributes to the blurring in an imaging system, is defined by the spot where the electrons impinge on the target. In microfocus tubes, this spot is limited to a few micrometers with the help of electron focusing, allowing for a high spatial resolution, but strongly limiting the flux and increasing exposure times.
Due to relatively low cost and high robustness, conventional x-ray tubes are widely used in medical imaging systems as well as in industry and research applications.

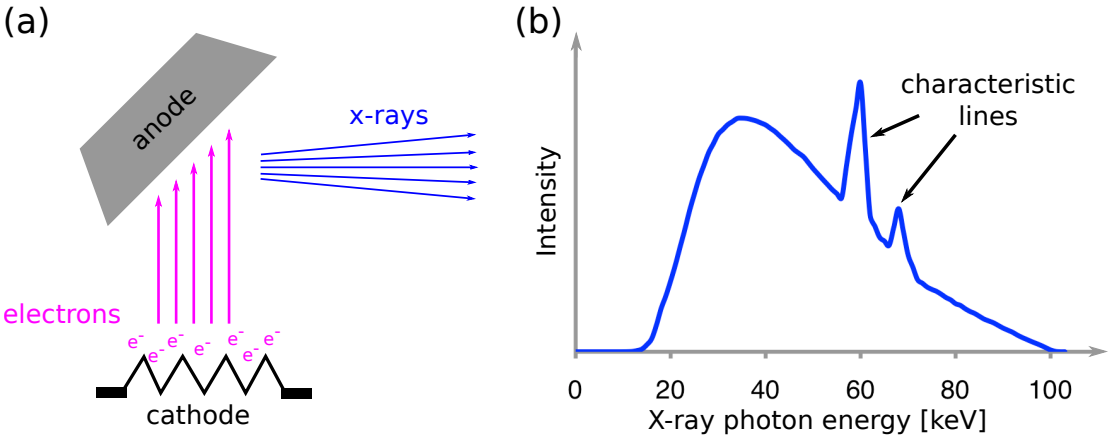

Figure 2.4: (a) Sketch of the working principle of an x-ray tube source. Electrons are emitted from the cathode and accelerated towards the anode. Interaction with the anode material generates x-rays. Figure adapted from Tapfer (2013). (b) X-ray photon energy spectrum of an x-ray tube with tungsten target, operated at a peak voltage of 100 kV. The characteristic lines are at $K_\alpha = 59$ keV and $K_\beta = 67$ keV.

2.2.2 X-ray detector

Different types of x-ray detectors apply a wide variety of principles to register impinging photons. The most important x-ray detectors that are relevant for imaging purposes can be roughly classified into so-called photon-counting detectors, which actually register single photons, and integrating detectors, which sum up the contributions from several photons that arrive in a certain time to generate

an electronic signal. Ehn (2013) provides an introduction on the working principle of photon-counting detectors. The working principle of integrating detectors shall be described here, following the textbook by Willmott (2011), as this detector type is employed in the setup used in this work.
An integrating detector usually consists of a scintillator layer, which converts the impinging x-rays into visible light, and a light-sensitive sensor, for example a charge-coupled device (CCD) camera (Strauss et al., 1988; Smith, 2009), to generate the electronic signal. The scintillator material is usually a salt or metal oxide doped with a high atomic-number material. The energy of an impinging x-ray photon is absorbed and utilized to electronically excite an atom of the scintillator material. The energy is transferred to a nearby excited state of the dopant, which then efficiently relaxes to a lower excited state via processes that do not include photon emission. The ultimate relaxation to the ground state occurs by emission of a photon of the visible or ultraviolet spectrum. The energy conversion of the scintillation process is illustrated in Figure 2.5a.

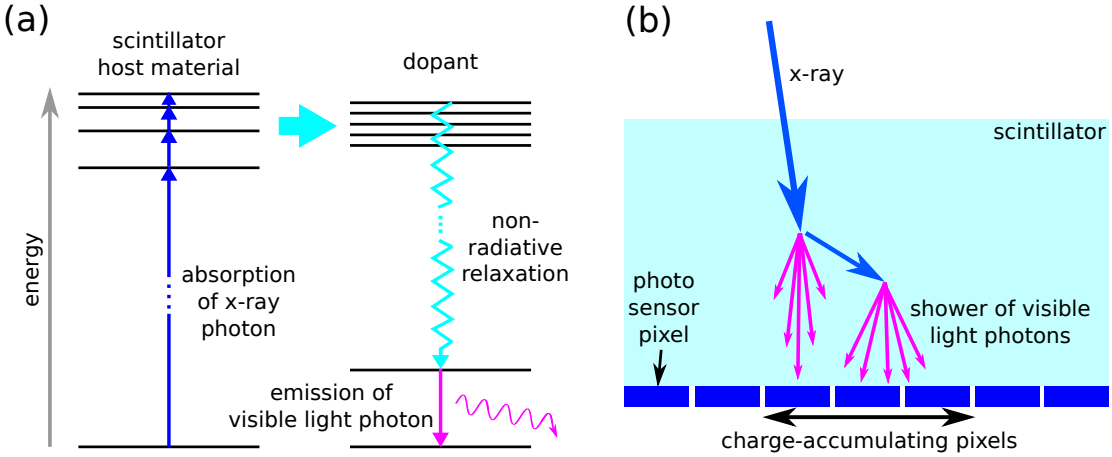

Figure 2.5: (a) Simplified energy level scheme of the scintillation process within an inorganic crystal. The energy of an x-ray absorbed in the host material is transferred to the dopant, which relaxes via non-radiative decay to a lower energy state. From there, relaxation happens via the emission of a (near-)visible light photon. Figure adapted from Willmott (2011). (b) Possible causes of blooming in the detection process: The x-ray can interact at several locations in the crystal and deposit energy in smaller portions. Moreover, the shower of generated light photons widens the area in which the photo sensor pixels are activated.

The generated light is then detected by a two-dimensional photosensitive pixel array, which converts the entering photons via the photoelectric effect into an electronic charge that is proportional to the number of incoming photons. This charge is consequently read out and converted into a digital signal that constitutes the image. As the detector always sums up the contributions from several photons impinging during a certain time period, it is called 'integrating'.

Several phenomena during the x-ray detection process can lead to a reduced resolution of the imaging system, which is referred to as 'blooming'. It denotes that the final resolution limit of the imaging system is larger than the size of one pixel in the photosensitive array. The blurring of an ideal point-like source or object on the detector is described by the detector point-spread function (PSF) (Figure 2.6). Usually, the processes in the scintillator dominate the broadening of the detector PSF: First, multiple scattering of the x-ray photon across the depth of the scintillator layer before final energy absorption can occur, which renders the location of the detection imprecise. Second, the visible-light photons are emitted into all directions, so that a cone-shaped shower of photons is detected (Fig. 2.5b). Additionally, the width of this shower depends on the interaction depth in the active layer, and therefore on the x-ray energy. Charge sharing between pixels (for details, see Knoll (2010)) in the photosensitive array can add to those effects.
The overall blurring in the imaging system is described by the system point-spread function. In addition to the detector contribution, it includes blurring induced by an extended source size.

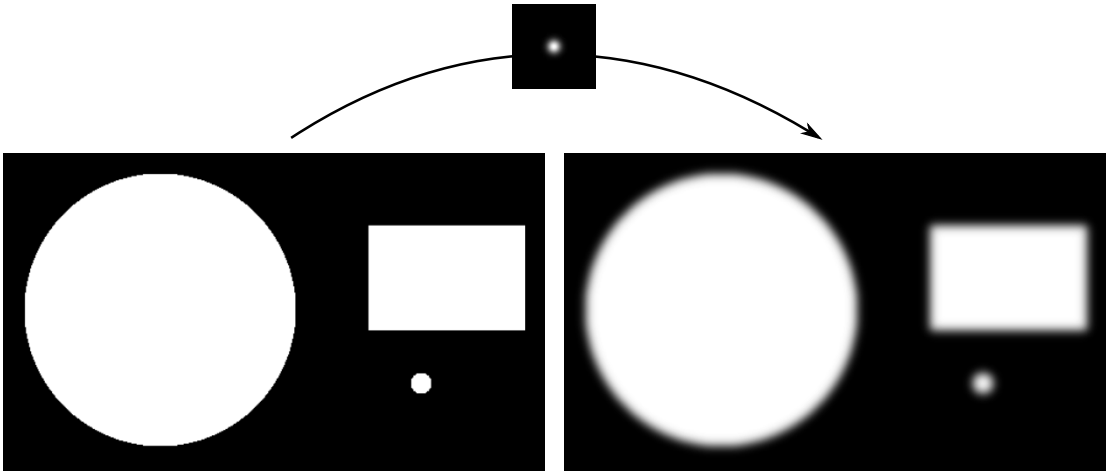

Figure 2.6: Illustration of blurring induced by an extended detector point-spread function. The sharp objects (left figure) are visibly blurred (right figure) due to blooming effects that are described by a point-spread function. In this example, the point-spread function is a two-dimensional Gaussian function (top figure).

2.3 Grating-based interferometry

X-ray phase-contrast imaging exploits the refractions that the x-rays undergo when traversing matter, whereas dark-field imaging creates an image contrast

from ultra small-angle scattering. As mentioned in the previous section, the refraction angles of x-rays are very small, which makes them difficult to be measured directly. Therefore, an extended spatial reference pattern is used, and the refraction is measured via the pattern's relative shift as induced by a sample. The method applied in this thesis, grating-based interferometry, uses a periodic grating structure to force an interference pattern upon the x-ray beam that is used to illuminate the sample. The local distortion of the pattern induced by the sample is measured relative to the original pattern without sample in the beam. From this, attenuation, phase and dark-field signal can be retrieved.
In this section, the underlying physical principles of grating-based interferometry, the necessary optical elements in the beam path, and the measurement procedure and signal extraction are introduced. Furthermore, the influence of polychromaticity and magnifying geometry are explained, as they occur in the setup used for the experiments in this thesis.

2.3.1 The Talbot effect

In 1836, Sir Henry Fox Talbot discovered that a periodic structure such as a grating, positioned in the path of light, creates images of itself at certain distances behind the grating (Talbot, 1836) without the use of any optical components. The self-imaging phenomenon, which was named *Talbot effect* after its discoverer, can be explained by interference of coherent waves and can be mathematically described by Fresnel propagation in free space of a periodically modulated wave front. The periodic modulation can be imposed on the wave front by a grating where the bars either absorb the wave or shift its phase. Figure 2.7 shows two examples of the intensity distribution of a propagated plane wave with wavelength λ for a grating where the depth and material of the bars are matched to shift the wave's phase by π and $\pi/2$, respectively. The gratings have a duty cycle of 0.5, which denotes the ratio between the grating spaces and its period.
It is found that the self-image, i.e. a box-shaped intensity distribution of the propagated wave, repeats itself at a certain distance, i.e. the full *Talbot distance*, and multiple integers m of it:

$$d_{\mathrm{T}} = \frac{2p_1^2}{\lambda}, \tag{2.25}$$

where p_1 denotes the periodicity of the grating. The distance $m\,d_{\mathrm{T}}$ is called the mth Talbot distance. It turns out that for certain phase shifts imposed on the plane and monochromatic wave, repetitions can be found at rational fractions of the Talbot distance. Weitkamp et al. (2006) summarize the rule for calculation of

the fractional Talbot distances for π and $\pi/2$ shifting gratings by

$$d_{\mathrm{T,f}} = \frac{n\, p_{1,\mathrm{eff}}^2}{2\lambda}, \tag{2.26}$$

with $n = 1, 2, ...$ being the fractional Talbot orders and $p_{1,\mathrm{eff}}$ being the effective period of the modulation inducing grating G1, i.e. the period of the intensity modulation. $p_{1,\mathrm{eff}}$ is defined depending of the respective wave-front modulation as follows:

$$p_{1,\mathrm{eff}} = \frac{p_1}{\eta} \quad \text{with} \begin{cases} \eta = 1 & \text{for absorbing or } \pi/2\text{-shifting grating.} \\ \eta = 2 & \text{for } \pi\text{-shifting grating.} \end{cases} \tag{2.27}$$

This formulation accounts for the fact that a π-shifting phase grating produces an interference pattern with half the period, while the pattern generated by a $\pi/2$-shifting grating has a period matching the grating pitch. Phase-shifting gratings produce self-images at odd Talbot orders ($n = 1, 3, 5...$), absorbing gratings at even Talbot orders ($n = 2, 4, 6...$).
Montgomery (1967) showed that also quasi-periodic structures create self-images, which means that the Talbot effect represents only a subset of self-imaging effects (Lohmann et al., 2005). In Figure 2.7, the fractional Talbot distances up to a full Talbot distance are given for the $\pi/2$-shifting (a) and the π-shifting (b) grating.

As grating-based interferometry relies on the interference pattern at a certain (fractional) Talbot distance as the spatial reference, the method is also called *Talbot interferometry*. In most cases, a phase-shifting grating is used to create the interference pattern, which is therefore called phase grating G1. To record the interference pattern, the detector is placed at a (fractional) Talbot distance. However, in practice the detector pixels are usually too large to resolve the minima and maxima of the pattern directly, because detectors with smaller pixels require too large flux or too long exposure times to obtain a reasonable signal-to-noise ratio, and usually do not provide a sufficiently large field of view. Therefore, another grating, called analyzer grating G2, is placed right in front of the detector to rasterize the pattern. Its period p_2 has to match the period of the sampled interference pattern. The measurement process of rasterizing the pattern and the extraction of the three signals are described in detail in Section 2.3.3.
Strictly speaking, the Talbot effect only denotes the case of illumination with a plane and coherent wave. The dependence of the Talbot distances on the wavelength tells us that, in case of longitudinally incoherent waves, i.e. a polychromatic x-ray beam, the interference pattern can be described as a superposition of laterally displaced individual interference patterns of the respective wavelengths that occur in the x-ray source spectrum. This leads to a washed out final interference

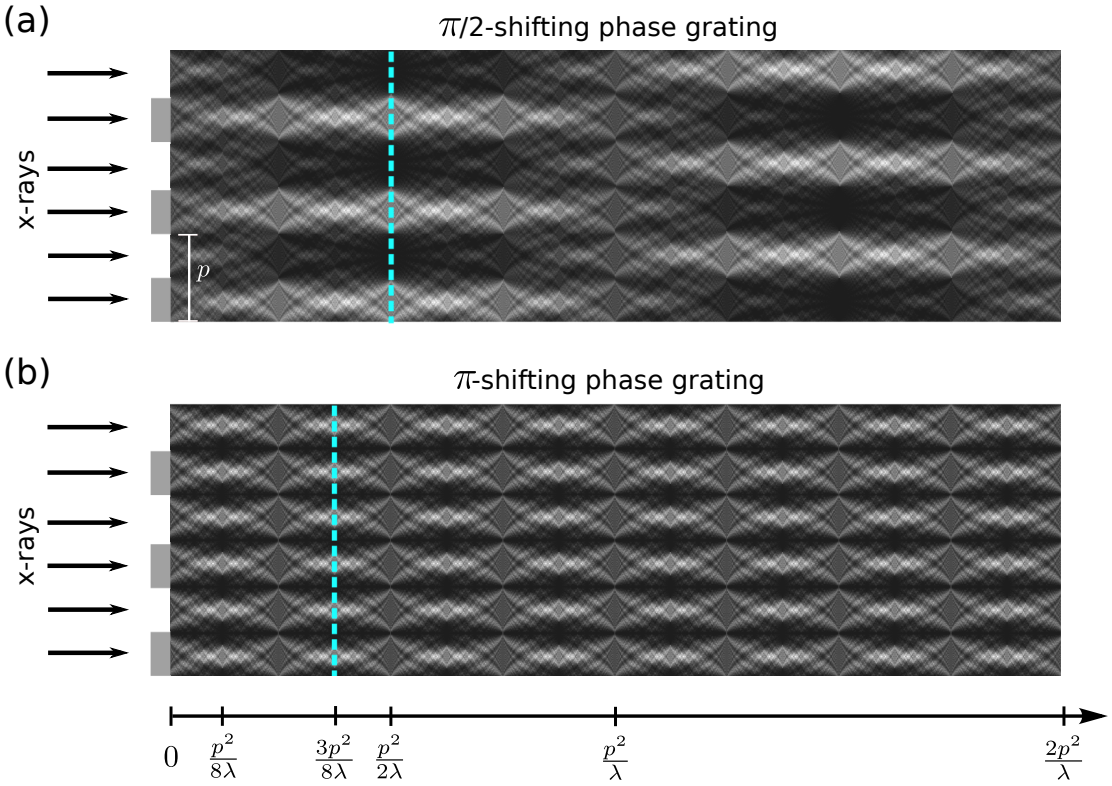

Figure 2.7: X-ray intensity patterns created by a plane x-ray wavefront that was propagated through a $\pi/2$-shifting (a) and a π-shifting (b) phase grating. For each intensity pattern two exemplary fractional Talbot distances are marked by a dashed line, at which the intensity pattern is box shaped. The propagation is plotted up to the first full Talbot distance. Figure adapted from Tapfer (2013).

pattern, i.e. the difference between minima and maxima of the pattern is reduced. Nonetheless, interferometric imaging is routinely used with polychromatic light sources. Engelhardt et al. (2008) and Chabior et al. (2011) provide an in-depth analysis about the effects of a polychromatic beam on Talbot interferometry.

2.3.2 The Lau effect

From Section 2.3.1, it is clear that grating-based imaging (GBI) relies on interference at a certain distance from the phase grating G1, which only occurs if the illumination radiation exhibits sufficient spatial coherence. In Section 2.1.2, it was shown that the spatial coherence directly depends on the source size and its distance. For grating interferometry, only spatial coherence in the direction perpendicular to the grating bars matters.
To describe the effect of an extended source onto the interference pattern, the

source can be understood as a sequence of individual point sources in a line perpendicular to the grating bars. Each of those point sources gives cause to a slightly shifted interference pattern behind the phase grating. The superposition of the many laterally displaced patterns causes the resulting pattern to be blurred. The extent of this effect is described by the projected source size, defined as

$$s' = \frac{d}{L}\, s, \tag{2.28}$$

where d denotes the distance between the phase grating and the detection plane, i.e. the position of the analyzer grating, and L the distance between the source and the phase grating (Figure 2.8a).

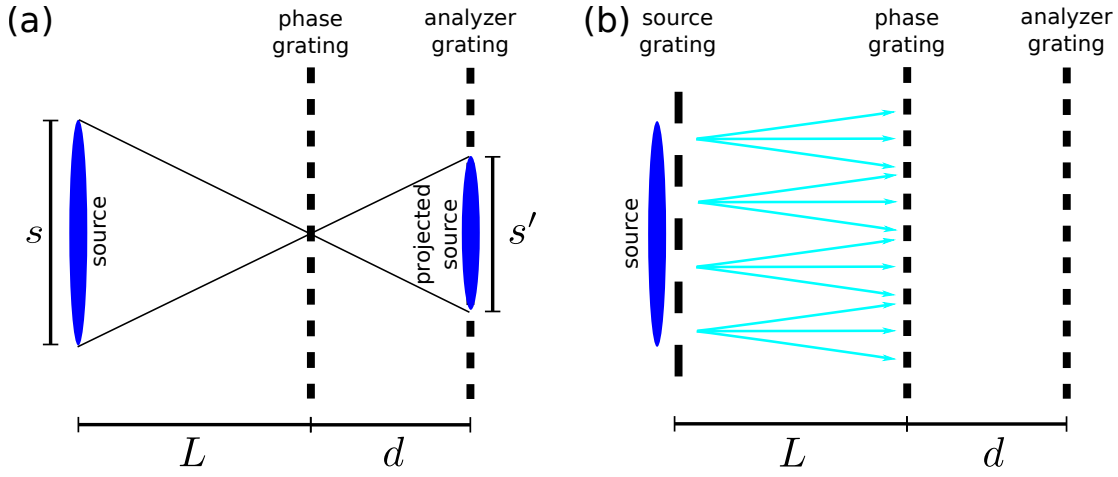

Figure 2.8: Spatial coherence with an extended source. (a) An extended source causes blurring of the interferometric pattern due to insufficient spatial coherence. This effect is quantified by the projected source size s' at the position of the analyzer grating. (b) A source grating divides the source into mutually incoherent line sources to regain spatial coherence. Figures adapted from Tapfer (2013).

In case the projected source size is too large to gain a satisfactory quality of the interference pattern, a third grating is introduced into the optical path, right behind the source. The so called source grating G0 has highly absorbing bars, usually made of gold, and thereby divides the extended source into mutually incoherent smaller line sources, as illustrated in Figure 2.8b. Each of the individual line sources gives rise to an interference pattern behind the phase grating. For these interference patterns to superimpose in an amplifying manner, the period of the source grating has to follow

$$p_0 = \frac{L}{d}\, p_2, \tag{2.29}$$

so that the displacement between the individual interference patterns is exactly one period of the patterns or an integer multiple thereof. This effect of increased transverse coherence by introduction of a third grating is called *Lau effect* (Lau, 1948). Grating interferometry carried out with a source grating is therefore also referred to as *Talbot-Lau interferometry*.
GBI without a source grating is possible at some setups with a synchrotron radiation source, which usually delivers highly coherent x-rays with a small source size and/or a large distance to the source. In a laboratory setup, sufficient coherence can be reached when using a micro-focus source, where the focal spot is extremely small. This comes at the cost of extremely limited flux and, thus, necessarily increased detector exposure times. The introduction of the source grating by Pfeiffer et al. (2006) and Weitkamp et al. (2006) rendered the method applicable with conventional x-ray sources with larger focal spots and reasonably high flux for imaging applications. The setup used for imaging in this thesis represents such a Talbot-Lau interferometer.
Note, that, nevertheless, the source grating does not improve the blurring effect that an extended source has on the spatial resolution of the imaging system, as it only enhances the coherence.

2.3.3 Scanning procedure and signal extraction

A sample placed into the beam path of the interferometer influences the interferometric pattern in three ways, which are illustrated individually in Figure 2.9. A purely absorbing object causes an overall intensity reduction behind the sample, so that the offset of the interferometric fringes is lowered (Figure 2.9a). A sample that only shifts the x-ray's phase, such as the wedge in Figure 2.9b, changes the propagation direction. This causes the interference pattern to be laterally shifted relative to the pattern in absence of a sample. If the x-rays are scattered at microstructures in an object, the minute direction changes of the x-rays lead to a smearing of the interference pattern, i.e. the difference between minima and maxima decreases (Figure 2.9c). In fact, the scattering is mainly composed of refraction at the interfaces within the microstructures that cannot be resolved on the length scale of the interferometric pattern as separate phase shifts anymore.

These three components of the interferometric pattern, i.e. offset, lateral shift, and oscillation amplitude, can be measured using the analyzer grating G2, which was briefly introduced in Section 2.3.1. The grating bars of G2 are usually made of a highly absorbing material such as gold, so that behind the bars ideally the transmission is zero and in between the bars the full intensity is recorded. To understand the scanning procedure, first, the formation of the original interference

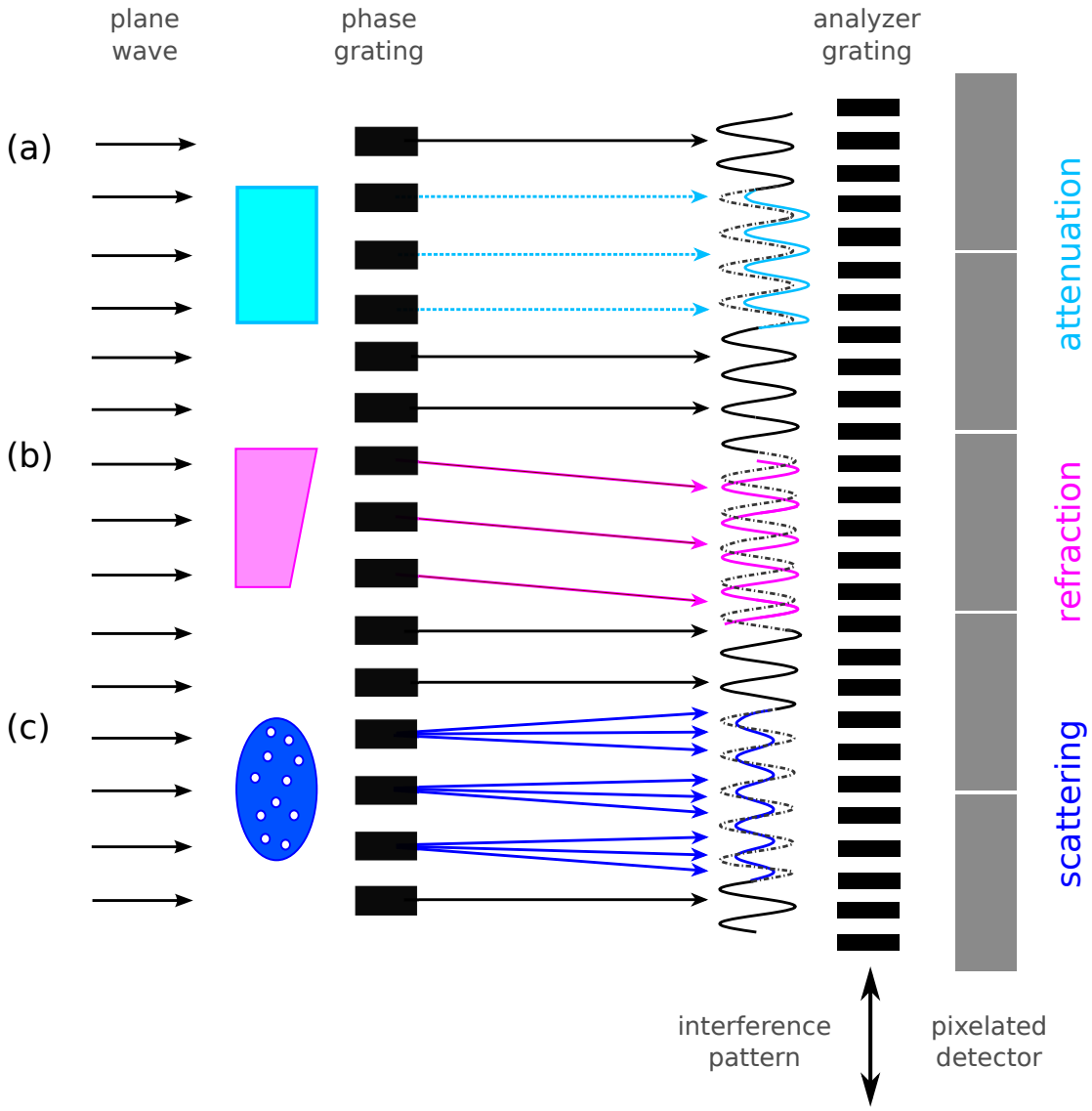

Figure 2.9: Working principle of a Talbot(-Lau) interferometer. A plane x-ray wavefront encounters objects that exhibit differing influences on the wave and thus alter the original interference pattern depicted in black. (a) A purely attenuating object reduces the average intensity (cyan). (b) A solely phase-shifting, i.e. refracting, object shifts the interference pattern laterally (magenta). (c) An object containing scattering microstructures diminishes the amplitude of the pattern (dark blue). The direction of lateral displacement of the analyzer grating to perform a phase-stepping scan is indicated by the vertical arrow. Figures adapted from Tapfer (2013).

pattern with no sample in the beam is considered. As discussed previously, in an ideal case, a coherent plane wave illuminates the phase grating, which creates a box-shaped interference pattern at a certain distance d. The pattern is sam-

pled by shifting the absorbing analyzer grating lateral to the beam path and by recording images at several positions of the grating along one fringe period of the interference pattern. This procedure is referred to as *phase stepping* (Weitkamp et al., 2005). One detector pixel is usually of such a size that the average intensity of many G2 grating slits is registered.
The signal that is thereby recorded in each pixel is mathematically described by a convolution of the box-shaped interference pattern with the box-shaped function representing the absorbing bars of the analyzer grating, resulting in a triangular intensity variation over one stepping period. In reality, the signal has to be convoluted with a third function representing the shape of the source, which is another box-shaped term, if a source grating is used. The resulting intensity $I(x_n)$ that is measured in each detector pixel during a phase-stepping scan can be described by a Fourier expansion series of the form

$$I(x_n) = \sum_{m=0}^{\infty} a_m \cos\left(m \frac{2\pi}{p_2} x_n + \phi_m\right). \tag{2.30}$$

The x_n denote the grating positions, a_m the amplitude coefficients and ϕ_m the interferometer phase coefficients. It was shown by Bech (2009) that, in a setup with moderate coherence due to a polychromatic beam, the curve can be readily described by a cosine curve, and higher-order harmonics can be neglected:

$$I(x_n) = a_0 + a_1 \cos\left(\frac{2\pi}{p_2} x_n - \phi_1\right). \tag{2.31}$$

The stepping curve is then sufficiently defined by the offset a_0 (average value), the amplitude a_1, and the relative phase ϕ_1. By introducing a sample into the beam, the parameters are affected as follows: The offset is lowered by attenuation, the phase is shifted by refraction, and the amplitude is reduced by scattering. The three effects are illustrated in Figure 2.10.

As discussed before, the interference pattern acts as a spatial reference, therefore the phase stepping curve has to be measured twice: once without a sample in the beam, which is called flatfield or reference measurement and subsequently denoted by the superscript 'r', and once with the sample in the beam, which is denoted by the superscript 's'.
The offset and amplitude parameters of the flatfield phase-stepping curve give a direct measure of the degree of interference in the given setup. This performance parameter is called *visibility* and is defined as

$$V_r := \frac{a_1^{\mathrm{r}}}{a_0^{\mathrm{r}}} = \frac{I_{\max} - I_{\min}}{I_{\max} + I_{\min}}, \tag{2.32}$$

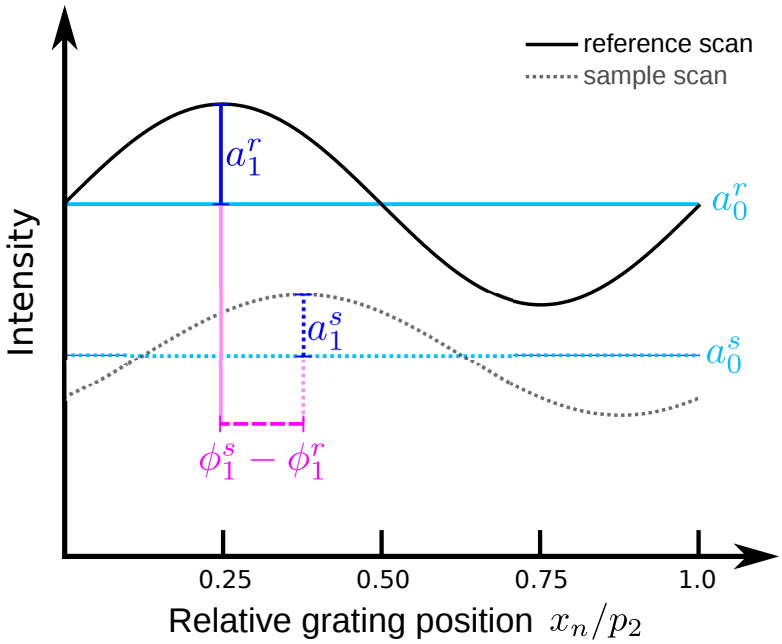

Figure 2.10: Phase-stepping curves of sample (solid line, superscript s) and reference (dotted line, superscript r) measurement to illustrate the change in intensity in one detector pixel during a phase-stepping scan. The effects of attenuation (cyan), refraction (magenta) and scattering (dark blue) introduced by the sample onto the parameters a_0, ϕ_1 and a_1, which describe the stepping curve, are color-coded according to Figure 2.9.

where $I_{\max}$ and $I_{\max}$ are maximum and minimum value of the measured intensity curve, respectively.

The ratio between the offsets of the two phase-stepping curves conveys the transmission T, which is also measured in any conventional x-ray imaging setup:

$$T := \frac{a_0^{\mathrm{s}}}{a_0^{\mathrm{r}}}. \tag{2.33}$$

Analogous to this, the ratio between the sample-curve visibility and the flatfield-curve visibility, provides us with the visibility change due to scattering:

$$V := \frac{V^{\mathrm{s}}}{V^{\mathrm{r}}} = \frac{a_1^{\mathrm{s}}/a_0^{\mathrm{s}}}{a_1^{\mathrm{r}}/a_0^{\mathrm{r}}}. \tag{2.34}$$

The lateral shift of the interference pattern due to refraction is proportional to the phase difference of the two curves:

$$\phi := \phi_1^{\mathrm{s}} - \phi_1^{\mathrm{r}}. \tag{2.35}$$

Note that, due to the periodicity of the cosine curve and the interference pattern, a lateral shift of more than one period of the pattern is not considered by the

measurement method and consequently cut off to only the relative difference. This phenomenon is called *phase wrapping*.

As those measures are recorded in each detector pixel with indices (x, y), the trimodal contrast images can be deduced. The *attenuation (A) image* is simply defined as $1 - T(x, y)$. The *dark-field (DF) image* is given by the visibility ratio $V(x, y)$ between sample and reference image. The term 'dark-field' originates from visible-light microscopy, where purely scatter-based images are denoted as 'dark-field microscopy images', because scattering structures appear bright on a dark background. The actual physical displacement of the interference pattern can be calculated as

$$S(x, y) = \frac{p_2}{2\pi}\,\phi(x, y). \tag{2.36}$$

This corresponds to a refraction angle of

$$\alpha(x, y) = \frac{p_2}{2\pi d}\,\phi(x, y). \tag{2.37}$$

Finally, the phase shift of the wave front Φ behind the object can be written as

$$\frac{\partial\Phi(x, y)}{\partial x} = \frac{2\pi}{\lambda}\,\alpha(x, y) = \frac{p_2}{\lambda d}\,\phi(x, y). \tag{2.38}$$

Here, Equation 2.8 was used. Note that the measurement of the two phase-stepping curves only gives access to the first derivative of the phase shift induced by the sample. Therefore, the image resulting from $\frac{\partial\Phi(x,y)}{\partial x}$ is called *differential phase-contrast (DPC) image*.

The standard process to extract the parameters from the phase-stepping curves is a pixel-wise Fourier analysis of the measured data. Due to efficient fast-fourier-transform (FFT) implementations in many programming languages, this provides a quick way for signal extraction. Also, higher harmonic fourier components can in principle be retrieved, if the degree of coherence at the setup requires their inclusion into the analysis. An alternative approach is the application of a sinusoidal fit to extract the parameters. In Section 3.3.3, two processing methods based on sinusoidal fitting are presented that provide additional information or can handle unstable phase-stepping positions, respectively.
In the case that the curve is sufficiently described by a cosine function, a sampling of the curve by three stepping positions is theoretically acceptable. However, adding more phase steps improves the signal-to-noise ratio and is therefore common practice.
In the course of this description of the scanning process, the analyzer grating was assumed to be laterally shifted during the stepping procedure, as it is the most

intuitive way to understand the rasterization of the interference fringes. Note, however, that in principle each of the three gratings that comprise the interferometer can be stepped, as long as in projection the pattern period p_2 or an integer multitude of it is covered. More details on the signal-extraction chain can be found in Bech (2009).

When designing a Talbot-Lau interferometer, the parameters such as grating material, periods, bar heights, and distances have to be chosen carefully to match the wavelength of the effective energy, at which the x-ray source of the setup is then ideally operated. If the weighted average energy of the spectrum deviates from the intended design energy, a reduced visibility will be the result. Furthermore, the design parameters need to be balanced in many ways. For example, a longer setup that is operated at higher Talbot orders may deliver an increased sensitivity, i.e. the ability to resolve refraction angles of a certain size. However, a longer distance between source and detector comes at the cost of decreased photon flux. Variances of the interferometer design are discussed in detail by Chabior (2011).

2.3.4 Interferometer with divergent beam

A truly parallel beam, i.e. a plane wave that propagates through the interferometer, represents an ideal case. Usually, beam divergence has to be considered in the interferometer design. The divergence in the plane perpendicular to the grating bar direction (i.e. the 'fan' direction) is quantified by the magnification M

$$M = \frac{L + d}{d}, \tag{2.39}$$

where L is the distance from source to phase grating and d the distance from phase to analyzer grating. As the wave front carrying the interferometric pattern also propagates in a divergent manner, the Talbot distance has to be scaled accordingly to

$$d'_{\mathrm{T}} = M\, d_{\mathrm{T}}, \tag{2.40}$$

and the period of the analyzer grating has to be adapted to the magnified period of the interference pattern by

$$p'_2 = M\, p_2. \tag{2.41}$$

Consequently, the period of the source grating is then $p_0 = \frac{L}{d}\, p'_2$.
This approach only considers the global magnification of the wave. To account for the local curvature of the wavefront, the gratings need to be bent accordingly. The usage of a curved phase and analyzer grating at a compact setup was

demonstrated by Thüring et al. (2011a). However, their production and handling is still rather demanding, as the bending process introduces local deformations that can cause artifacts in the images. Especially the extremely small bending radius, which would be necessary for the source grating, poses a challenge. Using non-bent gratings with a fan-angle geometry has two drawbacks: As the direction of incidence of an x-ray is more and more inclined relative to the grating bars towards the horizontal margins of the grating, more of the radiation is absorbed in the grating bars. This geometrical shadowing leads to a lower transmission and increased noise and decreased visibility in this region. It is of practical relevance as it limits the usable field of view (FOV) or the grating-bar aspect-ratio in compact setups. The second effect is a mismatching phase shift imposed onto the wave front passing through the outer regions of the phase grating, which also gives rise to a lowered visibility.
Regarding the divergence of the beam along the grating-bar direction, shadowing is not an issue. The variation in phase modulation also occurs along this direction. However, in the setup used in this thesis, the angular opening in the vertical direction is considerably smaller, so that the effect is of less relevance.

At a Talbot interferometer setup with a fan beam, the divergence has to be accounted for when the refraction angle α induced by the sample (or equivalently the refractive index decrement δ of the sample) is retrieved. For truly quantitative values, the measured values of the refraction angle α have to be rescaled according to Engelhardt et al. (2007) by

$$\alpha' = \frac{L}{r_\mathrm{L}}\,\alpha, \tag{2.42}$$

where r_L is the distance between source and object.

2.4 Principles of tomographic reconstruction

In this section, the procedure of tomographic reconstruction is introduced, which constitutes the computational part of computed tomography (CT). Tomographic reconstruction serves to compute a three-dimensional representation of an object, from which numerous projection images were measured at different angular views. In conventional attenuation-based CT, the distribution of the linear attenuation coefficient μ is retrieved from the measured transmitted intensities. The most commonly applied algorithm for this is filtered backprojection (FBP). In Section 2.4.1, first the Fourier slice theorem is introduced, as it represents the foundation of the FBP. Then the filtered backprojection itself is derived for the

case of parallel beam (Section 2.4.2). As the setup used in this thesis has a moderate divergent beam geometry, the modifications to the algorithm that are necessary to account for a cone-shaped beam are given in Section 2.4.4. Finally, a short overview over different iterative reconstruction techniques is provided in Section 2.4.5.

2.4.1 Fourier slice theorem

Following the description in the textbook by Kak and Slaney (2001), first, line integrals and projections are introduced for a basic understanding of the Fourier slice theorem. For the sake of simplicity, an object is considered that is described by a two-dimensional function $f(x, y)$. A projection along a line defined by the coordinates θ and t (Figure 2.11) can be written as the line integral

$$\mathcal{P}_\theta(t) = \int\limits_{(\theta,t)\text{line}} f(t, s)\,\mathrm{d}s. \tag{2.43}$$

Here, the coordinate system (t, s) tilted by θ and the original coordinate system (x, y) are linked via

$$\begin{bmatrix} t \\ s \end{bmatrix} = \begin{bmatrix} \cos\theta & \sin\theta \\ -\sin\theta & \cos\theta \end{bmatrix} \begin{bmatrix} x \\ y \end{bmatrix}. \tag{2.44}$$

Thus, Equation 2.43 can be rewritten as

$$\mathcal{P}_\theta(t) = \int\limits_{-\infty}^{\infty}\int\limits_{-\infty}^{\infty} f(x, y)\,\delta_\mathrm{D}(x\cos\theta + y\sin\theta - t)\,\mathrm{d}x\mathrm{d}y, \tag{2.45}$$

with δ_D representing the Dirac delta function. $\mathcal{P}_\theta(t)$ is called the Radon transform of $f(x, y)$ (Radon, 1917). A projection that is constituted of a set of such line integrals where the lines for different t are assumed to be parallel is called a parallel projection. The projections for all sampled angles θ stacked together are called a *sinogram* $\mathcal{P}(\theta, t)$, because a point in the object will follow a sine curve in this representation.
The Fourier slice theorem states that the one-dimensional Fourier transform of a parallel projection of an object $f(x, y)$ taken at an angle θ is equal to a slice of the two-dimensional Fourier transform of the object itself, inclined by the angle θ in the frequency domain. This is illustrated in Figure 2.11.

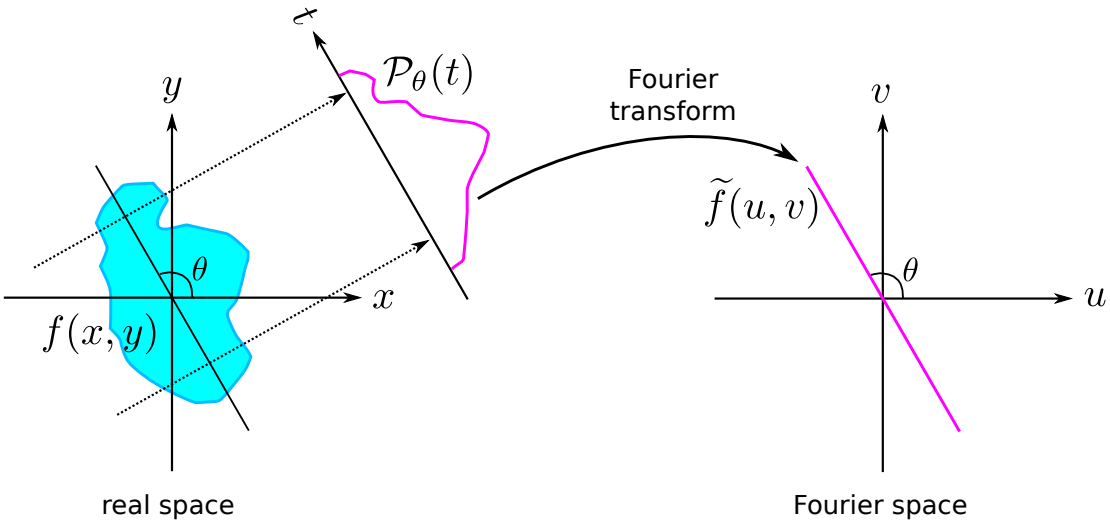

Figure 2.11: Sketch of the principle of the Fourier slice theorem. The one-dimensional Fourier transform of the projection $\mathcal{P}_\theta(t)$ of the object $f(x,y)$ at angle θ is equal to a slice inclined by θ of the two-dimensional Fourier transform $\widetilde{f}(u,v)$ of the object itself. Figure adapted from Kak and Slaney (2001).

It can be derived as follows: The one-dimensional Fourier transform of the projection is described by

$$\widetilde{\mathcal{P}}_\theta(\omega) = \int_{-\infty}^{\infty} \mathcal{P}_\theta(t)\, e^{-i2\pi\omega t}\, \mathrm{d}t. \tag{2.46}$$

Combining Equation 2.43 and 2.46 and transforming it to the non-tilted coordinate system leads to

$$\widetilde{\mathcal{P}}_\theta(\omega) = \int_{-\infty}^{\infty}\int_{-\infty}^{\infty} f(x,y)\, e^{-i2\pi\omega(x\cos\theta + y\sin\theta)}\, \mathrm{d}x\mathrm{d}y. \tag{2.47}$$

On the other hand, the two-dimensional Fourier transform of the object function $f(x,y)$ is given by

$$\widetilde{f}(u,v) = \int_{-\infty}^{\infty}\int_{-\infty}^{\infty} f(x,y)\, e^{-i2\pi(ux+vy)}\, \mathrm{d}x\mathrm{d}y. \tag{2.48}$$

By comparing Equation 2.47 with 2.48, the essence of the Fourier slice theorem becomes obvious: $\widetilde{f}(u,v) = \widetilde{\mathcal{P}}_\theta(\omega)$ with the transformation to polar coordinates (θ,ω) as $(u,v) = (\omega\cos\theta, \omega\sin\theta)$.

The direct consequence of the Fourier slice theorem is that, if the frequency space (u, v) is infinitely sampled, which means an infinite number of projections is at hand, the original object function can be reconstructed by using the inverse Fourier transform:

$$f(x,y) = \int_{-\infty}^{\infty}\int_{-\infty}^{\infty} \widetilde{f}(u,v)\, e^{i2\pi\omega(ux+vy)}\, \mathrm{d}u\mathrm{d}v. \tag{2.49}$$

This way of deriving an image $f(x, y)$ from its projections is called the inverse Radon transform.

2.4.2 Filtered backprojection

Filtered backprojection (FBP) is currently the most commonly used algorithm for tomographic reconstruction due to its simplicity and easy implementation. It makes direct use of the Fourier slice theorem, which states that an object can be recovered from projection measurements of the object.
When Equation 2.49 is transformed from the rectangular grid to polar coordinates using $u = \omega\cos\theta$ and $v = \omega\sin\theta$ and changing the differentials by $\mathrm{d}u\mathrm{d}v = \omega\,\mathrm{d}\omega\mathrm{d}\theta$, the following expression is obtained:

$$f(x,y) = \int_{0}^{\pi}\int_{-\infty}^{\infty} \widetilde{f}(\omega,\theta)\,|\omega|\, e^{i2\pi\omega(x\cos\theta+y\sin\theta)}\, \mathrm{d}\omega\mathrm{d}\theta, \tag{2.50}$$

For details on the conversion, the reader is referred to Kak and Slaney (2001). According to the Fourier slice theorem, the two-dimensional Fourier transform $\widetilde{f}(\omega, \theta)$ can be substituted by the Fourier transform of the projection at angle θ, $\widetilde{\mathcal{P}}_\theta(\omega)$, and the integral can be split into the integrations over ω and over θ:

$$f(x,y) = \int_{0}^{\pi}\left[\int_{-\infty}^{\infty} \widetilde{\mathcal{P}}_\theta(\omega)\,|\omega|\, e^{i2\pi\omega(x\cos\theta+y\sin\theta)}\, \mathrm{d}\omega\right]\mathrm{d}\theta, \tag{2.51}$$

The inner integral

$$\mathcal{Q}_\theta(x\cos\theta + y\sin\theta) = \int_{-\infty}^{\infty} \widetilde{\mathcal{P}}_\theta(\omega)\,|\omega|\, e^{i2\pi\omega(x\cos\theta+y\sin\theta)}\, \mathrm{d}\omega, \tag{2.52}$$

represents a filtering operation in Fourier space on the measured projections. The factor $|\omega|$ accounts for the denser sampling towards the origin in Fourier space

(Figure 2.12) by weighting the high-frequency components stronger than the low-frequency components. Generally speaking, this so-called *ramp filter* or *Ram-Lak filter* constitutes the filter part in the filtered backprojection.
The outer integral

$$f(x,y) = \int_0^{\pi} \mathcal{Q}_\theta(x\cos\theta + y\sin\theta)\,\mathrm{d}\theta, \tag{2.53}$$

merely represents the summation of the filtered projections over all angles θ. This represents the *backprojection* of the FBP and can be understood as smearing the measured projections back over the reconstruction plane under their corresponding angle.
In reality, projections can only be taken at a finite number of angular views. In that case, $\widetilde{f}(u,v)$ is only known on a finite number of radial lines in the frequency space, as depicted in Figure 2.12. Also, measured projections have a discretized representation due to the pixelated detector array, which means that, in an algorithmic implementation, a change to the discrete Fourier transform is necessary. As the reconstructed object is usually defined on a Cartesian grid, but the sampling in Fourier space is done in a polar coordinate system, interpolation between the grids is necessary.

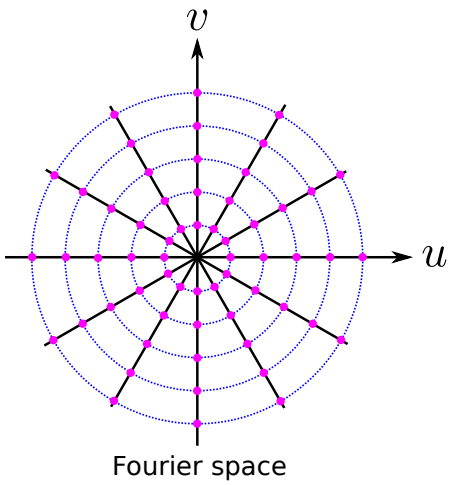

Figure 2.12: Sampling in Fourier space: Collecting projections at certain angles in real space corresponds to sampling at radial lines in Fourier space. If a discrete Fourier transform algorithm is used, the magenta-colored discrete dots represent the actual sampling locations of the Fourier transform. Figure adapted from Kak and Slaney (2001).

For a correct representation of the reconstructed object using FBP, the sampling of the Fourier space has to be sufficiently dense also in the outer regions. The

sampling limit is determined via the Nyquist sampling theorem, which states that a signal must be sampled at least twice during each cycle of the highest frequency of the signal. Translating this to the $\mathcal{N}_\theta$ angular samples taken during the projection acquisition in CT, and assuming that the $\mathcal{N}_{\text{pix}}$ detector pixels in horizontal direction are the finest sampling available, the minimum necessary number of projections is

$$\mathcal{N}_\theta = \frac{\pi}{2}\mathcal{N}_{\text{pix}}, \tag{2.54}$$

according to Müller (1998).

2.4.3 Line integrals for trimodal tomographic reconstruction

The three imaging signals transmission, differential phase, and dark field that are accessed by grating-based interferometry in projection (Section 2.3) originate from three different physical quantities that can be recovered using FBP for tomographic reconstruction.

The **transmission** $T = a_{\text{s}}^0/a_{\text{r}}^0$, as introduced in Section 2.3.3, recorded at angle θ is connected to the linear attenuation coefficient μ according to the Lambert-Beer law (see Equation 2.16)

$$T_\theta(t) = \exp\left(-\int_0^D \mu(t,s)\,\mathrm{d}s\right), \tag{2.55}$$

where the integration is performed along the direction s in the tilted coordinate system (Equation 2.44 and Figure 2.11) between x-ray source and detector, so practically from 0 to the thickness D of the sample. Equation 2.43 can then be rewritten with the object function represented by $\mu(x,y)$ and the projections denoted by the negative natural logarithm of the transmission measured at angle θ:

$$\mathcal{P}_\theta(t) = -\ln\left(T_\theta(t)\right) = \int_0^D \mu(t,s)\,\mathrm{d}s. \tag{2.56}$$

Applying FBP according to Equations 2.52 and 2.53, the distribution of $\mu(x,y)$ in the sample space can be recovered by using the one-dimensional Fourier transform

$\widetilde{\tau}_\theta(\omega) = \mathcal{FT}\{-\ln T_\theta(t)\}$ of the negative natural logarithm of the transmission and by changing to polar coordinates. The filtering is performed according to

$$\mathcal{Q}_\theta(x\cos\theta + y\sin\theta) = \int_{-\infty}^{\infty} \widetilde{\tau}_\theta(\omega)\, F(\omega)\, e^{i2\pi\omega(x\cos\theta + y\sin\theta)}\, \mathrm{d}\omega, \tag{2.57}$$

with the ramp-shaped filter function $F(\omega) = |\omega|$. The filtered projections are backprojected via

$$\mu(x,y) = \int_0^{\pi} \mathcal{Q}_\theta(x\cos\theta + y\sin\theta)\, \mathrm{d}\theta. \tag{2.58}$$

In daily practice of using FBP on conventional attenuation data, the filter function can vary from the strict ramp-shaped filter, if high frequencies ought to be suppressed further, for example by using a *Hamming window* (Andersen and Kak, 1984).

Using tomographic reconstruction, it is also possible to retrieve the refractive index decrement $\delta(x,y)$ from the **differential phase** data measured in projection by a grating interferometer. With Equation 2.38 linking the measured refraction angle α to the differential phase of the wavefront $\frac{\partial\Phi}{\partial t}$ and to the phase parameter of the stepping curve ϕ, and by using Equations 2.20 the expression

$$\alpha_\theta(t) = \frac{\lambda}{2\pi}\frac{\partial\Phi_\theta}{\partial t} = \frac{p_2}{2\pi d}\,\phi_\theta(t) = \int_0^{D} \frac{\partial\delta(s,t)}{\partial t}\,\mathrm{d}s \tag{2.59}$$

is obtained, when introducing the (t,s) grid rotated by angle θ. Thus, the projections are defined as follows:

$$\mathcal{P}_\theta(t) = \frac{p_2}{2\pi d}\,\phi_\theta(t) = \frac{\partial}{\partial t}\int_0^{D} \delta(s,t)\,\mathrm{d}s. \tag{2.60}$$

Because of the partial derivative $\frac{\partial}{\partial t}$, the FBP cannot be applied in the same manner as for the transmission projections. However, it is possible to compensate for the differential projections by considering how the Fourier transform acts upon the derivative of a function $f(x)$:

$$\mathcal{FT}\{\frac{\partial}{\partial x} f(x)\} = 2\pi i\omega\, \widetilde{f}(\omega). \tag{2.61}$$

Thereby, the filter function described in Equation 2.52 can be adapted for differential data to

$$\mathcal{H}_\theta(x\cos\theta + y\sin\theta) = \int_{-\infty}^{\infty} 2\pi i\omega\, \widetilde{\delta}_\theta(\omega)\, \frac{|\omega|}{2\pi i\omega}\, e^{i2\pi\omega(x\cos\theta + y\sin\theta)}\, \mathrm{d}\omega. \tag{2.62}$$

In conlusion, an FBP reconstruction from differential data only requires replacing the Ram-Lak filter by the imaginary filter function

$$H(\omega) = \frac{|\omega|}{2\pi i\omega} = 2\pi i\, \mathrm{sgn}(\omega), \tag{2.63}$$

called *Hilbert filter* (Pfeiffer et al., 2007b). The backprojection can be applied without further modification:

$$\delta(x,y) = \int_0^{\pi} \mathcal{H}_\theta(x\cos\theta + y\sin\theta)\, \mathrm{d}\theta. \tag{2.64}$$

From **dark-field** projection data as extracted by a Talbot interferometer, a physical quantity referred to as the *linear diffusion coefficient* ε can be deduced by means of tomographic reconstruction. The diffusion coefficient describes the local scattering power that the sample exhibits to x-rays. Bech (2009) showed that the measured visibility $V = V^{\mathrm{s}}/V^{\mathrm{r}}$ at the angle θ is connected to the linear diffusion coefficient via

$$V_\theta(t) = \exp\left(\frac{-2\pi^2 d^2}{p_2^2} \int_0^D \varepsilon(t,s)\, \mathrm{d}s\right), \tag{2.65}$$

in analogy to the relation of linear attenuation coefficient and x-ray attenuation. It is assumed that the scattering in each segment along the integration direction causes a Gaussian angular broadening.
The projection data used as input for the FBP can then be written for dark-field scans as the natural logarithm of the visibility

$$\mathcal{P}_\theta(t) = -\frac{p_2^2}{2\pi^2 d^2}\, \ln\left(V_\theta(t)\right) = \int_0^D \varepsilon(t,s)\, \mathrm{d}s. \tag{2.66}$$

Then the FBP can be performed with the standard filter function and backpro-

jection procedure:

$$\mathcal{Q}_\theta(x\cos\theta + y\sin\theta) = \int_{-\infty}^{\infty} \widetilde{\epsilon}_\theta(\omega)\, F(\omega)\, e^{i2\pi\omega(x\cos\theta + y\sin\theta)}\, \mathrm{d}\omega, \tag{2.67}$$

$$\varepsilon(x,y) = \int_{0}^{\pi} \mathcal{Q}_\theta(x\cos\theta + y\sin\theta)\, \mathrm{d}\theta. \tag{2.68}$$

2.4.4 Geometry with divergent beam

The description of the filtered backprojection in Section 2.4.2 portrays the ideal case of parallel rays that traverse the object and that are then recorded by a horizontal row of detector pixels. However, this case often does not hold true in reality. Only imaging setups with a very long distance between source and sample stage can apply algorithms that use the parallel beam approximation. In clinical practice and in small-animal imaging, however, the distances between x-ray source, sample and detector are short, which requires a description of the beam geometry as divergent in the plane defined by source and detector pixel row. The divergence causes the rays to form a *fan-shaped beam* in the (x, y) plane (Figure 2.13). If, in addition, more than a small slice in the longitudinal direction of the object is illuminated and accordingly covered by an area detector extended in the z direction, the divergence is described by a *cone-beam geometry* (Figure 2.14). Both divergence directions have to be considered in the reconstruction algorithm, so that a geometrically correct three-dimensional image representation of the measured object is recovered. As the scanner used in this work is compact and, thus, exhibits a moderate cone-beam geometry, the basic formulas to extend the FBP reconstruction algorithm to divergent beam geometries are presented here.

Fan beam. For a fan-shaped beam, algorithmically, the cases of equidistant sampling of the rays by a flat detector and equiangular sampling of the rays by a cylindrical detector have to be distinguished. Here, only the formulas for a flat detector shall be presented, as this is the geometry found in the setup used in this thesis. The complete derivation of the formulas for both cases can be found in the textbook by Kak and Slaney (2001).
An equidistant fan-beam geometry requires that the projection data is preweighted in addition to the (ramp-)filtering prior to backprojection. Each ray in the fan-shaped beam that is recorded by a detector pixel can be identified by its angle γ relative to the central ray in the fan, i.e. the one that is perpendicular

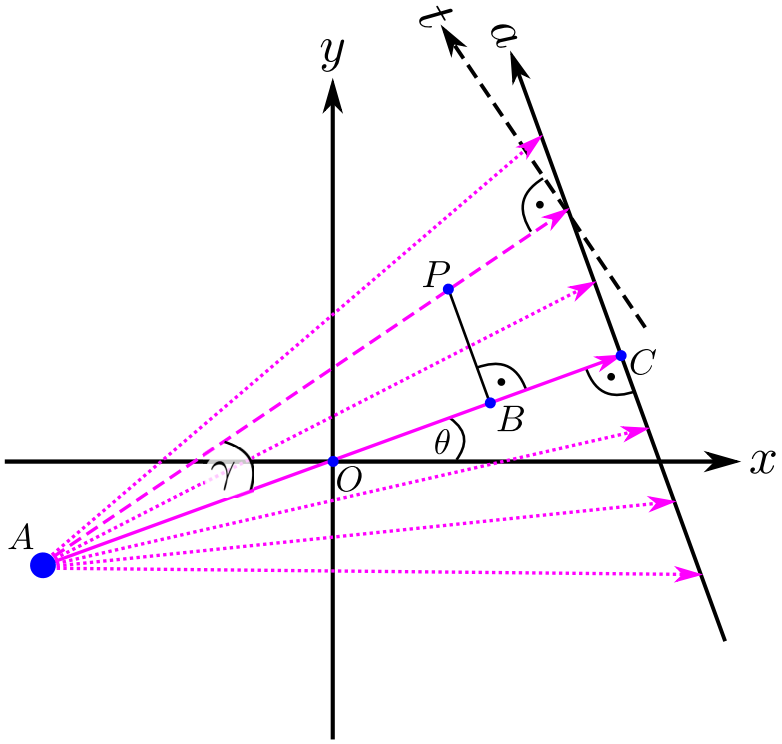

Figure 2.13: Sketch of fan-beam geometry and corresponding coordinate systems. The x-rays constituting the fan are depicted in magenta. The grid defined by the x- and y-axis is stationary. The a-axis and the central ray (solid line) from point A to C define the coordinate system that is rotated by θ relative to the stationary system around the origin O. A ray in the fan passing through point $P(x, y)$ (dashed line) is defined via its inclination γ relative to the central ray. The distance $\overline{AO}$ defines D_{SI} in the text. $\overline{AC}$ is the source-to-detector distance S and $\overline{AB}$ represents distance U.

to the detector surface (Figure 2.13). The weighting factor is represented by the cosine of this angle. It can be expressed by the source-to-detector distance S and the distance a of the corresponding detector pixel to the center of the corresponding pixel line on the detector. The pre-weighted projection at angular view θ is then

$$\mathcal{P}_\theta^{\mathrm{fan}}(a) = \cos\gamma \cdot \mathcal{P}_\theta(a) = \frac{S}{\sqrt{S^2 + a^2}}\,\mathcal{P}_\theta(a). \tag{2.69}$$

Following the notation by Turbell (2001), the transformation between the fixed (sample) coordinate system (x, y) and the detector coordinate a at projection with angular view θ is given by:

$$a(x, y, \theta) = S \cdot \frac{-x\sin\theta + y\cos\theta}{D_{\mathrm{SI}} + x\cos\theta + y\sin\theta}, \tag{2.70}$$

with D_{SI} being the distance between source and rotation center in the origin, usually referred to as isocenter. The filtering operation on the pre-weighted pro-

jections is according to Equation 2.52

$$\mathcal{Q}_\theta^{\text{fan}}(a) = \int_{-\infty}^{\infty} \widetilde{\mathcal{P}}_\theta^{\text{fan}}(\omega_a)\, |\omega_a|\, e^{i2\pi\omega_a a}\, \mathrm{d}\omega_a. \tag{2.71}$$

The filtered projections have to be backprojected along the direction of the original ray, which is accounted for by another weighting function:

$$f^{\text{fan}}(x,y) = \frac{1}{2}\int_0^{2\pi} \frac{S^2}{U(x,y,\theta)^2}\, \mathcal{Q}_\theta^{\text{fan}}(a(x,y,\theta))\, \mathrm{d}\theta, \tag{2.72}$$

with

$$U(x,y,\theta) = D_{\text{SI}} + x\cos\theta + y\sin\theta \tag{2.73}$$

being the distance between the source and the line parallel to the detector that intersects the point (x,y) in the reconstructed image (Figure 2.13). The fan-beam geometry and the relation between the coordinate systems is illustrated in Figure 2.13. Note that the integral for the backprojection in Equation 2.72 is taken over the complete angular range of 360° for θ, but is compensated by the factor $\frac{1}{2}$. In the parallel beam case, opposing angular views, i.e. projections at θ and $\theta + \pi$, contain just mirrored information, hence one half of the rotation is redundant. This is not the case in fan-beam geometry, as opposing views still sample the object differently at rays with $\gamma \neq 0$. However, the mathematically minimally required sampling range in case of a beam with fan-angle opening $\gamma_{\max}$ is $180° + 2\gamma_{\max}$ (Kak and Slaney, 2001).

Cone beam. The most popular three-dimensional filtered backprojection algorithm for the reconstruction of cone-beam CT data from a flat detector is the Feldkamp-Davis-Kress (FDK) algorithm (Feldkamp et al., 1984). It features strong analogy to the fan-beam FBP formulas. A detailed derivation is given in Kak and Slaney (2001). In the doctoral dissertation by Turbell (2001), a comprehensive overview is given and several implementation variations of the FDK algorithm are discussed. Here, the most important formulas shall be summarized.

Similar to the fan-beam case, projections acquired with a cone beam have to be pre-weighted. The *Feldkamp weights* are a combination of the cosine functions of both the angles in horizontal (fan, γ) and vertical (cone, κ) direction. The angles are measured between the ray that intersects the detector at position $Q(a,b)$ and the central ray of the projection, i.e. the line $\overline{\text{AO}}$ in Figure 2.14:

$$\mathcal{P}_\theta^{\text{cone}}(a,b) = \cos\gamma\, \cos\kappa \cdot \mathcal{P}_\theta(a,b) = \frac{S}{\sqrt{S^2 + a^2 + b^2}}\, \mathcal{P}_\theta(a,b). \tag{2.74}$$

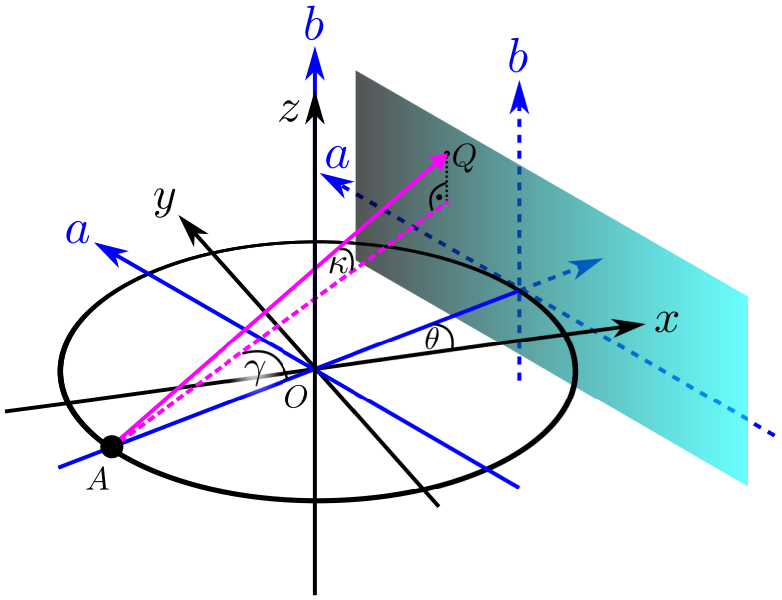

Figure 2.14: Sketch of cone-beam geometry and corresponding coordinate systems. An x-ray (solid magenta line) hits the detector at point $Q(a, b)$. Its direction is described by the fan angle γ and the cone angle κ relative to the coordinate system that rotates with the source (located at point A) and the flat detector. This rotating coordinate system is depicted by blue arrows. Its position relative to the stationary grid defined by (x, y) is given by the view angle θ. O denotes the rotation center (isocenter).

a is defined as in Equation 2.70, and the vertical detector coordinate is given by

$$b(x, y, z, \theta) = z \, \frac{S}{D_{\mathrm{SI}} + x \cos\theta + y \sin\theta}. \tag{2.75}$$

The filtering operation on the pre-weighted projections is not dependent on the vertical coordinate b:

$$\mathcal{Q}_\theta^{\mathrm{cone}}(x, y, z) = \int_{-\infty}^{\infty} \widetilde{\mathcal{P}}_\theta^{\mathrm{cone}}(\omega_a, b) \, |\omega_a| \, e^{i2\pi\omega_a a(x,y)} \, \mathrm{d}\omega_a. \tag{2.76}$$

Note that the Fourier transform is only performed with respect to u.
The filtered projections are backprojected into the three-dimensional reconstruction volume as:

$$f^{\mathrm{cone}}(x, y, z) = \frac{1}{2} \int_0^{2\pi} \frac{S^2}{U(x, y, \theta)^2} \, \mathcal{Q}^{\mathrm{cone}}(x, y, z, \theta) \, \mathrm{d}\theta, \tag{2.77}$$

with U defined as in the fan case, so it is also independent of the vertical coordinate.

The FDK algorithm represents only an approximate approach for a three-dimensional reconstruction: It can be shown that a simple circular source trajectory is not sufficient for sampling the volume with a cone beam in a strict mathematical sense. The farther away the data is from the central slice, i.e. the slice where only a fan, and no cone inclination occurs, the more likely distortions, streaking or shading artifacts are to appear. Hsieh (2009) provides comprehensive examples of typical cone-beam artifacts. Figure 2.15 illustrates that one ray intersects several slices in the cone-beam geometry. The longitudinal extension of the object then poses a challenge, as it is typically undersampled in the upper and lower circular areas shaded in brighter gray. This causes imprecise reconstructed voxel values as a truncation artifact.

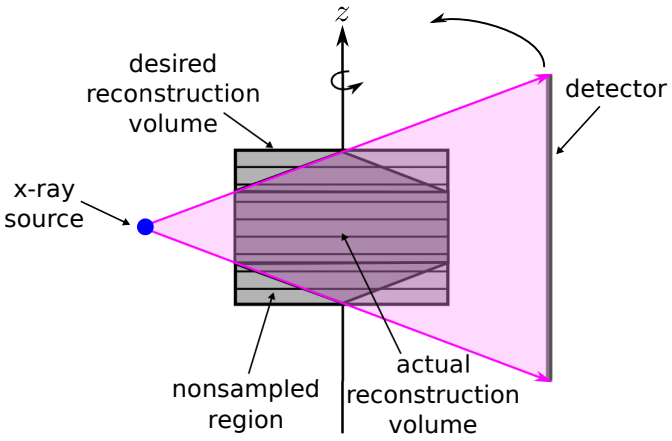

Figure 2.15: Illustration of the problem of longitudinal truncation in cone-beam geometry. Due to the cone opening angle, parts of the object are not sampled, so that the actual reliable reconstruction volume is reduced. Moreover, the sketch shows that rays traverse several slices in the object.

Nonetheless, with small cone angles (as it is also the case in the setup used in this work), the algorithm's precision is sufficient. Moreover, as the cosine function only changes little with angle values close to zero, the Feldkamp weighting is also of minor importance concerning the quantitativeness of the data here, as opposed to strong fan and cone angles in clinical CT. The main contribution of the three-dimensional backprojection here is the geometrically correct representation.
Compared to the simple parallel-beam geometry, fan- and, especially, cone-beam backprojection are computationally much more demanding, because the weighting changes from voxel to voxel in the reconstructed image. However, as the voxel values in the volume can be reconstructed independently from each other, three-dimensional tomographic reconstruction is highly parallelizable. Therefore, for the reconstructions provided in this thesis, an implementation was used that is based on parallelization on graphics processing units. For more information, the reader is referred to Section 3.3.5 and Fehringer et al. (2014).

As introduced in Section 2.3.4, the magnifying geometry influences the measured value of the refraction angle depending on the sample position relative to the phase grating. A similar position dependence is also known for the dark-field signal in the case that the scattering structure sizes are in the range of the grating periods (Yashiro et al., 2011). In case of strong fan angles and samples that are thick compared to the interferometer dimensions, this position dependence should be taken into account in the reconstruction algorithm for a quantitatively correct object representation. This was demonstrated for the phase signal by Qi and Chen (2008) and Chabior et al. (2012) and for the dark-field signal by van Stevendaal et al. (2013). Nevertheless, as the setup used in this thesis still has moderate divergence and thin samples compared to the geometry of clinical human CT scanners, such corrections were neglected in this work.

2.4.5 Principle of iterative reconstruction

The FBP algorithm presented in this chapter is an analytical approach to reconstruct the image volume from projections. As elaborated in Section 2.4.2, many simplifications are necessary to be able to mathematically handle the filtering, weighting and backprojection process. Such simplifications are, for example, that the source is assumed to be perfectly point-like, that the rays are cast as pencil beams through the object, that they are recorded at exactly the center of each detector element, and that the detector is sensitive over its complete area. Moreover, such analytical approaches rely on mathematically sufficient and equidistant sampling. Hence, FBP delivers deteriorated reconstructed images in case of missing data, such as truncated projections, limited-angle tomography or undersampling. An alternative approach is represented by *iterative reconstruction (IR)* algorithms. Not only do they usually cope better with artifacts due to missing data, but they also exhibit an improved noise performance (Hsieh, 2009). Additionally, prior knowledge about the measured object can be included into the iterative reconstruction to reduce artifacts as caused by highly-absorbing materials, such as metal implants.
The principle of iterative reconstruction (IR) shall be briefly summarized here according to Hsieh (2009). A more detailed description is given by Kak and Slaney (2001), and a short review can be found in Hahn (2014).
To describe the iterative approach, the scanned object shall be represented by the vector $\mathbf{f}$. The measured projections are contained in the vector $\mathbf{p}$. To map the measured projections to the object function vector, they can be linked via a matrix operator $\mathbf{A}$ and the error vector $\mathbf{e}$.

$$\mathbf{p} = \mathbf{A} \cdot \mathbf{f} + \mathbf{e}. \tag{2.78}$$

$\mathbf{A}$ is referred to as the system matrix. In the simplest case, the system matrix entries contain the contribution of a voxel in image space to a pixel in the projection space, and the error vector is zero. To model the real conditions more closely, the system matrix can be determined based on the actual physical properties of the CT system (Nuyts et al., 2013), such as focal spot shape, detector response, or geometrical parameters (Hsieh, 2009). The error vector $\mathbf{e}$ accounts for any additive bias.
The reconstruction principle is based on a feedback loop, starting from an estimate of $\mathbf{f}$ given the measurement $\mathbf{p}$. As the system matrix, also called forward-model, is usually very large for CT problems, a direct inversion is not possible and numerical solutions have to be found. The common approach is to formulate a cost function that is to be optimized. In easy words, an estimate of $\mathbf{f}$ is used and forward projected. Forward projection means that the values of the voxels along the particular ray path are summed and assigned as the projection value on the detector. Then, these artificially created projections $\mathbf{p}'$ are compared to the measured projections $\mathbf{p}$. Based on the difference, the estimate of $\mathbf{f}$ is updated. The procedure is repeated, i.e. 'iterated', until a certain convergence criterion, for example a minimal difference between forward projection and measured projection, is reached.
One basic approach which follows this principle is called *algebraic reconstruction technique* (ART). According to how and when the voxel values in the object function are updated, further refined algorithms can be classified into *simultaneous iterative reconstruction technique* (SIRT) and *simultaneous algebraic reconstruction technique* (SART) (Hahn, 2014; Kak and Slaney, 2001).
Algebraic techniques ignore the statistical nature of the measured data, which means they assume noiseless projections. Consequently, a further refinement is given by *statistical iterative reconstruction* (SIR): Here, statistical models of the noise in the acquired data are incorporated into the reconstruction process. Typically, for attenuation-based CT, a Poisson-based counting-statistics model is used (Fessler, 2000). However, the correct modeling of noise in calibrated projection data is difficult and sometimes not straightforward, as often pure Poisson statistics cannot be applied due to alternations by the electronic noise and energy-dependent signals (Hsieh, 2009). Nonetheless, statistical noise models are often used to create a confidence map of the measured projection data. The object function is then updated from projection values that are weighted according to the confidence map. In Section 3.3.5, the statistical iterative reconstruction algorithm by Hahn (2014) that was used for reconstructing phase-contrast, attenuation, and dark-field data in the framework of the present thesis is explained in more detail.

2.5 Contrast agents

Contrast agents come to use in several radiological imaging techniques, if the tissues to be distinguished do not exhibit sufficient contrast. The lack of contrast occurs if the tissues' properties concerning the interaction principle that the imaging technique relies on are too similar. In conventional attenuation-based x-ray imaging, tissue types with strongly differing absorption cross sections due to different average atomic numbers, for example bones and muscle, can be easily differentiated. However, soft-tissue types that have similar average atomic numbers are usually hard to distinguish from each other, for example the inner organs, i.e. liver, kidney, intestines etc. Therefore, x-ray specific radiocontrast agents are often administered to patients to enhance contrast. In fact, about half of the CT scans in the United States of America involve intravenously injected contrast agents (Namasivayam et al., 2006).
A radiocontrast agent changes the average atomic number and density of the tissue or bodily fluid that it is taken up by, which is then exploited as stronger difference in x-ray attenuation. The change can go both ways: Either to a lower density and reduced attenuation, for example by the use of gas such as in carbon-dioxide angiography (Selby, 2008), or to a higher average atomic number and stronger attenuation, for example by using iodine- or barium-based contrast agents. In the latter case, the relatively high atomic number of the elements ($Z = 53$ for iodine and $Z = 65$ for barium) compared to the materials contained in the human body causes increased absorption. A typical application for barium sulfate is the oral ingestion to image the gastrointestinal tract. Iodine-based agents are the most widely-used radiocontrast media. They exist in numerous different versions for various applications such as angiography, urography and many diagnostic questions in abdominal CT imaging.
The reason for the widespread use of iodine is that not many other high-atomic number elements have the chemical characteristics to form soluble compounds with low toxicity. Those that do show biocompatibility are often very expensive, such as gold particles. Lusic and Grinstaff (2013) provide a review about current chemical compounds used as CT contrast media.
Even iodinated contrast media exhibit a non-negligible toxicity, depending on the classification into an ionic or non-ionic compound. In the ionic case, the iodine ion is dissolved into the bodily fluid, whereas in the non-ionic compound it remains bound. Similar to other pharmacological substances, iodinated contrast agents can cause adverse reactions, such as pain at the injection site, nausea, vomiting, and skin rashes or in extreme cases anaphylactoid reactions (Pasternak and Williamson, 2012). Additionally, iodine is found to cause hyperthyroidism and renal dysfunction or failure in some cases (Morcos and Thomsen, 2001; Pasternak

and Williamson, 2012).
A particular feature of iodinated contrast agents is that the characteristic K-edge of the absorption cross section of iodine at $E = 33.169$ keV (Thompson, 2009) can be used for imaging. For this, an image is acquired just below and just above the K energy. Because of the strongly differing absorption, a subtraction of those two images reveals the regions of strong contrast-agent uptake (Riederer and Mistretta, 1977; Bertrand et al., 2005; Schlomka et al., 2008). A similar approach, which has found frequent application in the clinics, is the real-time digital subtraction angiography using iodine or carbon-dioxide: Here, a radiographic projection image is taken of the region where the blood vessels are to be investigated first without contrast agent. Subsequently, contrast agent is injected into the vessel system and another image is taken right after injection as long as the contrast agent portion, referred to as the bolus, is still in the region of interest (Brody, 1982). Immediately, a motion-corrected (Meijering et al., 1999) image subtraction is performed, so that the resulting difference image shows the precise locations of vessel occlusions.
A new trend in x-ray CT contrast agent development is the design of contrast-agent molecules that accumulate specifically to certain tissue types (Lusic and Grinstaff, 2013), for example via receptor binding at cell walls or selective uptake into cells. This biochemical targeting is already widely used in molecular imaging, for example in positron emission tomography (PET) and single photon emission computed tomography (SPECT).
X-ray phase-contrast imaging (PCI) relies on the refraction of x-rays, which is directly related to a change in electron density of the material. Thus, an optimal contrast medium for PCI would be one that exhibits an electron density that strongly differs from the ones in the tissue types of the body. So far, no optimal contrast agent hast been found, partly because, in many cases, the high electron density is coupled to a high atomic number, too, and vice versa. Hence—generally speaking—conventional contrast agents for attenuation-based CT would also increase contrast in the phase measurement.
Nevertheless, the contrast generation in dark-field is worth a closer inspection: Here, many interfaces between small structures of different (electron) densities cause the signal, and not so much the overall average difference between densities of different tissues. Thus, a contrast agent that introduces as many interfaces as possible into the beam path between materials with densities as different as possible would be favorable to increase the dark-field signal. In Chapter 4, the use of small bubbles for exactly this purpose is studied.

Chapter 3

Imaging with the small-animal scanner

In this chapter, after a brief motivation, the dedicated phase-contrast and dark-field small-animal scanner is presented shortly along with its technological issues concerning system characteristics and stability. Several different software-based tools to reduce the image artifacts arising from those issues, both in the processing, and in the tomographic reconstruction step, are introduced. To demonstrate the correction effects in the processing and reconstruction framework, imaging results of a simple phantom and a plastic figure as well as a high-performance scan of an ex vivo mouse are shown. Furthermore, the first in vivo projection image results of a healthy mouse and the first in vivo dark-field and phase-contrast CT scans of a healthy mouse and two mice with pulmonary diseases are presented. The in vivo projection results have been published previously in Bech et al., "In-vivo dark-field and phase-contrast x-ray imaging", Scientific Reports (2013), whereas the CT results have been submitted for publication as Velroyen et al., "X-ray dark-field computed tomography of living mice". The chapter concludes with a summary and outlook on further technological developments concerning small-animal PCI and dark-field imaging (DFI).

3.1 Motivation

Grating-based x-ray phase-contrast imaging was first made available in the early 2000s (David et al., 2002; Momose et al., 2003; Momose, 2005; Weitkamp et al., 2005) and grating-based dark-field imaging was first presented only shortly afterwards (Pfeiffer et al., 2008). First benchmarking studies concentrated on high-

performance scans of small and mostly fixated biological and biomedical specimens at large-scale synchrotron facilities using highly brilliant x-rays and high-resolution setups to demonstrate the imaging potential of the technique (Momose et al., 2006; Pfeiffer et al., 2007a; Donath et al., 2010; Schulz et al., 2010). After Pfeiffer et al. (2006, 2007b, 2008) had proven the feasibility of x-ray grating-interferometry with a conventional polychromatic x-ray source by introduction of a source grating, the investigation of the technique moved towards the identification of possible clinical applications (Stampanoni et al., 2011; Stutman et al., 2011; Schleede et al., 2012; Sztrókay et al., 2013; Fingerle et al., 2014; Herzen et al., 2014; Hetterich et al., 2014). Efforts were undertaken to push technological limits of the method, for example by performing imaging at high energies (Willner et al., 2013), developing alternative (shorter) acquisition schemes (Bennett et al., 2010), and by stitching of gratings for a larger field of view (Meiser et al., 2014). One of those steps towards clinical application was translating the method from bench-top setups that contain a fixed source, detector and interferometer and a rotatable sample stage to a table-top scanner with fixed sample-stage (i.e. animal bed) and rotatable gantry comprising source, detector and grating interferometer in order to facilitate *in vivo* imaging. Because of the complexity and degree of optimization required by state-of-the-art human-body sized CT scanners and technological limits concerning the size of the gratings this effort was first undertaken for a compact small-animal setup. It was tackled within a preceding doctoral thesis by Tapfer (2013), which focused on the technological development of the small-animal x-ray phase-contrast and dark-field CT scanner 'Skyscan 1190' in collaboration with the industrial partner *Bruker microCT* (formerly *Skyscan*). The thesis describes the first commissioning results from the scanner, such as stability measurements, hardware improvements, and feasibility demonstrations of quantitative phase-contrast CT imaging with a rotating gantry (Tapfer et al., 2011, 2012).

The work presented in this chapter directly connects to the preceding thesis and takes the venture of *in vivo* imaging one step forward. The methodological part focuses on the application of algorithmic solutions to counteract image artifacts arising from the scanner's particular challenges concerning stability and setup characteristiscs (discussed in Section 3.2). For this purpose, phantom measurements as well as an *ex vivo* mouse scan are presented. Subsequently, the first actual *in vivo* imaging results from the scanner are presented. They take advantage of and are partly only feasible because of those software algorithms. These very first PCI and DFI results of living mice performed with an x-ray grating interferometer on a rotating gantry comprise simple projection radiography (Bech et al., 2013) as well as computed tomography (Velroyen et al., b). The breakthrough of demonstrating *in vivo* applicability of the method constitutes an important milestone

for its translation into clinics, which is the ultimate goal. Moreover, the feasibility of dose-compatible preclinical small-animal DFI (and PCI) radiography and CT allows for studies on the identification and evaluation of pathologies for which the novel x-ray modalities can add diagnostic benefit. Section 3.6 provides an example on the increased information gained by dark-field computed tomography (DFCT) on two pulmonary disorders.

3.2 The scanner setup: characteristics and shortcomings

The results presented in this chapter were acquired with the unique dedicated small-animal x-ray phase-contrast and dark-field CT scanner "Skyscan 1190" developed in collaboration with *Bruker microCT*, Kontich, Belgium. For a detailed insight into the development considerations the reader is referred to the preceding doctoral thesis "Small animal X-ray Phase-Contrast Imaging" (Tapfer, 2013). Here, only the specifications relevant to the tools and results presented below are given.

3.2.1 Scanner specifications

The scanner is a table-top system equipped with a rotatable mechanical gantry and a stationary sample stage in the form of an animal bed. The setup design is unique considering that usually the sample is rotated for tomographic image acquisition in existing phase-contrast setups. The rotating gantry comprises a flatpanel detector (Hamamatsu C9312SK-06) comprised of a Gadolinium oxysulfide scintillator and a cooled 12-bit CCD camera with 2496×2304 pixels and 50 µm pixel size, a mini-focus x-ray tube source (RTW, MCBM 65B-50 W) with a tungsten target and a focal-spot diameter of approximately 50 µm, and a Talbot-Lau interferometer. The three gratings of the interferometer, fabricated by *microworks*, Karlsruhe, Germany, are described by the following grating bar materials, heights and periods, respectively: source grating G0 - gold, 35 µm, 10 µm; phase grating G1 - nickel, 4.0 µm, 3.2 µm; analyzer grating G2 - gold, 25 µm/45 µm, 4.8 µm. Note that the original G2 with a height of 25 µm, as introduced in Tapfer (2013), was only used in the measurement of the plastic toy presented in Section 3.3.4 and the first *in vivo* projection images presented in Section 3.5. The grating was subsequently replaced by one with 45 µm high bars to increase visibility. The source grating is equipped with a piezo stepper motor and can also be rotated. The phase grating is motorized to be moved in any of the three directions and

can also be tilted in two directions and rotated to allow for a proper aligment of the gratings. The distances between focal spot and G0, G0 and G1, and G1 and G2 are 31 mm, 300 mm and 145 mm, respectively. Hence, the interferometer is operated at first fractional Talbot distance and laid out for a design energy of 23 keV. The phase grating is laid out to introduce a phase shift of $\pi/2$ to x-rays of this energy. Source and sample are 270 mm apart, whereas sample and detector have a distance of 200 mm. Thus, the total length is small compared to bench-top setups, which results in a moderate cone-beam geometry. However, it is strong enough to be necessarily considered during tomographic reconstruction. The cone-beam geometry leads to an effective pixel size of 29 µm.* The aforementioned visibility boost by introducing the higher G2 grating comes at the cost of increased noise due to the fan opening of the beam. The non-parallel beam path causes increased shadowing of the x-rays in the peripheral grating regions on the left- and righthand side of the considered field of view.
The scanner's facilities to monitor breathing motion via video-tracking, as well as heart beat and temperature, allow for in-vivo experiments in small rodents. A built-in warm-air fan is available to stabilize the body temperature of anesthetized animals.
Images are acquired using the proprietary Skyscan control-software, which delivers phase stepping sets of raw projection images of data type Tagged Image File Format (TIFF), a main text-based log file containing scanner specifications and acquisition parameters and an additional text-based log file for the system temperature over the course of the scan.

3.2.2 Stability issues and artifacts

Since the scanner is the first system to have a Talbot-Lau interferometer installed on a rotating gantry, the stability of the phase-sensitive imaging setup during acquisition is of great interest. With grating periods in the micrometer range, drifts or vibrations on the scale of fractions of micrometers can cause severe artifacts when retrieving phase or visibility information. A thorough stability analysis can be found in Tapfer (2013) and shall be shortly summarized here: To evaluate the unsteadiness of the interferometric pattern, repeated phase stepping scans were acquired with an empty field of view under two different conditions and the relative phase of the interferometric fringes was analyzed. First, a measurement with a static gantry over a long period of time after starting the x-ray source

*The effective angular opening in vertical and horizontal direction depends on the size of the field of view of interest, i.e. the cropping of the projections that are used in the reconstruction. For example the coronal slices of the *ex vivo* mouse presented in Section 3.4 cover a fan angle in the horizontal direction of approximately 7.0° and a vertical angle of about 3.1°.

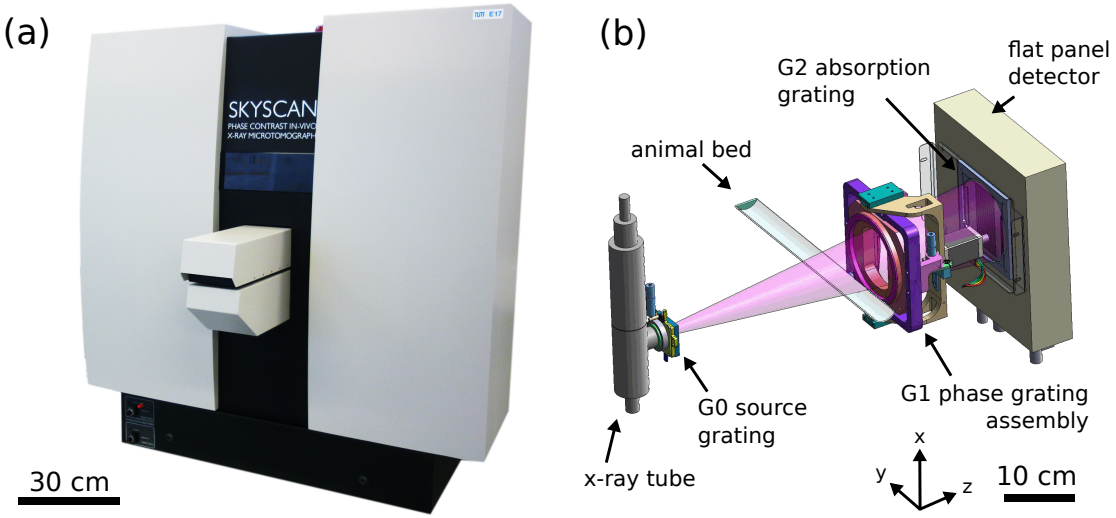

Figure 3.1: Phase-contrast and dark-field small-animal CT scanner with rotating gantry. (a) Photograph of the Skyscan 1190. (b) Setup that is installed on the rotating gantry (Image courtesy B. Pauwels).

revealed that the phase drifts by about $1.5\,\pi$ between the start-up moment and a relatively stable condition after approximately 3 hours. This can be explained by heating-up of the system, in particular of the source grating and its mounting structure, and by the resulting thermal expansion of the material. Additional phase drifts in the order of $\frac{\pi}{2}$ rad are observed over the course of 24 hours due to day-night ambient temperature changes in the laboratory where the scanner is located. Second, repeated measurements of the relative phase during a full gantry rotation initially revealed a systematic drift over the range of approximately $14\,\pi$ caused by the gravitational force that severely affects the relative alignment of the gratings depending on the current gantry angle. In the course of Tapfer's work this was amended by installing alignment motors with zero-backlash gears and a mechanical spring on the holding structure of G1 to counteract the gravitational force, improving the drift range to $6\,\pi$.

To understand how the instable grating aligment causes artifacts, two effects have to be considered: On the one hand, the gratings that are commonly used in Talbot-interferometry setups are non-perfect periodic structures due to difficulties in the complex production process. Local variations in grating quality along with imprecise alignment cause the superposition of periodic structures to be imperfect. In consequence, intensity variations of a certain beat frequency are overlaid onto the raw projection image. Figure 3.2a shows exemplarily how two periodic structures with slightly different periodicity and a minor relative tilt cause a su-

perimposed medium-range fringe. The formation of those so-called Moiré fringes was described mathematically in detail by Weitkamp et al. (2004) and analyzed further by Hermville (2013). Figure 3.2b shows an example of a raw projection with such a Moiré fringe caused by non-perfect gratings and deviations in the alignment.
On the other hand, Moiré fringes only pose a problem when perfoming PCI/DFI with the phase stepping method if the fringe pattern does not remain stable. If mechanical or thermal influences cause the fringe pattern to drift, as it is the case in the discussed setup, the pattern cannot be canceled out anymore by the flat-field correction contained in the standard processing as described in Section 2.3.3. This results in remaining Moiré fringes with medium frequency as well as long-range phase variations over the whole field of view that are not caused by the sample (see Figure 3.5 and Figure 3.6, respectively). In Section 3.3.4 an extended adaptive phase recovery algorithm is presented to correct for medium-range phase variations. In Section 3.3.3.2 the application of an alternative processing approach is demonstrated, which takes additional uncertanties into account and is able to deal with residual Moiré fringes.

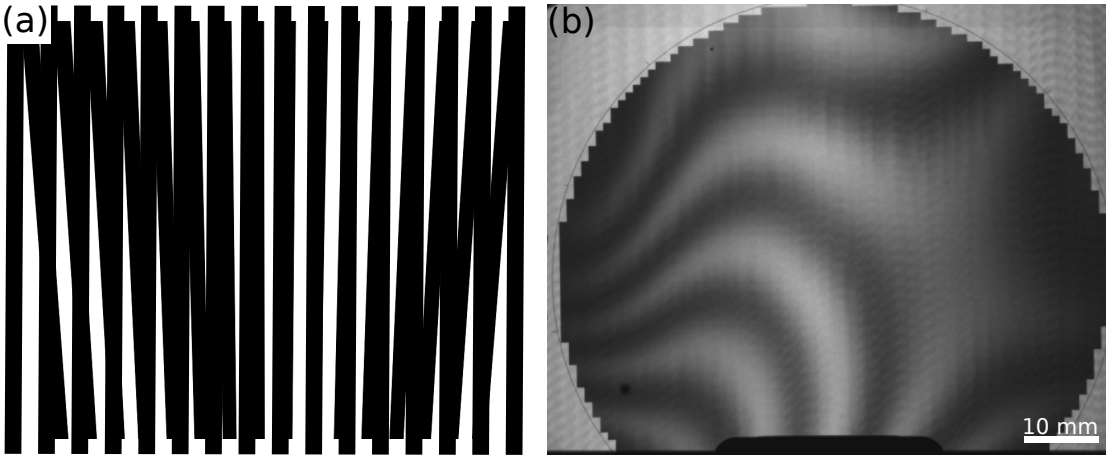

Figure 3.2: Examples for Moiré fringes. (a) Illustration of Moiré fringes that are generated by two overlaying periodic structures with relative tilt and rotation and mismatching periods. (b) Raw detector image from Skyscan 1190 CT scanner with visible superposition Moiré fringes. The round structure indicates the field-of-view coverage by the phase grating.

3.2.3 Spatial system response

The sharpness with which an imaging system depicts features of the sample is influenced by several of the system's properties such as focal-spot size of the source or interaction depth and light spread in the detector's scintillator material (see

Section 2.2). The overall spatial system response can be described by, for example, the system point-spread function (PSF). The PSF describes the blurring of an ideal point object caused by the system response.
The spatial system response of the scanner has been intensively characterized using various methods and is described in the diploma thesis "Experimental characterization of the first preclinical X-ray phase-contrast CT scanner" (Müller, 2013). In one approach, the system response to a sharp edge that is placed in the sample plane of the scanner was measured and fitted in horizontal direction. From this fit, the line spread function (LSF) was deduced via derivation and then rotated, so that a symmetrical PSF was obtained. Other approaches described in the thesis justify the assumption that the spatial system response of the scanner is approximately radially symmetric. Thereby, LSFs/PSFs for 1×1, 2×2 and 4×4 detector binning were determined and are presented in Figure 3.3.

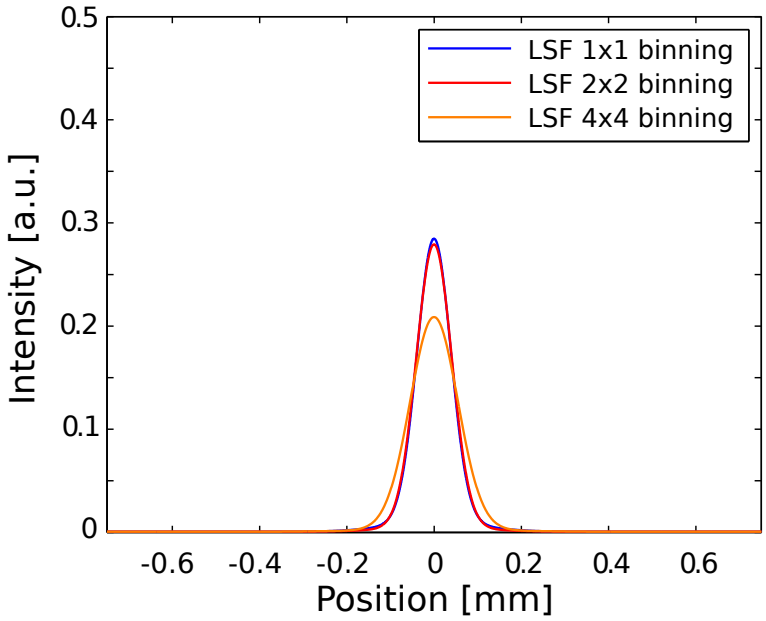

Figure 3.3: Measured line spread functions (LSFs) describing the spatial system response of the Skyscan 1190 for three different detector binning modes. The graph was adapted from Müller (2013).

As the line-spread function (LSF) was determined from the sharp edge placed in the sample plane, both the blurring contributions from the source and the detector are included. However, Müller (2013) showed that, at this position, the detector influence dominates, so that the contribution of the focal spot size to the LSF in Figure 3.3 is negligible.
In Section 3.3.2 a software tool is presented that utilizes the PSF information to enhance image sharpness by deconvolving raw images with the blurring function.

3.2.4 Scan time

Compared to commercially available conventional preclinical CT systems, the acquisition time at the Skyscan 1190 is rather long. This can mainly be attributed to two effects. First, to the necessity of the phase stepping method to acquire several (at least 3) projections per tomography angle and, second, to rather low flux of the source and poor sensitivity of the detector, when the system is operated at source voltages of 30 to 35 kVp, which are preferred because of optimal visibility of the interferometer. For proof-of-concept phantom and *ex vivo* studies, long scan times of several hours or days for a tomography do not pose a problem, but for *in vivo* CT imaging, restrictions apply. Since the scanner is not (yet) equipped for gas anesthesia, which in principle could be applied in a stable condition for long periods of time, the animals had to be anesthetized by injection anesthesia. This limits the measurement duration to about two hours, because accidental overdose is to be avoided.
Due to the scan-time restriction, only highly undersampled tomography scans could be acquired for the *in vivo* case. Therefore, a reconstruction option alternative to conventional FBP had to be applied: Section 3.3.5 shortly introduces a statistical iterative reconstruction algorithm for this purpose.

3.3 Improved signal recovery by means of software correction

The shortcomings of the setup described in Section 3.2 cause various artifacts in phase projections and tomographies. In this section, novel processing tools and an alternative tomographic reconstruction approach are presented shortly. Imaging examples are given, where the new measures helped to overcome the described issues.

3.3.1 General functionalities of processing framework

A purpose-built processing framework was set up from scratch to fulfill two goals: first, to meet the requirements that a semi-commercial image acquisition system poses to the signal extraction and post-processing pipeline, and, second, to efficiently use existing software libraries of the research group at the same time. Therefore the high-level programming language *python* was used.
To connect to the commercial front-end, the framework reads the text-based log

file produced by the acquisition software and automatically imports scanning parameters necessary for processing (for example number of steps, detector binning mode etc.) as well as the TIFF files that comprise the scan. This is done by simply calling the processing script in a command line and providing the path of the logfile as argument.
To remain compatible with the commercial reconstruction software NRecon by *Bruker microCT*, the framework automatically generates modality-specific log files that are required by NRecon as well as output in form of compatible TIFF files if desired. For maximal flexibility and compatibility with other existing post-processing and reconstruction scripts in the research group, the standard output format of the processed image stacks is *.hdf*. A text-based log file for easy access to the used processing parameters is automatically created.
Within the script call the user can choose from an abundance of options documented in the "usage" description, which can be reviewed via "-h". Some examples are given in Appendix A.1. The functionality to call the processing from command line rather than via a graphical user inferface was chosen to facilitate batch processing. Thereby, a shell script can be used for automatized launching of several subsequent processing jobs.

3.3.2 Deconvolution with system point-spread function

In general, the output signal of a linear, shift-invariant imaging system can be mathematically described by the input signal convolved with the imaging system impulse response. Since this impulse response, here described by the PSF, is the resolution-limiting factor, improving the resolution can be achieved by deconvolution of the output signal with the known PSF. One commonly used approach for deconvolution of a blurred image is the Richardson-Lucy (RL) algorithm (Richardson, 1972; Lucy, 1974). It is based on a maximum-likelihood estimation of the deconvolved image, which is iteratively updated after comparing its convolution with the PSF to the measured signal. It contains the assumption of Poisson-distributed noise, which is typically the case in counting statistics of raw detector images.

The derivation and implementation of the algorithm for application to raw phase-stepping data was first performed by D. Hahn and is described in detail in his thesis (Hahn, 2014). The present work takes this approach one step further by performing the RL deconvolution with the aforementioned measured actual PSF of the system for different detector binning modes, rather than a guessed or assumed Gaussian PSF. The kernel sizes of the PSF were 9×9, 3×3, and 2×2 for

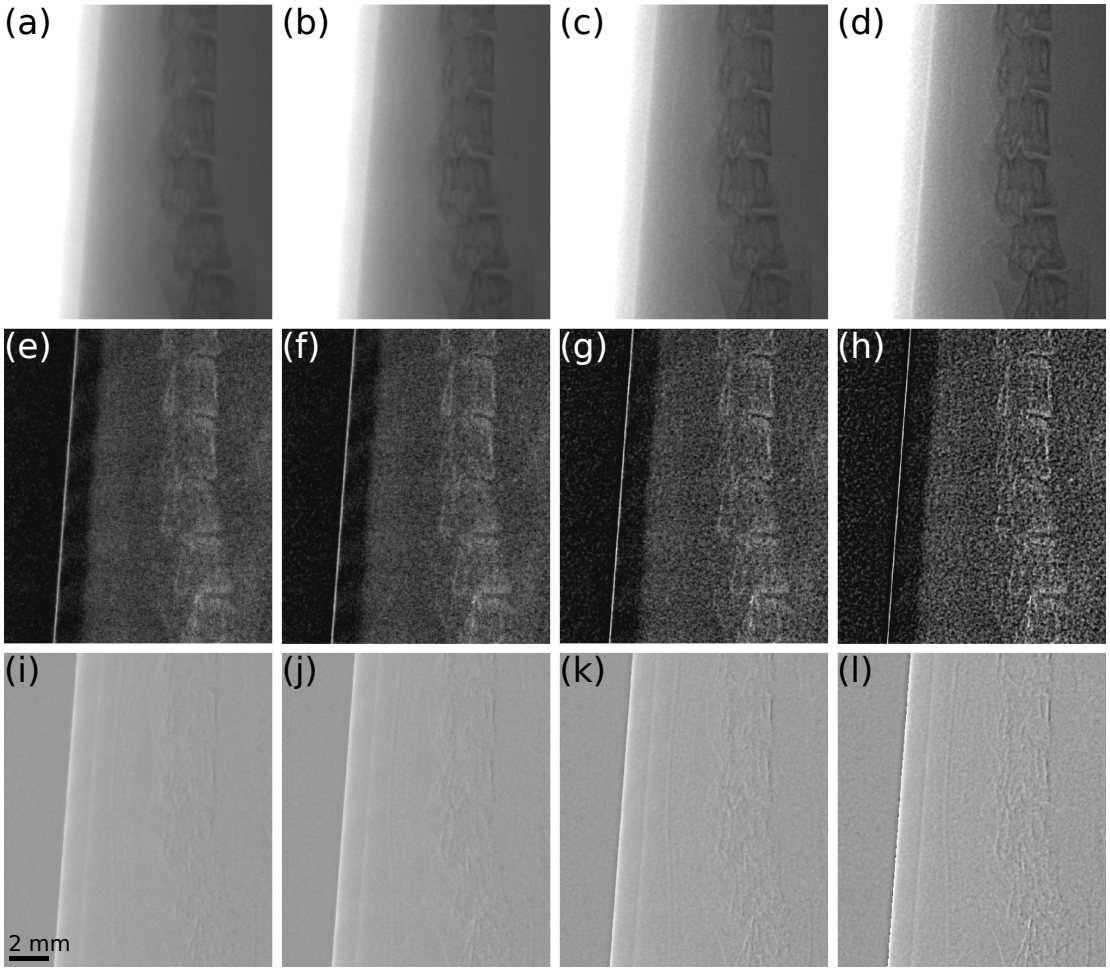

Figure 3.4: Detail of trimodal projection images of a formalin-fixated *ex vivo* mouse processed with increasing number of deconvolution iterations. (a)-(d) Attenuation. (e)-(h) Dark field. (i)-(l) Differential phase. Columns from left to right: No deconvolution, one iteration, three iterations, five iterations.

1×1, 2×2, and 4×4 binning, respectivly.

Figure 3.4 shows exemplary absorption, dark-field and differential phase images of a formalin-fixated *ex vivo* mouse in a plastic tube. The RL deconvolution operation was applied to the raw stepping images prior to trimodal signal extraction with increasing number of iterations (For details about the scan parameters, see Section 3.4). Only a detail of the spine of the mouse next to the edge of the plastic container is shown to demonstrate the effect of the deconvolution and artifacts that can arise.

The leftmost column shows the original absorption, dark-field and differential phase projections with no deconvolution applied. From left to right, the number

of iterations increases from zero to one, three and five. It is clearly visible that the sharpness of the bone features increases with the number of iterations in all three modalities. However, the image series demonstrates a typical property of the RL deconvolution: Along with the feature sharpness, also the noise in the image is highly pronounced. Hence, a trade-off between feature sharpness and noise has to be found by tuning the number of iterations (Zech, 2013). Since absorption, dark-field and phase exhibit different specific noise behaviour (Chabior, 2011) the optimal number of iterations can deviate for different modalities. In Figure 3.4, the dark-field images exhibit stronger noise than the absorption images, as they display a very granular noise structure already at low numbers of iterations. Therefore, for these dark-field images one iteration would be the recommended maximum, whereas the absorption image remains sufficiently smooth at three iterations and only starts to exhibit too much granularity at five iterations. In the differential phase image it is visible that over-regularization by the RL algorithm can increase statistical phase wrapping and over- and undershooting[†] at strong edges such as at the container edge and at the vertebra, as can be seen in Figure 3.4l.

3.3.3 Alternative signal-extraction methods

In addition to the standard processing to extract attenuation, differential phase and dark-field signal from a raw stepping series, as presented in Section 2.3.3, the processing framework for the Skyscan data contains two alternative methods that either deliver more information about the signal (Section 3.3.3.1) or can cope with unstable stepping data (Section 3.3.3.2).

3.3.3.1 Statistical phase retrieval

The intensity curve that is measured during the stepping procedure of a Talbot-Lau interferometer is usually described by the intensity curve model function as introduced in Section 2.3.3

$$I(x) = a_0 + a_1 \cos\left(\frac{2\pi}{p_2}x - \phi_1\right), \tag{3.1}$$

with p_2 being the period of the interferometric pattern. The most commonly used method to extract the parameters a_0 (mean), a_1 (amplitude) and ϕ_1 (relative

[†]Over-/undershooting denotes a phenomenon where at a step or spike in the image the gray values right next to the feature are significantly lower or higher than the actual true gray value levels.

phase) in order to retrieve transmission, dark-field and differential phase signal is the Fourier approach described earlier. The drawback of this fast approach is that it cannot deliver the statistical uncertainties of the three signal channels, which are required for the statistical iterative reconstruction technique (see Section 3.3.5). Therefore the statistical phase retrieval (SPR) introduced by Hahn (2014) was incorporated in the scanner-specific processing framework. The following short summary of the algorithm and the notations are adapted from the cited thesis. The technique applies a weighted least-squares (WLS) fit to the sinusoidal curve that describes the measured intensities in each pixel. For this estimation to be applicable, the description of the stepping curve has to be rewritten in a linearized version

$$I(x) = A_0 + A_1 \cos\left(\frac{2\pi}{p_2}\, x\right) + B_1 \sin\left(\frac{2\pi}{p_2}\, x\right), \tag{3.2}$$

with the conversion between the parameter sets as follows:

$$a_0 = A_0, \quad \phi_1 = \arctan\frac{B_1}{A_1}, \quad V = \frac{\sqrt{A_1^2 + B_1^2}}{A_0}, \tag{3.3}$$

with the visibility $V = a_1/a_0$. By introduction of the estimated-parameters vector $\mathbf{a} = (A_0, A_1, B_1)^T$ and the basis-functions vector $\mathbf{X}(x) = (1, \cos(\frac{2\pi}{p_2}\, x), \sin(\frac{2\pi}{p_2}\, x))^T$ a WLS cost function can be defined as

$$S = \sum_{i=0}^{N-1} \frac{1}{\sigma_i^2} \left[I(x_i) - \sum_{j=0}^{M-1} a_j \cdot X_j(x_i) \right]^2, \tag{3.4}$$

where M denotes the total number of basis functions and estimated parameters and N stands for the total number of stepping positions. σ_i is the statistical uncertainty of the intensity measurement in the pixel for stepping position x_i. Since the main contribution to noise is basic counting statistics, the uncertainty can be described by a Poisson noise model, i.e. $\sigma_i = \alpha\sqrt{I_i}$ with $\alpha = 1$, if I directly represents photon counts.
To obtain A_0, A_1, and B_1, as well as their uncertainties σ_{A_0}, σ_{A_1}, σ_{B_1}, the WLS problem is solved by calculating the gradient of Equation 3.4 with respect to each of the estimation parameters and setting it equal to zero. For a more detailed description as well as the numerical implementation, the reader is referred to Hahn (2014), Section 3.2 and Appendix A.1. Solving the derived system of equations yields the solution vector $\mathbf{a}$ as well as its variances and covariances. Standard Gaussian error propagation leads to the statistical uncertainties of the original stepping-curve parameters (for more comprehensive display here without

covariances)

$$\begin{aligned} \sigma_{a_0} &= \sigma_{A_0}, \\ \sigma_{\phi_1} &= \sqrt{\frac{A_1^2\sigma_{B_1}^2 + B_1^2\sigma_{A_1}^2}{A_1^2+B_1^2}}, \\ \sigma_V &= \sqrt{\frac{(A_1^2+B_1^2)\sigma_{A_0}^2}{A_0^4} + \frac{A_1^2\sigma_{A_1}^2 + B_1^2\sigma_{B_1}^2}{A_0^2(A_1^2+B_1^2)}}. \end{aligned} \tag{3.5}$$

This procedure is applied to a stepping set with sample and one with an empty beam (called flatfield or reference), denoted by the subscripts 's' and 'r', respectively. For the three signal channels that are fed into the tomographic reconstruction, i.e.

$$\mathcal{T} = -\ln\frac{a_\mathrm{s}}{a_\mathrm{r}}, \quad \phi = \arg\left(e^{i(\phi_\mathrm{s}-\phi_\mathrm{r})}\right), \quad \mathcal{V} = -\ln\frac{V_\mathrm{s}}{V_\mathrm{r}} \tag{3.6}$$

again, the uncertainties are determined via error propagation:

$$\sigma_\mathcal{T}^2 = \frac{\sigma_{a_\mathrm{s}}^2}{a_\mathrm{s}^2} + \frac{\sigma_{a_\mathrm{r}}^2}{a_\mathrm{r}^2}, \quad \sigma_\phi^2 = \sigma_{\phi_\mathrm{s}}^2 + \sigma_{\phi_\mathrm{r}}^2, \quad \sigma_\mathcal{V}^2 = \frac{\sigma_{V_\mathrm{s}}^2}{V_\mathrm{s}^2} + \frac{\sigma_{V_\mathrm{r}}^2}{V_\mathrm{r}^2}. \tag{3.7}$$

Equations 3.6 and 3.7 provide a direct quick and analytical access to the three interferometric signal channels and their uncertainties, which are exploited in the statistical iterative reconstruction algorithm (see Section 3.3.5).

3.3.3.2 Expectation maximization algorithm for unstable stepping

The mechanical and thermal fluctuations described in Section 3.2 can influence the measured intensity curve during a phase-stepping scan. Therefore, systematic fluctuations, denoted by Δs, ΔI and ΔV, are assigned to the stepping positions $s_i = \frac{2\pi}{p}\, x_i$ (with p being the period of the grating being stepped) as well as to the intensity I and to the visibility V of the interferometric pattern.
These fluctuations are unknown and thus contribute to the number of parameters that describe the stepping curve and are to be extracted. Hence, the number of measured values is not sufficient anymore, so that an underdetermined linear system of equations is obtained. Neither SPR nor the standard Fourier analysis processing are applicable in this case.
To overcome this problem, G. Potdevin suggested a processing method based on an expectation-maximization (EM) algorithm (Dempster et al., 1977; Do and Batzoglou, 2008) as a more versatile processing approach (manuscript in preparation). The numerical implementation into python code functions was accomplished by G. Potdevin. Function calls with appropriate starting parameters and thresholds were incorporated into the scanner processing framework to allow the application

of the algorithm to unstable stepping data of the rotating-gantry CT scanner. The following short summary of the principles of this algorithm is adapted from an internal version of the manuscript draft.
Similar to the SPR approach, the intensity curve of the phase-stepping scan is described by a periodic function of sinusoidal shape:

$$I(s_i, k) = \sum_{n=0}^{N-1} \alpha_n \, A_n(k) \, \cos(n \, s_i) + \beta_n \, B_n(k) \, \sin(n \, s_i), \tag{3.8}$$

where k denotes the pixel index, $s_i = \frac{2\pi}{p} x_i$ the stepping positions, p the period of the grating being stepped and n the order of the expansion. Usually only zeroth and first order are considered. While the $A_n(k)$ and $B_n(k)$ are equivalent to the parameters introduced in Equation 3.2, the α_n and β_n are linked to the fluctuations as follows:

$$\Delta I = \alpha_0, \quad \Delta V = \sqrt{\alpha_1^2 + \beta_1^2}, \quad \Delta s = \arctan \frac{\alpha_1}{\beta_1}. \tag{3.9}$$

Thereby, the fluctuations are considered as hidden (latent) variables in the EM algorithm. A log-likelihood function is defined as

$$- \log \mathcal{L} = \sum_k \tfrac{1}{\sigma(k)^2} \left[\sum_i \left(I(s_i, k) - \sum_{n=0}^{N-1} \alpha_n \, A_n(k) \, \cos(n \, s_i) + \beta_n \, B_n(k) \, \sin(n \, s_i) \right)^2 \right]. \tag{3.10}$$

The inner sum over i establishes the consistency of the measured intensity $I(s_i, k)$ in each pixel for all raw projections of the stepping set with the model, whereas the outer sum over k ensures consistency of the intensity with the model within one raw projection. $\sigma(k)$ weights the pixels assuming Gaussian noise. This approach also makes the assumption that all measurements are independent and identically distributed.
The EM algorithm can then be described in three steps:

1. A first initial guess of the stepping position and fluctuation is made, usually the values that they should reach in an ideal measurement: $s_i = i\frac{p}{N}$, $\Delta I = 1$ and $\Delta V = 1$, with N the number of stepping positions.

2. With the guessed s_i, ΔI and ΔV, the parameters A_n and B_n, or a_0, a_1 and ϕ_1 are calculated by solving a system of equations using linear

least-squares fitting as described in Section 3.3.3.1. This step corresponds to evaluating the inner sum of Equation 3.10 to ensure consistency of the Fourier expansion in each pixel with respect to the measured intensities.

3. With the parameters a_0, a_1 and ϕ_1 calculated in step 2, the optimal Δs_i, ΔI and ΔV for each projection are evaluated by solving another linear system of equations in the form of

$$\begin{pmatrix} A_0(1) & A_1(1) & B_1(1) \\ A_0(2) & A_1(2) & B_1(2) \\ \vdots & \vdots & \vdots \\ A_0(k) & A_1(k) & B_1(k) \end{pmatrix} \cdot \begin{pmatrix} \alpha_0 \\ \alpha_1 \\ \beta_1 \end{pmatrix} = \begin{pmatrix} I(1) \\ I(2) \\ \vdots \\ I(k) \end{pmatrix}. \tag{3.11}$$

This step corresponds to evaluating the outer sum of Equation 3.10 to ensure consistency of the intensity variations across pixels.

Those steps are repeated until convergence is reached. The convergence criterion implemented is that Δs_i, the change of the value of s_i between successive iterations is sufficiently small. To avoid converging to local extrema, good starting values have to be provided to the EM algorithm. Fortunately, this is usually no problem in case of phase stepping, since the stepping positions usually vary only by a limited amount from the ideal positions. The retrieval of the s_i, ΔI and ΔV by the EM algorithm is only possible in a relative manner, i.e. there exists an unknown additive constant. This constant can be subsequently corrected for by the extended adaptive differential phase recovery (Section 3.3.4) and a simple offset-correction for absorption and dark-field image using an uncovered part of the field of view. The EM procedure is also applied to the measured reference phase stepping sets, since those are also subject to fluctuations. Therefore, the correction achieved by the EM algorithm comes at the cost of a prolonged processing duration by a factor of approximately twice the number of iterations (usually 5-10 iterations were necessary until convergence).
Figure 3.5 shows an example of a differential phase projection of a water-filled plastic tube, which shows clear residual Moiré fringes due to instabilities when processed with the SPR method (a), but no remaining fringes, when processed with the EM algorithm (b). The effect of this successful fringe removal on a reconstructed tomographic dataset is displayed in Figure 3.7. Slices (c) and (g) were reconstructed from SPR-processed projections and show patches and fringes in the homogeneous sample region, whereas slices (d) and (h) were reconstructed from EM-processed projections and show a homogeneous area.

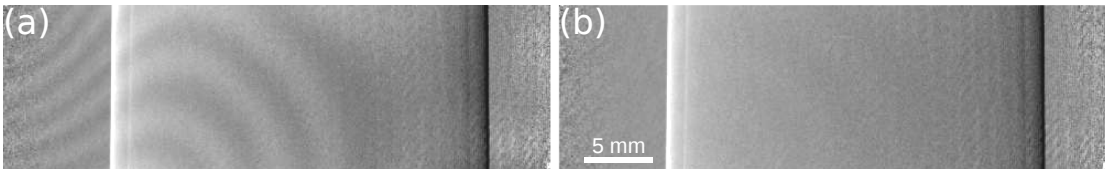

Figure 3.5: Differential phase projection of a water-filled tube. Gray values are scaled from $-\pi/4$ to $\pi/4$. (a) Projection processed using standard sine-fit algorithm. Residual Moiré fringes are strongly visible. (b) Projection processed using expectation-maximization algorithm, that takes stepping position and intensity as hidden variables into account. No residual Moiré fringes are visible.

3.3.4 Extended adaptive differential phase recovery algorithm

The mechanical and thermal drifts between different gantry positions and between the time points of sample and blank scan cause a locally varying offset in the conventionally processed differential phase image (Figure 3.6a). A straightforward solution would be to record a flatfield projection instantly after each angular sample projection, but this approach is very time consuming, because it requires moving the sample stage out of and back into the FOV. To increase acquisition speed, a typical scan scheme can be applied as follows: A set of blank images is recorded each time a certain number of sample projections has been acquired, corresponding to a block of angular positions. Another, even faster, option is to first complete a full sample-scan tomography rotation and subsequently perform a separate, but identically spaced, blank tomography. The drawback is that, depending on the acquistion duration of the tomography, this acquisition scheme can exhibit severe deviations due to thermal variations.
To compensate for the drifts occurring between sample and blank scan, Tapfer already introduced adaptive differential phase recovery (ADPR) in his thesis (Tapfer, 2013). This procedure works as follows: Each value $I(x, y)$ in the processed differential phase image is tranformed into its complex exponential via $I'(x, y) = e^{i \cdot I(x,y)}$. This is done, because the periodic nature of the function allows to deal with phase wrapping that occurs in the image because the background distortion causes the signal to shift over the $\pm\pi$ limit (Tapfer, 2013). In the complex plane, the gradient of all image pixel values is determined and averaged for x and y direction. From those averaged gradients, an inclined plane is defined that is subsequently subtracted from the image. Additionally, a remaining constant offset of the phase value is determined by evaluating the signal in default background regions, where no sample covers the field of view. This offset is subtracted from the complex image values. Ultimately, the image values are transformed back to the angle argument of the complex plane.

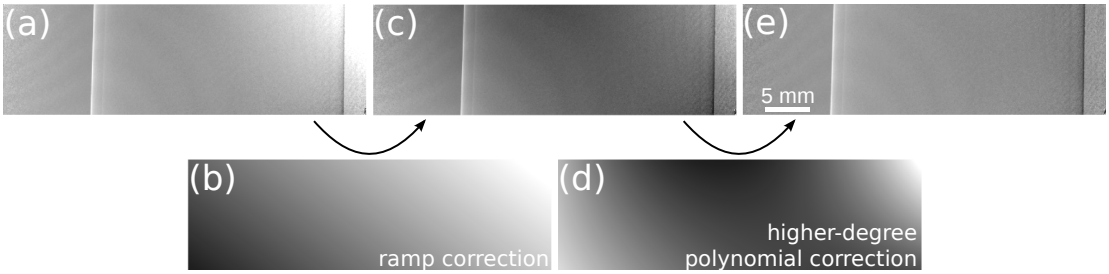

Figure 3.6: Exemplary differential phase projection of a water-filled plastic cylinder and different stages of the adaptive differential phase recovery. Gray-value scaling is given in brackets. (a) Uncorrected projection with a strong background distortion [$-\pi/2$, $\pi/2$]. (b) Angle of complex ramp fit to background gradient of the projection, scaled to minimum and maximum value [0.005, 1.494]. (c) Projection with remaining higher-degree distortions after subtraction of ramp fit [$-\pi/2$, $\pi/2$]. (d) Surface fit of polynom with degree 2 to background distortions of the projection on (c), scaled to minimum and maximum value [-0.903, 0.823]. (e) Flat projection after subtraction of surface fit [$-\pi/2$, $\pi/2$].

Daily practice with tomography data acquired at the preclinical CT scanner revealed that ADPR in the described form is not sufficient for correcting background phase distortions. Figure 3.6 illustrates a case of a differential phase projection that still shows a remaining distortion after applying ADPR in the previously described form (Fig. 3.6a and b). It is clearly visible that this distortion cannot be described by a ramp, but only by a polynomial of higher degree (see Figure 3.6c). Therefore, ADPR was extended to a more versatile version (EADPR): To deal with phase wrapping, the original ramp correction including the conversion of image data to the complex plane and back, is applied as a first step. In addition, a two-dimensional polynomial fit with user-defined degree is applied to the image data. The surface that is described by the polynomial is then subtracted from the image. Afterwards, another offset correction based on background regions without sample-coverage is applied in order to settle the image values at the correct level. Experience with various datasets revealed that usually a polynom of degree 2, i.e. of the form

$$p(x,y) = a + bx + cy + dxy + ex^2 + fy^2 + gxy^2 + hx^2y + jx^2y^2, \qquad (3.12)$$

describes the phase distortions sufficiently to gain a flat projection image. Figure 3.6d shows an example of the correction surface formed by a polynomial of degree 2 and Figure 3.6e displays the final projection image. Polynomials of higher degree tend to introduce distortions instead of correcting them.
In the course of extending ADPR, the area that is chosen to determine the ramp or polynomial surface and the concluding offset was defined in a more versatile

way. Originally, the complete image, including every positive and negative edge in the measured phase, was used to define the average two-dimensional gradient. In the extended version, it is possible to use only the empty areas to the left and right of the sample to avoid fitting a distortion that is an actual feature of the sample. The areas are determined automatically by combining a transmission threshold and a visibility threshold, to exclude areas of sample coverage and areas of poor image quality, respectively. In addition, those automatically determined areas are eroded to avoid accidental inclusion of the outer sample edges.

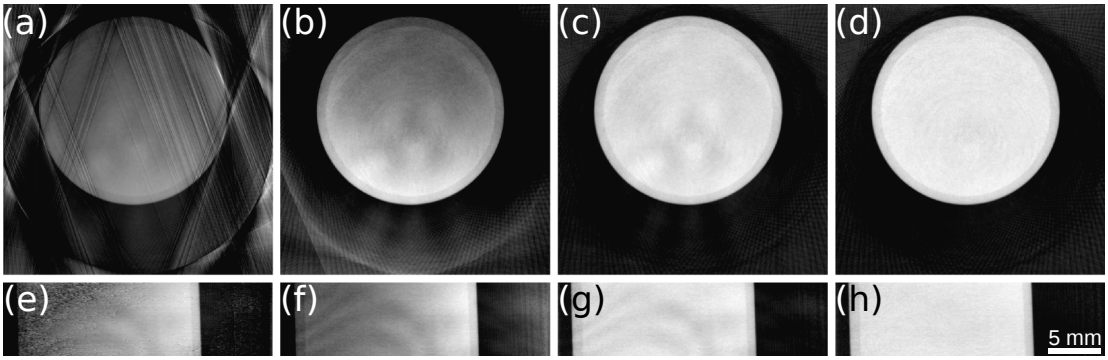

Figure 3.7: Axial (top row) and sagittal (bottom row) reconstructed slices of a phase-contrast tomography scan of a water-filled plastic tube for different cases of phase-recovery correction. (a) and (e) show the reconstruction of completely uncorrected slices. Gradients and projections that contain such strong distortions that phase wrapping occurs over the whole field of view generate strong artifacts in the reconstructed images. (b) and (f) show the reconstruction of projections that were corrected using ADPR. The phase wrapping is eliminated, but a strong gradient and smaller patches and fringes of varying signal remain over the homogeneous sample. (c) and (g) show the reconstruction of projections that were corrected using a polynomial surface fit of degree 2 on top of the ramp correction. The strong gradient is eliminated, but the smaller patches and fringes remain. (d) and (h) show the reconstruction of the polynomial-fit corrected projections that were further processed using the expectation-maximization algorithm introduced in Section 3.3.3.2. Here, also the smaller patches and fringes are eliminated and flat images of the homogeneous sample are regained. All images are scaled from zero to their maximal value.

To evaluate the improvements of the different stages of the extended adaptive differential phase recovery (EADPR) algorithm most clearly and quantitatively, a water-filled plastic tube was chosen intentionally as a very homogeneous sample. It was measured at a source voltage of 30 kVp and a tube current of 466 µA. For each projection angle, 10 phase steps were acquired with 10 s exposure time each. In total, phase stepping sets were recorded for 180 angular positions over the full gantry rotation. 10 flatfields were taken every 20 angles. The detector was operated in 2×2 binning mode. The reconstructed volume covers $707 \times 707 \times 215$ voxels.

The visual effect of the different stages of the EADPR algorithm on a three-

dimensional reconstructed CT dataset is presented in Figure 3.7. A sagittal and an axial slice are shown for each of the stages: When no correction is applied, the slices are dominated by artifacts caused by medium-range phase wrapping (see Figure 3.7a and e). This is the kind caused by strong background distortions as opposed to the phase wrapping caused by strongly phase-shifting sample features. Figure 3.7b and f show the reconstructed dataset corrected with the original ADPR. There is still a strong gradient left due to higher-order distortions in the projection images. This gradient is eliminated by the polynomial surface correction, als shown in Figure 3.7c and g. The remaining smaller patches and fringes can only be eliminated by the more advanced expectation-maximization processing method described in Section 3.3.3.2 (Figure 3.7d and h).
Figure 3.8 displays horizontal and vertical profiles through an axial slice of the dataset in Figure 3.7c in black versus those from the dataset processed equivalently, but with merely a ramp rather than a polynomial surface correction (Figure 3.7b), in blue. The effect of the distortions on the quantitative reconstructed value of the refractive index decrement δ becomes apparent. The blue horizontal profile not only shows a value that is too low overall, but also exhibits a strong cupping that could be falsely attributed to beam hardening. The vertical profile of the insufficiently corrected dataset (blue) drops on one side to a very low value compared to the EADPR-corrected one.

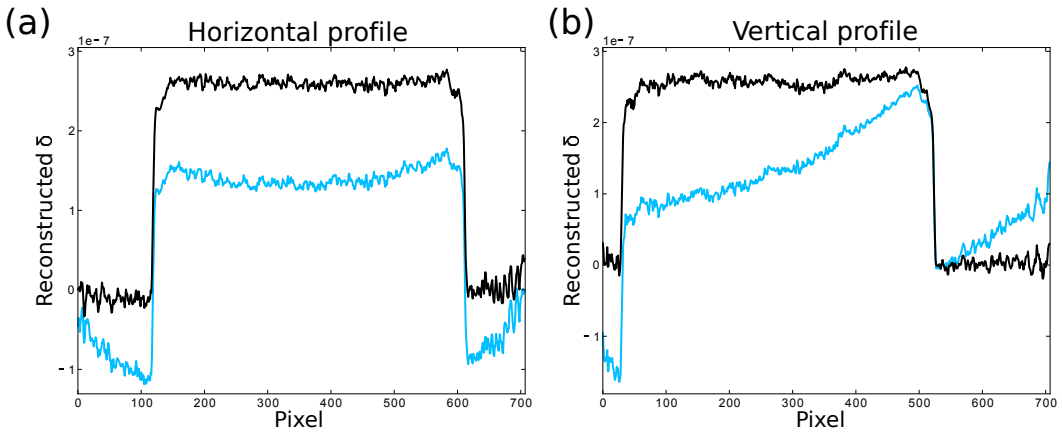

Figure 3.8: Horizontal and vertical profiles through the reconstructed water-filled tube for the polynomial-fit corrected (black) and the ramp-corrected (blue) case. The influence of the correction on the quantitative values is significant. Effects that could be falsely attributed to beam hardening are corrected by the polynomial surface fit correction.

For a rough estimate of the effect of EADPR (and the correction introduced by the EM algorithm) on the extraction of quantitative values, the signal within the water-filled cylinder was averaged through a volume of 140 reconstructed slices for each of the stages shown in Figure 3.7, forming the value δ_w. Also, the value

measured in air δ_a was accordingly averaged in a ring around the plastic tube. From those two values, the datasets were converted to phase Hounsfield Units considering the common definition:

$$\mathrm{HUp} = \frac{\delta - \delta_w}{\delta_w - \delta_a} \cdot 1000. \tag{3.13}$$

Subsequently, the standard deviation in the water volume was calculated in terms of Hounsfield Units deviation and is presented for the four evaluated cases in Table 3.1. The significant reduction of uncertainty introduced by the surface correction from 202 to 41 HUp is apparent. The EM processing reduces the noise even further, however on a smaller scale. Note that the accuracy of quantitative values can be further increased by applying larger statistics during the scan, i.e. more angular positions, more phase steps, longer exposure times. In fact, the present dataset is already undersampled with a reconstructed sample width of approximately 500 pixels and angular sampling of only 180 views. Tapfer (2013) demonstrated the general quantitativeness of high-performance absorption and phase scans at the Skyscan 1190 using a dedicated phantom containing fluids of known chemical constituents.

	no ADPR	ADPR		EADPR	
	SPR	SPR	EM	SPR	EM
σ (HUp)	294	202	190	41	27

Table 3.1: Standard deviation σ in phase Hounsfield units (HUp) for the signal of water in a scan of a water-filled plastic tube, depending on the processing and correction method. EM stands for expectation maximization algorithm, SPR for the standard processing method using a sinusoidal fit (statistical phase retrieval). (E)ADPR: (extended) adaptive differential phase recovery.

Furthermore, the original ADPR could not deliver acceptable image quality for scans recorded with the fast acquisition scheme of a subsequent separate flatfield tomography. Figure 3.9a shows a sinogram of the ramp-corrected projections of a plastic toy (see Figure 3.9e), for which a separate blank tomography scan was acquired after the actual sample scan. The scan parameters are as follows: 40 kVp source voltage, 730 µA source current, 6 phase steps with 5 s exposure time each, 900 angular projections over 360 degrees, 2×2 binning mode. The sinogram shows strong inhomogeneities not induced by the sample. The resulting FBP reconstruction (size 685×685 pixels) in Figure 3.9c again shows a strong gradient. But when the polynomial-surface correction is applied, the resulting histogram is more homogeneous and the FBP reconstruction slice shows no gradient (see Figure 3.9b and d). Hence, the EADPR facilitates CT scans of living mice, where the

animal does not need to be taken out of the beam during a scan for the purpose of flatfield acquisition, if there is enough time to conduct a flatfield tomography afterwards.

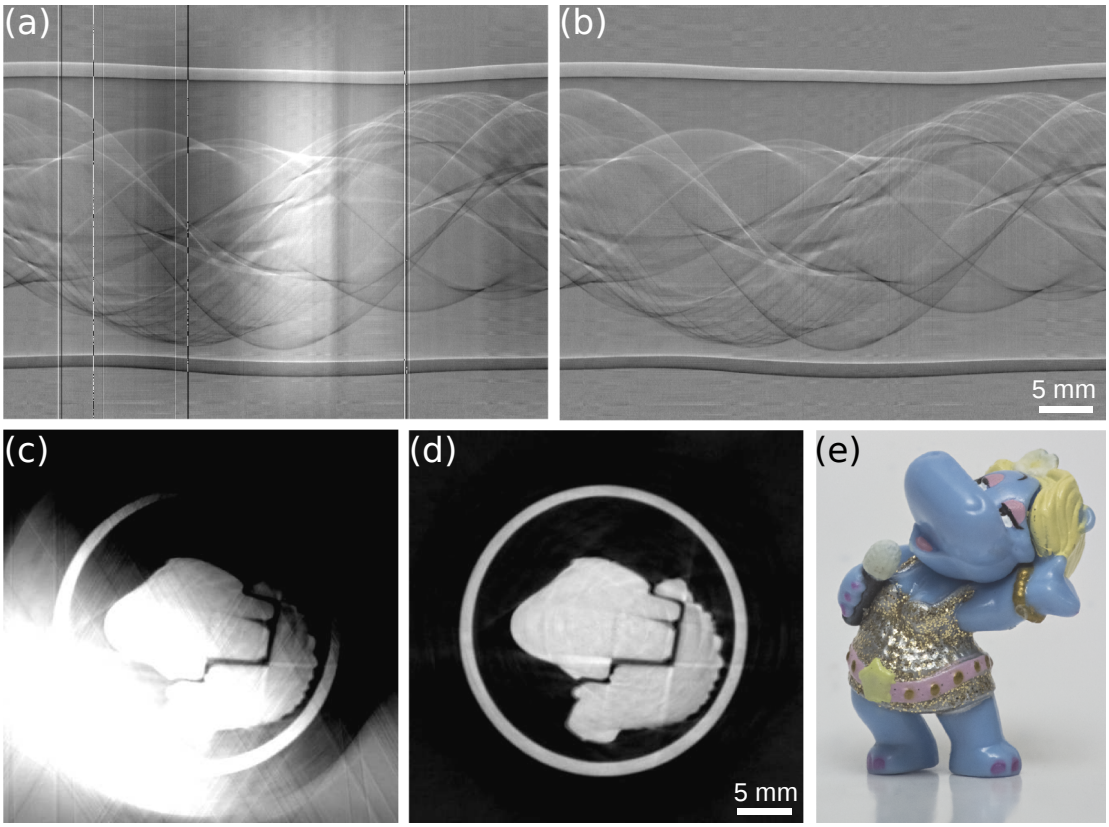

Figure 3.9: Phase-contrast tomography dataset of a plastic toy in a plastic tube, for which the flatfields were recorded in a separate tomography after the actual sample scan. (a) Sinogram of only phase-ramp corrected projections: Many distortions remain. (b) Sinogram of projections with applied 2D polynom-fit correction: The data is considerably more homogeneous. Sinograms are scaled from $-\pi/2$ to $\pi/2$. (c) Tomographic reconstruction of ramp-only corrected dataset. A strong gradient over the volume remains. (d) Tomographic reconstruction of dataset with applied 2D polynom-fit correction. The gradient is removed. Both reconstructions are scaled from zero to the maximal value of the slice shown in (d). (e) Photograph of the plastic sample.

3.3.5 Tomographic reconstruction

3.3.5.1 General framework

To complement the purpose-built processing framework, a tailored tomographic reconstruction software script was developed to allow the use of existing recon-

struction libraries of the research group and become independent of and faster than the commercial 'black-box' reconstruction software 'NRecon'.
Analogous to the processing framework, the reconstruction script is called via command line, providing the path of the processed data in *.hdf* format. All mandatory information is read from a text-based log file created by the processing software, including the geometric distances that are obligatory to deal with the cone-beam geometry of the scanner during reconstruction. The projection operations that are necessary during a tomographic reconstruction are performed by projectors that were developed by Fehringer et al. (2014) and implemented on graphical processing units (GPUs) to accelerate the reconstruction process. In Appendix A.2 the various functionalities that can be chosen by the user are listed.

3.3.5.2 Statistical iterative reconstruction

With FBP, a fast and suitable analytical algorithm is available to reconstruct datasets tomographically that contain little to no noise, are sufficiently sampled (Kak and Slaney, 2001), and do not contain corrupt projections or artifact-inducing features. If those constraints are not fulfilled, emerging iterative reconstruction techniques (introduced in Chapter 2, Section 2.4.5) provide a better alternative. In conventional clinical CT imaging, the introduction of iterative techniques allows to obtain smooth reconstructions from noisy data, which can be turned over into saving patient dose during a scan (Noël et al., 2011, 2013). Since grating-based PCI and DFI using the phase-stepping procedure inherently require a larger dose per projection than a conventional single absorption projection, the necessity to save radiation dose and acquisition time is even more urgent than in available clinical CT imaging.
As explained before, acquisition time is a particularly delicate issue at the Skyscan 1190, since the overall time for a mouse CT is limited by the anesthesia duration of about two hours. Hence, in this chapter, CT results from the Skyscan 1190 are shown, which were reconstructed using the statistical iterative reconstruction (SIR) framework developed by Hahn (2014). The following paragraphs shortly summarize the working principles of the algorithm and are adapted from Hahn (2014), to which the reader is referred for a more thorough description.

The algorithm relies on a feedback loop consisting of frequent projection operations, namely a forward- and a backprojection, which were implemented on GPUs by Fehringer et al. (2014). For this highly-parallelized implementation, the representation of the image volume subsets in form of voxel discretization is optimal, since it allows for separate handling of data as small independent portions. The

implementation of the forward projection is based on a ray that is traced from the detector pixel of interest through the volume back to the source position (Joseph, 1982; Siddon, 1985). During forward projection, the contribution from each voxel that intersects with the ray is considered to update the detector pixel value. Thus, this operation is repeated in a loop over all detector pixels and projection angles, when projecting forward. On the contrary, the backprojection is voxel-driven (Müller et al., 1998): While looping over all voxels for each projection angle, each voxel is projected onto the detector and its value is updated by the linearly interpolated contributions of the respective detector pixels.
In contrast to conventional attenuation-based CT, the input to the SIR framework is not constituted of raw images, but already processed data. Thus, limitations to the spatial resolution posed by the acquisition system such as the PSF (Section 3.3.2), are not accounted for in the reconstruction algorithm, so they need to be dealt with beforehand.

The statistical model that underlies the iterative reconstruction technique is presented for the case of measured differential phase images, i.e. a measured refraction angle α, from which the quantity of the refractive index decrement δ is to be reconstructed. However, the algorithm can, of course, be used to reconstruct the linear attenuation coefficient μ from measured transmission data $\frac{I}{I_0}$ or the linear diffusion coefficient ϵ from measured visibility data $\frac{V^{\mathrm{s}}}{V^{\mathrm{r}}}$. In this case, according to equations from Section 2.4, the negative natural logarithm of the measured data has to be taken first. Additionally, the partial derivative in Equation 3.14 has to be removed, because of the non-differential nature of the data.
The statistical model behind the SIR can be described in three ways: by a weighted-least-squares fit, a maximum-likelihood formulation or a Bayesian statistics approach. Each of those approaches lead to one central cost-function (Hahn, 2014):

$$\hat{\boldsymbol{\delta}} = \arg\min_{\boldsymbol{\delta}} \sum_{x,\theta} w_{x,\theta} \left(\alpha_{x,\theta} - \sum_{j} \partial_x A^{\theta}_{x,j} \delta_j \right)^2 + \sum_{k} \lambda_k R_k(\boldsymbol{\delta}). \tag{3.14}$$

The first term, the sum over pixel index x and the projection view θ, ensures the consistency of the measured refraction angle $\alpha_{x,\theta}$ with the statistically modeled image formation process. The second term, the sum over k, represents a regularization term that is discussed below. The term $\sum_j \partial_x A^{\theta}_{x,j} \delta_j$ describes the forward-projection model in form the entries $A^{\theta}_{x,j}$ of a matrix operation $\mathbf{A}$ acting on assumed δ_j, where the index j describes the number of basis functions underlying the forward projector. The derivative ∂_x stems from the differential nature of the signal in case of differential phase images. The weights $w_{x,\theta}$ are based on

the statistical uncertainty for each pixel in the projection image extracted by the statistical phase retrieval procedure as described in Section 3.3.3.1, so that less reliable pixel values are considered less in the reconstruction process. The weighting can be extended additionally by masking out complete corrupt projections, to exclude their contribution to the reconstructed image.
Since the reconstruction problem is ill-posed, i.e. many assumed δ_i can lead to the correct measured values $\alpha_{x,\theta}$, a regularization term is necessary. Otherwise, the algorithm would converge to local solutions, missing the global optimum. Several approaches exist to regularize the minimization of the cost function. The common ideas are to force the reconstructed values to be smooth and/or to include a-priori knowledge about the sample, for example to incorporate a fixed value where it is to be expected for a known material. Another possibility can be to include information about the noise power spectrum of the signal. For more information on regularization possibilities, the reader is referred to Hahn (2014) and Fessler (2000). By selecting the regularization parameter λ, a trade-off between noise reduction and spatial resolution has to be found. In this thesis, the smoothness-inducing version of the regularization is used.
The SIR results presented in this chapter were regularized using the Huber potential (Huber, 1964):

$$R_H(\mathbf{x}, \mathbf{m}, \gamma) = \sum_i m_i \sum_{j \in \mathcal{N}_i} \begin{cases} \frac{(x_i - x_j)^2}{2\gamma^2} & \text{for } |x_i - x_j| \leq \gamma \\ \frac{|x_i - x_j| - \gamma/2}{\gamma} & \text{for } |x_i - x_j| > \gamma \end{cases}, \tag{3.15}$$

where i indicates all image voxels and j is the index running over all neighboring voxels of voxel i. The Huber potential locally penalizes differences between neighboring voxels. However, by choosing the parameter γ appropriately, large voxel differences are less regularized than small ones. Thereby, true edges will be preserved. By setting a mask m_i the regularization can be restricted to certain voxels.
The minimization of the cost function is carried out by computing its local gradient and subsequently performing a line search along the steepest descent. When reaching the minimum, another line search is done in a conjugate direction. This method is called minimization via conjugate gradient. For this algorithm, the non-linear version was implemented to deal with the non-linear Huber potential.

3.4 *Ex vivo* phase-contrast CT

3.4.1 Introduction

To demonstrate the soft-tissue contrast within inner organs that is achieved by the Skyscan 1190, a high-performance scan of a formalin-fixated *ex vivo* mouse was conducted. In several preceding studies, equivalent fixated mouse samples have been imaged in phase contrast, both at synchrotron facilities (Tapfer et al., 2014) and at a high-performance bench-top setup with a rotating anode x-ray source (Tapfer et al., 2013). Along these lines, the scan presented in this chapter serves as a benchmarking result for soft-tissue discernability at a compact rotating-gantry setup. Processing and reconstruction tools for image quality enhancement are exemplarily shown at this dataset. Moreover, the limits of the phase-contrast signal generated in soft-tissue at this particular setup concerning *in vivo* imaging are assessed by means of an undersampling series of the acquired dataset.

3.4.2 Data acquisition and processing

The formalin-fixated mouse was provided by Prof. Multhoff, Radiotherapy Department, Klinikum rechts der Isar, Technische Universität München, and placed in a plastic cylinder filled with formalin. It was scanned at a source peak voltage of 30 kV and a current of 453 µA. For each angular position, a phase-stepping series of 6 steps with 10 s exposure time each was recorded. Views from a total of 1000 angular positions, evenly spaced over 360 degrees, were acquired. After every 20th angular position, a block of 10 flatfields was recorded. The data was recorded with the higher G2 in place (Section 3.2). The effective angular opening of the coronal slices presented in this section covers $\sim 7.0°$ in horizontal direction $\sim 3.1°$ in vertical direction.
The raw data was processed once without deconvolution of the PSF and once with three iterations of deconvolution with the RL algorithm. The attenuation, dark-field and phase signals were extracted using the statistical processing and the EADPR algorithm. Basic filtered back-projection was performed of the unconvoluted data for attenuation, dark-field and phase signal, with a ring-removal of filter kernel size of 9 pixels (for more details, see Appendix A.2) in case of the attenuation signal, because the grating structures cause strong ring artifacts in the tomographic reconstruction. To compare image quality, in case of the phase signal, a filtered back-projection (FBP) of the deconvolved dataset was performed. Subsequently, a single-band bilateral filter, which decreases image noise while preserving edges (see Allner (2013)), was applied to two exemplary slices. A filter

kernel defined by a three-dimensional Gaussian distribution with a width σ of 3,5,3 pixels was used. The shape of the filter was chosen anisotropic to cope with line artifacts that are perpendicular to the axial direction. In addition, statistical iterative reconstructions with Huber regularization were performed of the deconvolved data, for the fully sampled case of 1000 projections, as well as for the undersampled cases of only 500, 250, 125 and 62 evenly spaced projections. The reconstruction parameters were $\lambda_{\text{Huber}} = 0.5$, $\gamma_{\text{Huber}} = 0.001$, and 50 iterations.[‡] The used angular views were evenly spaced over the full 360 degrees to avoid artifacts induced by the bone that can occur when performing 180 degree scans.

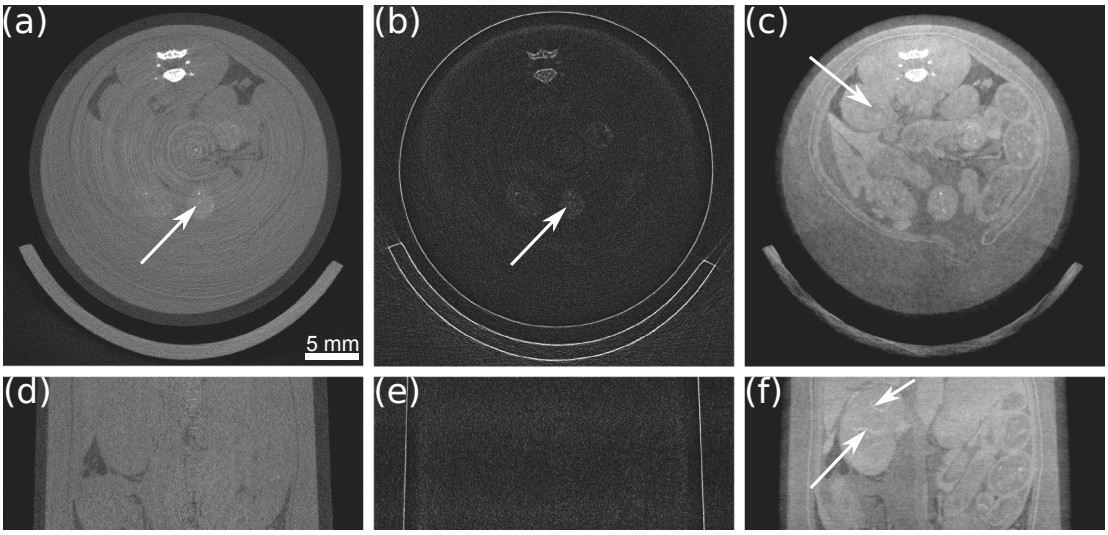

Figure 3.10: High-performance tomography of a fixated *ex vivo* mouse, reconstructed with simple filtered back-projection. The top row shows axial slices (a-c), while the bottom row shows coronal slices (d-f). (a, d) Attenuation contrast. (b, e) Dark-field contrast. (c, f) Phase contrast. The attenuation signal clearly depicts the bones, but shows low soft-tissue contrast. The dark-field image displays scattering in the spine and in remaining fibre-rich food in the intestines. Strong refraction at the edges of the plastic cylinder and mouse bed also cause a visibility decrease that translates into a dark-field signal. The phase-contrast images exhibit strongly increased soft-tissue contrast that allows for discernibility of various organs and even shows inner structure of the kidney. All images were scaled for best visual appearance.

3.4.3 Results and discussion

Figure 3.10 shows the filtered back-projection reconstruction of all three modalities of the fully sampled dataset of the *ex vivo* mouse. The axial (a-c) and coronal

[‡]Those parameters refer to the SIR implementation version of the group-internal pyCT.reco package in operation during the effective date of July 15th, 2014.

(d-f) slices through the abdominal area illustrate the complementarity of the three signals channels. The attenuation-based signal (Fig. 3.10a and d) indicates structures of strong absorption, such as the spine or remaining food in the intestines as indicated by the white arrow. The contrast between organs is non-existent, only some interstitial fluid of lower density can be spotted. The image quality is deteriorated by ring artifacts that arise from the grating structures in the beam path. This is unavoidable in the scanner prototype, because the detector position cannot be shifted relatively to the grating assembly during a scan. Note that, when comparing attenuation-based data to the other signal channels, a state-of-the-art conventional small-animal microCT system without gratings generates images with considerably fewer ring artifacts. In the dark-field tomography images (Fig. 3.10b and e), scattering structures in the animal are highlighted, which are the bones and the fibre-rich food in the intestines (indicated by the white arrow). For dark-field CT, the abdominal area usually does not provide many structures of interest, at least not in a setup with limited sensitivity as with the Skyscan 1190. Strong local changes of the wavefront that are not fully resolved by the detector pixel size appear at edges from plastic to air, i.e. at the sample cylinder and the animal bed. Due to the partial volume effect, this leads to a decrease in visibility and also appears as a dark-field signal (Koehler et al., 2012). The phase-contrast CT (Fig. 3.10c and f) shows enhanced soft-tissue contrast, so that inner organs like kidney, liver and intestines can be readily differentiated from each other. Also, the soft tissue can clearly be distinguished from the fixation fluid. In the kidney, even inner structures of the organ are visible, indicated by white arrows. However, the reconstructed data still shows a considerable amount of phase-contrast–typical low-frequency noise. Moreover, a shadowing artifact from the animal bed towards the rotation center in the axial slice can be observed, most apparent at the right and left tip of the bed. This can most probably be attributed to phase wrapping at the strongly phase-shifting interface between the sample stage and air. Nevertheless, the soft-tissue representation is excellent compared to absorption-based imaging and approaches the image quality of similar specimens recorded at the rotating-anode setup presented by Tapfer (2013).

In the following, several approaches to increase image quality are evaluated for the phase-contrast signal channel, as this is the most interesting of the three channels for representation of inner organs in the abdominal area. As described in Section 3.3.2, the sharpness of the images is affected by a relatively broad system PSF. The effect of the PSF deconvolution on the projection images of this sample was already shown in Figure 3.4. An FBP reconstruction that originates from differential phase projections that were processed from deconvolved raw data of three iterations is presented in Figure 3.11a and d. It is clearly visible that the increase of sharpness is transferred from the projection images to the reconstructed vol-

ume, for example at the skin layers of the mouse or also at the inner structure of the vertebral body. However, the image noise is strongly enhanced, too, compared to the noise in Figure 3.10c and f.
The noise texture of phase-contrast tomographic reconstructions based on FBP with Hilbert filter of differential phase projections is highly anisotropic: In the axial slices, the noise is approximately isotropically distributed and contains a significant low-frequency part. In the coronal and sagittal slices, the noise along the grating-bar direction is dominated by high frequencies and therefore those slices exhibit a highly anisotropic noise texture and line artifacts (strongly visible in Figure 3.10f and Figure 3.11d).[§]

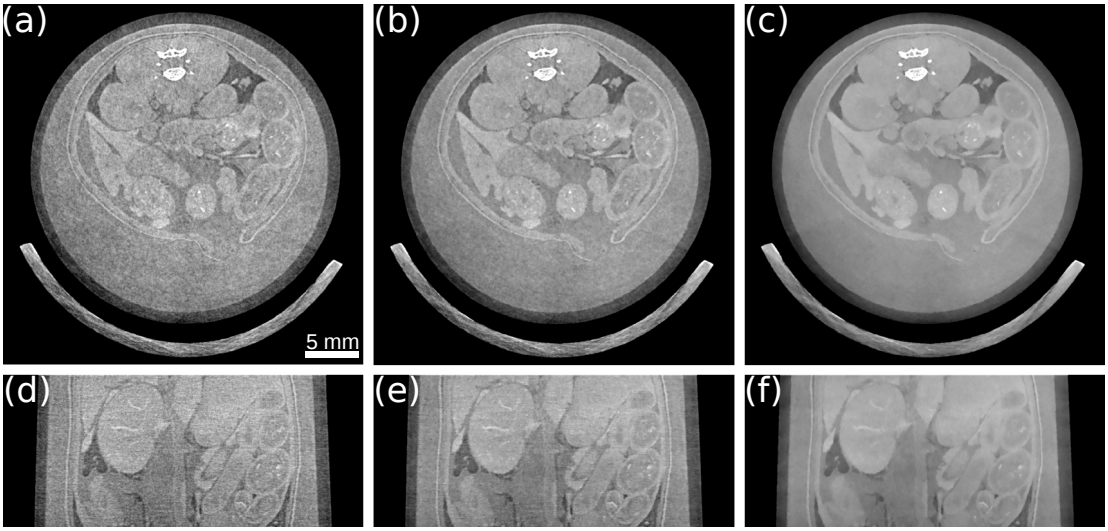

Figure 3.11: Slices of high-performance phase-contrast tomography of a fixated *ex vivo* mouse. The top row shows axial slices (a-c), while the bottom row shows coronal slices (d-f). (a) Filtered back-projection after three iterations of Richardson-Lucy deconvolution with system point-spread function on raw data prior to processing. The deconvolution enhances sharpness, but also increases noise in the images. (b) Filtered back-projection of deconvolved data with subsequent single-band bilateral filtering to counteract the noise increase. (c) Statistical iterative reconstruction of deconvolved data. The regularization suppresses the noise, but preserves the sharp edges. All images are displayed with identical scaling.

To counteract the undesirable effect that the deconvolution increases noise and line artifacts, the slices of the reconstructed volume as displayed in Figure 3.11a and d were treated with a single-band bilateral filter.[¶] This filter applies a value-

[§]An approximated independence of the axial slices is assumed, because of the mild cone angle.

[¶]As another approach, Thüring et al. (2011b) and Schleede (2013) showed that noise can be reduced and line artifacts successfully suppressed by the use of a regularized integration

difference– and distance-depending weighting onto voxels of a certain neighborhood in three dimensions in the reconstructed volume (Allner, 2013). To supress the line artifacts somewhat more than the general noise, the kernel size was chosen to be larger in the direction along the grating bars than perpendicular to it. The filtered slices are shown in Figure 3.11b and e. The successful noise reduction is apparent, while the sharpness is maintained.
To demonstrate a superior way to increase image quality and suppress noise, the deconvolved dataset was reconstructed iteratively with an appropriate regularization parameter, as displayed in Figure 3.11c (axial slice) and f (coronal slice). The noise reduction through regularization is immense, while the edges of the anatomical structures are well preserved. Note that, by deconvolving the raw data with the system PSF, prior to iterative reconstruction, the noise correlation is changed, but the noise model in SIR assumes uncorrelated noise. However, this inaccuracy regarding the model is not pivotal to prevent from the application of the deconvolution, because first an foremost the incorrect noise model is outweighted by the gain in edge sharpness. Furthermore, even without deconvolution, the assumption of uncorrelated noise is violated in the Skyscan 1190 data, because of correlation-inducing factors such as detector blur, source size or cone angle. The ideal solution would be to consider noise-correlation in the iterative reconstruction model as for example done in Tilley et al. (2014).
The displayed *ex vivo* scan represents a high-perfomance image acquisition of the sample. With 1000 angular views the dose is in the range of 1.5 to 2 Gy, which is only acceptable for terminal *in vivo* experiments. As discussed in detail by Raupach and Flohr (2011, 2012), the PCI-CT signal measured with phase stepping is expected to break down earlier than attenuation-based CT when going towards lower dose. On the other hand, PCI-CT profits from high system resolutions. To investigate the sampling limit for the phase-contrast signal breakdown in the Skyscan 1190, the deconvolved dataset was reconstructed several times with stepwise reduced sampling from full sampling over 1/2, 1/4, 1/8 down to 1/16 of the original number of projections.

Figure 3.12 shows axial and coronal slices of the undersampling series reconstructed with simple filtered back-projection. With 1/2 of the projections, the noise level increases visibly, but all structures are still recognizable (Fig. 3.12b and e). Already with an undersampling factor of 1/4, which corresponds to 250 projections, the noise dominates over some of the internal structures (Fig. 3.12c). The visibility of the vessel structure in the kidney in the coronal slice (Fig. 3.12f) is significantly decreased. With stronger undersampling, the inner organs are hardly visible anymore and with only 62 projections the signal breaks down under noise influence (Fig. 3.12g-j).

algorithm on the differential phase projections prior to reconstruction.

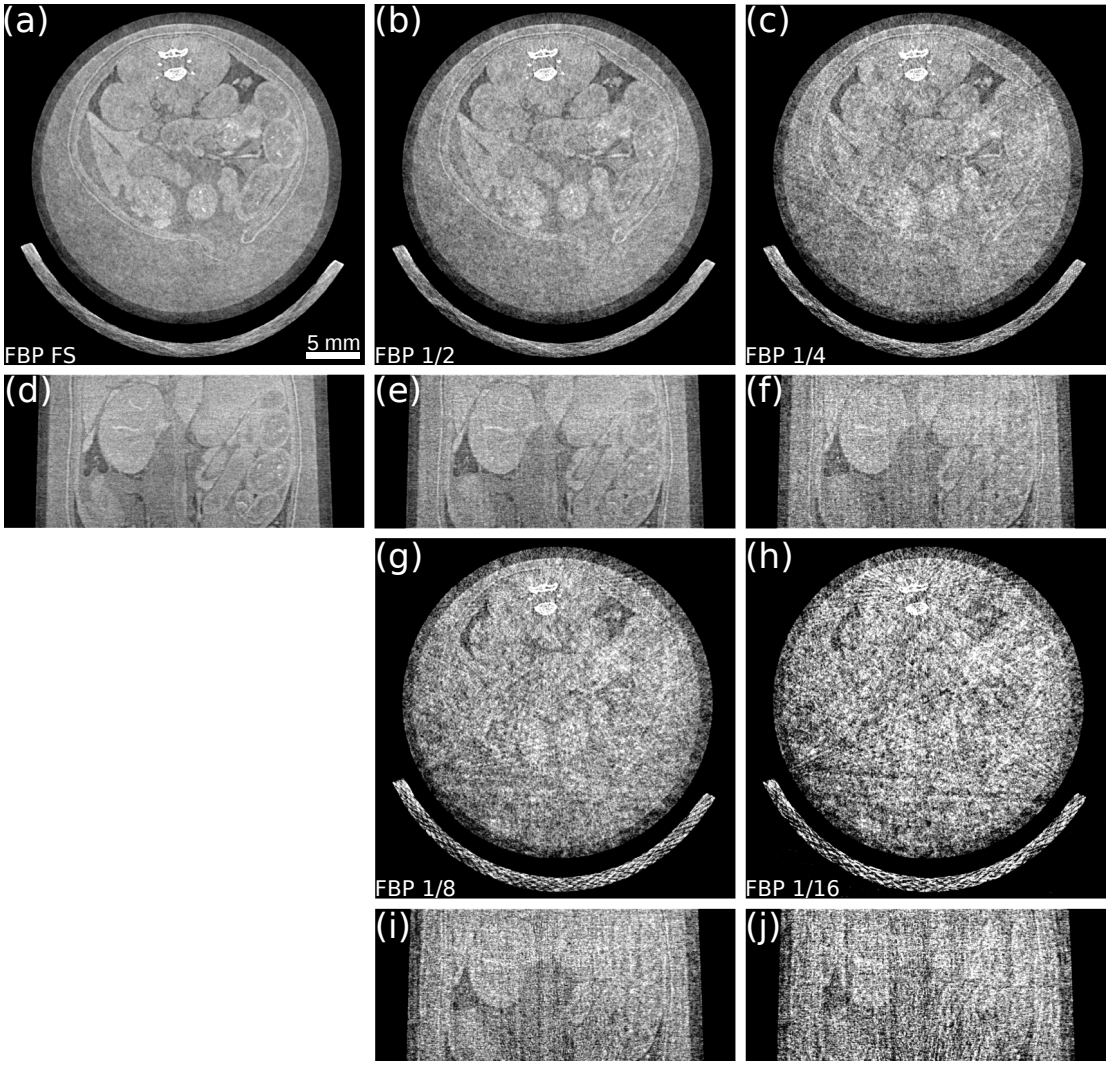

Figure 3.12: Tomography of a fixated *ex vivo* mouse, reconstructed with simple filtered back-projection for decreasing numbers of projection angles. The first and third row show axial slices (a-c, g, h), while the second and forth row show coronal slices (d-f, i, j). (a, d) FBP of the fully sampled (FS) data set with 1000 projections. (b, e) FBP of 1/2 of the measured projections. (c, f) FBP of 1/4 of the acquired projections. (g, i) FBP of 1/8 of the acquired projections. (h, j) FBP of 1/16 of the acquired projections. It is apparent that already with an undersampling factor of 1/4 the noise dominates over the weaker phase-shifting internal structures of the animal.

Figure 3.13 shows axial and coronal slices of the undersampling series reconstructed with SIR. When compared to the FBP undersampling series discussed before, it is striking that the regularization in the SIR handles the noise arising from dose reduction in a superior manner. With only half of the projections, the

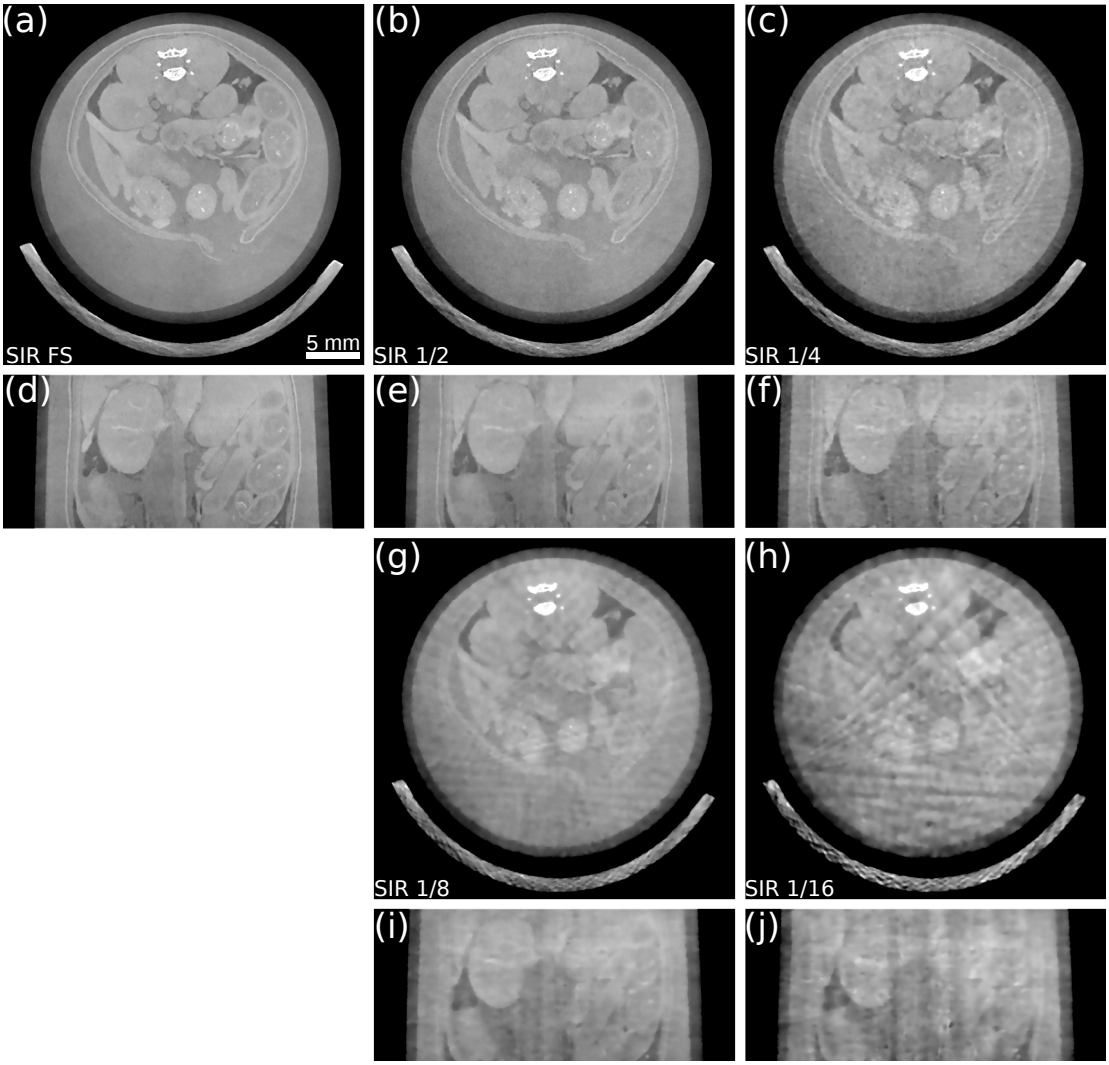

Figure 3.13: Tomography of a fixated *ex vivo* mouse, reconstructed with statistical iterative reconstruction for decreasing numbers of projection angles. The first and third row show axial slices (a-c, g, h), while the second and forth row show coronal slices (d-f, i, j). (a, d) SIR of the fully sampled (FS) data set with 1000 projections. (b, e) SIR of 1/2 of the measured projections. (c, f) SIR of 1/4 of the acquired projections. (g, i) SIR of 1/8 of the acquired projections. (h, j) SIR of 1/16 of the acquired projections. With an undersampling factor of 1/4 the weaker phase-shifting inner organs can still be distinguished despite streak artifacts. Even with only 1/8 of the projections, most internal structures are recognizable, however strongly blurred.

image quality is only slightly deteriorated, and weak streak artifacts arise in the axial slice (Figure 3.13b). With an undersampling of 1/4 (Figure 3.13c), stronger streak artifacts occur, but also the weakly phase-shifting organs can still be distinguished. Even with only one eighth of the projections, most inner organs are

recognizable, however a strong blurring is visible (Figure 3.13g, i). With an undersampling factor of 1/16, the streaks dominate and structure visibility is not given anymore.
From the presented results, it is apparent that — by using SIR with an appropriate regularization — the undersampling limit for a certain feature visibility can be pushed towards fewer angular views. The regularization smoothes noise in general, so in principle one can also choose the way of recording angular views with shorter exposure instead of acquiring fewer angular views. However, the approach of shorter exposure per view becomes unfavorable at some point, as each raw projection in the Skyscan 1190 requires a certain amount of overhead time and is afflicted with electronic readout noise. A detailed analysis of the signal-to-noise ratio depending on varying acquisition schemes at the Skyscan 1190 (without analysing the influence of the reconstruction technique) can be found in Müller (2013).[‖]
The limit of phase-contrast signal breakdown (about 250 projections with 6 steps and 10 seconds exposure time each) still prevents *in vivo* PCI-CT for the structures that do not exhibit a strong phase shift, such as the inner organs of the abdomen, mainly because the duration of the acquisition exceeds the possible duration of anaesthesia at the current setup. The approximate dose of ≤ 500 mGy would be compatible with *in vivo* mouse scans. Nonethless, tissue types with strongly differing electron densities, such as lung tissue versus solid soft tissue, can be visualized *in vivo* by PCI-CT at the Skyscan 1190. However, Section 3.6 will show that for this application, the dark-field channel provides more accessible information than phase-contrast imaging. In Section 3.7, possible alterations to the scanner setup are discussed to push the signal breakdown limit and allow *in vivo* PCI-CT of the abdominal area.

3.5 *In vivo* projection imaging of a healthy mouse

Note that parts of data and content of this section have been published previously and can be found in Bech et al., "In-vivo dark-field and phase-contrast x-ray imaging", Scientific Reports (2013).

3.5.1 Introduction

The results from the Skyscan 1190 that were presented so far covered phantom as well as *ex vivo* measurements. The main purpose of the development of this

[‖]For a general discussion of noise in GBI the reader is referred to Chabior (2011).

scanner was, however, to take the leap to imaging of living animals. This represents an important milestone in the translation of phase-contrast and dark-field imaging into a clinical environment. Moreover, *in vivo* imaging is a mandatory prerequisite for the identification of diseases, for which the new technology can deliver diagnostic benefit. This is particularly important for organs such as the airways that can – under certain circumstances – exhibit a significantly different signal when excised and fixated compared to the *in vivo* situation, caused by differing encased air volumes.
Other *in vivo* studies using PCI/DFI techniques were so far restricted to synchrotron radiation sources (Parsons et al., 2008; Siu et al., 2008; Coan et al., 2010; Tang et al., 2011; Takeda et al., 2012) and/or a very small field of view (Bennett et al., 2010). The Skyscan 1190 is the only scanner solely dedicated to small-animal imaging with appropriate monitoring devices, a fixed animal bed in horizontal position around which the setup can be rotated, and a heating facility to keep the body temperature of the animal stable.
When translating to *in vivo* imaging, we concentrated first on mere projection imaging to avoid the stability and time restrictions described earlier. However, in Section 3.6, also the first *in vivo* CTs are presented.

3.5.2 Data acquisition and processing

The animal experiment was performed according to the study protocol approved by the ethics committee for animal studies of the University of Antwerp. The first *in vivo* phase-contrast and dark-field projection imaging was performed at the Skyscan 1190 prototype scanner located at *Bruker microCT*, Kontich, Belgium, which has identical specifications concerning the complete setup as the scanner in the laboratory at the Technische Universität München. For G2, the smaller gold structure with a height of 25 µm was used. The mouse was anesthetized using an intraperitoneal injection of Sodium pentobarbital (Nembutal) at a dose of 30-50 mg/kg. It was fixed in a supine position on the animal bed of the scanner by the use of plastic tape to minimize movement artifacts. The animal was monitored via a live video system for vital functions during the whole scan. The x-ray source was operated at 31 kV peak voltage and approximately 500 µA current. A phase stepping series of 5 images with an exposure time of 10 seconds each was acquired, resulting in a total dose of 3.9 mGy to the animal per phase stepping set. The dose had been determined via a measurement by A. Yaroshenko using a patient skin dosimeter (Unfors PSD, Unfors Instruments AB, Billdal, Sweden) placed in the center of a polymer cylinder with a diameter of 3 cm as an appropriate mouse phantom. Dose rates corresponding to certain peak voltages are listed in Table 3.2. The animal was imaged alive in two conditions, once in its natural furry

state, and once after depilation in the chest region, to be able to evaulate the influence of fur to the three imaging signals. Afterwards the mouse was sacrificed and imaged again *ex vivo*.

Peak voltage [kVp]	Dose rate [mGy/s]
26	0.014
27	0.021
28	0.027
35	0.057
38	0.109
42	0.203
47	0.276

Table 3.2: Dose rates for different peak voltages (at maximum power) of the x-ray source of the Skyscan 1190. Data courtesy A. Yaroshenko.

The three imaging signals were obtained by using the EM algorithm and EADPR to remove remaining fringes and distortions. Two height steps of the furry *in vivo* scan were stitched together for a better overview over the signal-generating structures in the animal. For comparison of the image content provided by attenuation and differential phase signal, a differential attenuation image was generated from the attenuation data by computing the gray value difference between neighboring pixels along the horizontal axis.

3.5.3 Results and discussion

Figure 3.14 shows the stitched images of the living mouse with fur for conventional attenuation (a), dark-field (b), and differential phase (d) signal. In the attenuation image, mainly the skeletal structure of the mouse is visible. In contrast, the differential phase signal shows strong refraction of the x-rays at the edges of air-filled structures such as bubbles in the intestines and the trachea. To allow an evaluation of the difference in information content in the attenuation versus the differential phase signal, a differentiated version of the attenuation signal is shown in Fig. 3.14c. It highlights that the strongest influence to the signal is due to increased absorption in the calcium-rich bone structures, whereas in the differential phase signal, the soft-tissue and air structures dominate. This observation suggests a strong potential of phase-sensitive x-ray imaging for diagnostics of airway diseases.

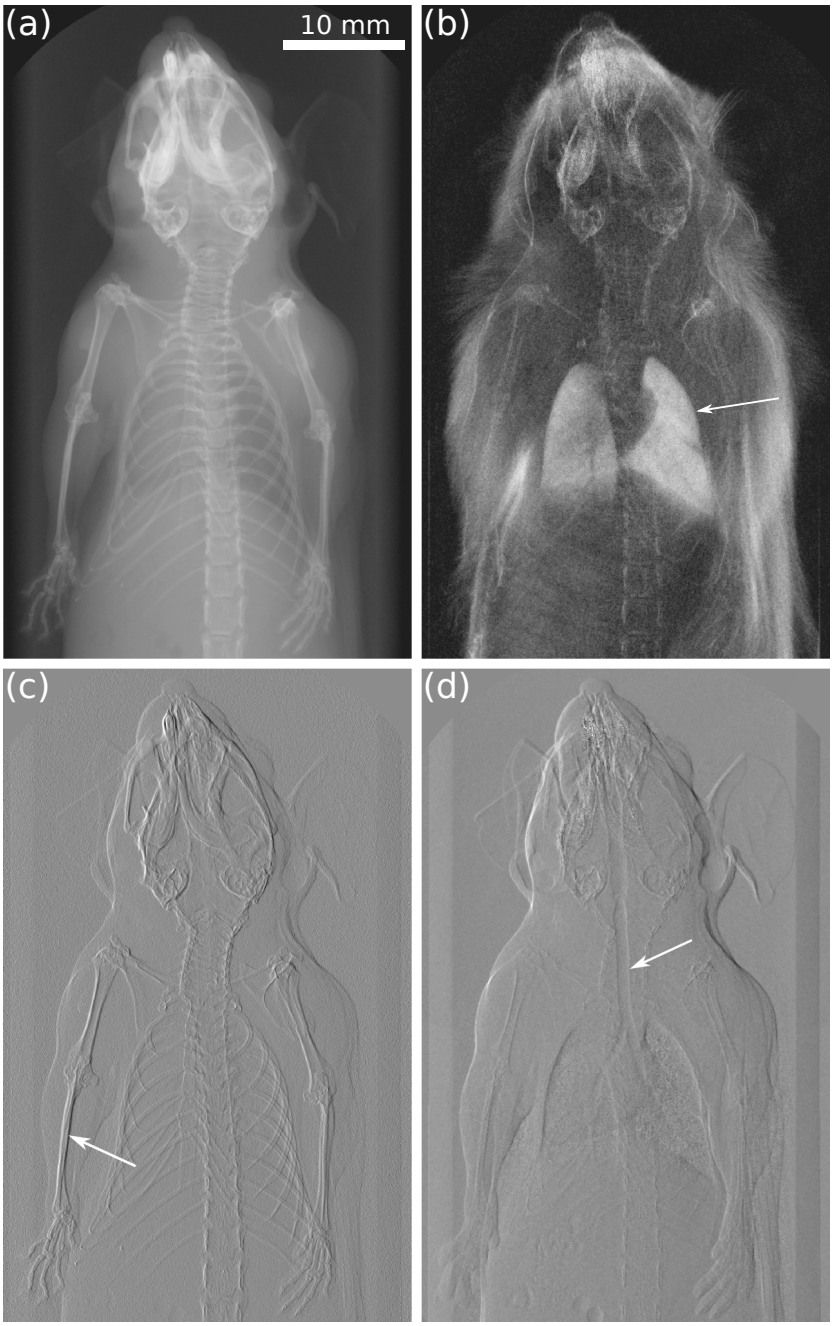

Figure 3.14: *In vivo* projection images of a healthy mouse. (a) Attenuation [0, 1]. (b) Dark field [0, 1]. (c) Differential attenuation (scaled for a similar dynamic range as covered by the differential phase). (d) Differential phase $[-\pi/2, \pi/2]$. As indicated by arrows, the airways show up strongly in dark field (lung) and differential phase (trachea), whereas the attenuation signal mainly provides depiction of boney structures.

The dark-field projection (Fig. 3.14b) shows strong scattering of x-rays at fur, but more importantly in pulmonary tissue. The lung comprises a network of air-filled tissue bubbles in the range of tens of micrometers, the alveoli, which serve for gas exchange in the blood. Those numerous tissue-air interfaces exhibit strong scattering of x-rays, resulting in an enhanced dark-field signal.

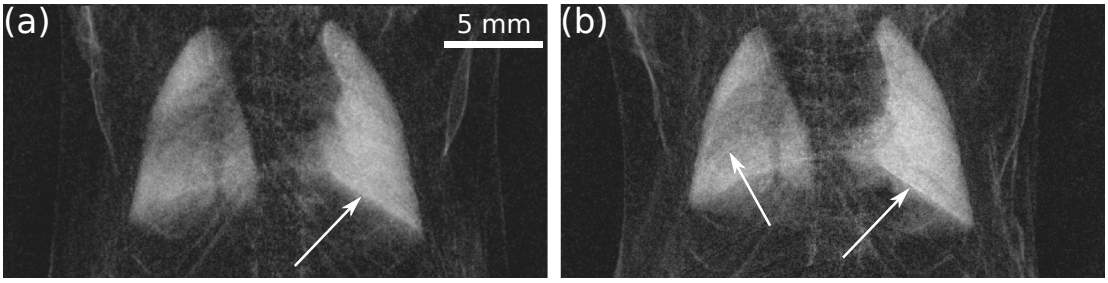

Figure 3.15: Dark-field projection images of the thorax region of (a) depilated *in vivo* mouse and (b) the same mouse *post mortem*. The images serve to visualize the extent of artifacts due to breathing motion. White arrows indicate edges at the diaphragm and at the ribcage that appear clearer in the motion-free *post mortem* state and are slightly blurred in the *in vivo* image. Images are scaled from 0 (no scattering) to 1.0 (strong scattering).

Figure 3.15a displays a dark-field image of the same mouse after the hair in the chest region was removed. Therefore, the background scattering generated by hair-to-air interfaces is eliminated. The same image was acquired *post mortem* of the same mouse, which is presented in Figure 3.15b. As one step in the stepping series was acquired with 10 seconds exposure time, it covers several breathing cycles of the mouse in the *in vivo* case. In a careful comparison, the extent of motion blurring to the lung signal is visible. In the *in vivo* image, the edges of the lung are slightly blurred, for example at the diaphragm as indicated by a white arrow in Fig. 3.15a. Moreover, in the *post mortem* image, the ribs show up as fine lines on top of the pulmonary tissue, as indicated by the left white arrow in Fig. 3.15b, which is to a great extent blurred out in the motion-affected image. However, the influence of motion is not too severe, so that the images acquired *in vivo* still have diagnostic quality.
To mimimize motion blurring, forced breathing in combination with shorter exposure times would be mandatory to allow for a gated phase-stepping acquisition, such that each step is acquired at identical points in succeeding breathing cycles. However, two shortcomings of the scanner prevent gated phase-stepping so far: First, the forced breathing is best performed in combination with the application of gas anesthesia, which requires a tubing system that can direct the anesthetic gas to the mouse and the exhaled gas out of the scanner again. Due to spatial restrictions, this system is not installed in the current prototype version. Second,

minimizing the exposure time to a range that covers only a small part of a breathing cycle is prevented by too low sensitivity of the detector or too little flux at the x-ray energy, where visibility is optimal for phase- and dark-field imaging. A more sensitive detector and gratings with thinner wafers would shorten the required exposure time. The same measures could also decrease the required dose while maintaining image quality. However, the dose of 3.9 mGy per image set is perfectly acceptable for *in vivo* murine imaging.
The excellent signal strength generated by the lung in the dark field suggests strong potential for the use of x-ray scatter-based imaging in the diagnostics of pulmonary diseases. Schleede et al. (2012) and Yaroshenko et al. (2013) already demonstrated the additional diagnostic value of dark-field projection imaging for the detection of pulmonary emphysema on excised murine lungs, both at a compact synchrotron source with radiation of high brilliance as well as at the prototype small-animal scanner. Following the projection imaging results presented in this section, an *in vivo* study series on various lung disorders, such as emphysema and fibrosis, based on dark-field projections acquired at the Skyscan 1190 was initiated. Research is ongoing, but first very promising results are presented in Meinel et al. (2014b) and Hellbach et al..

3.6 *In vivo* dark-field CT of mice with pulmonary disease

Note that the content of this section has been submitted for publication as Velroyen et al., "X-Ray Dark-Field Computed Tomography of Living Mice". Figures and text passages in this section may appear identically in the publication.

3.6.1 Introduction

Lung diseases pose one of the leading causes of death worldwide (World Health Organization, 2011 (accessed July 18, 2014)). A large fraction of those mortality numbers is represented by chronic obstructive pulmonary disease (Zvezdin et al., 2009), of which lung emphysema is a common component. The disease is associated with inflammatory processes in lung tissue caused most commonly by smoking. In consequence, the alveolar walls necessary for gas exchange in the blood are destroyed, resulting in enlarged distal air spaces and consequently deteriorated lung function and decreased quality of life (Ley-Zaporozhan et al., 2008).

Pulmonary fibrosis can be idiopathic or caused by inhalation of pollutants, infection, or adverse reactions to drugs (Bourke, 2006). In the course of this interstitial lung disease, normal parenchyma is gradually replaced by connective tissue (scarring), resulting in a restricted lung and impaired gas exchange (King, 2005). The sensitivity and specificity of conventional x-ray projection radiography in diagnosing those disorders is low for mild to moderate stages (King, 2005; Washko, 2010), and lung function testing is still gold standard, while direct assessment of the microstructural changes and disease progression is only available via invasive biopsy. Attenuation-based high-resolution computed tomography (HRCT) serves for improved emphysema and fibrosis imaging, also providing information about the three-dimensional regional distribution of the disease necessary for lung volume reduction surgery (Washko et al., 2008; Criner and Mamary, 2010). However, its use is limited due to the required substantial radiation dose (Washko, 2010). In this section, the first successful x-ray dark-field (DF) computed tomography (CT) scans of *in vivo* mice with the dedicated micro-CT scanner Skyscan 1190 (Tapfer et al., 2012) are presented. To exploit the DF signals ability to depict microstructures that are smaller than the imaging system's resolution, thoracic tomographies were acquired of a healthy control mouse, a mouse with pulmonary emphysema and a mouse with pulmonary fibrosis. The scope of this section is to highlight the feasibility and demonstrate the potential diagnostic benefit of the novel contrast modality in three-dimensional imaging. Complementary to the quantitative Hounsfield scale in absorption-based CT, a scatter-based Hounsfield scale for quantitative DFCT of lung tissue is introduced.

3.6.2 Materials and methods

Murine model: Animal experiments were performed with the permission of the responsible Institutional Animal Care and Use Committee according to national (GV-SOLAS) and international (FELASA) animal welfare guidelines. For this study 6 to 8 week old pathogen-free female C57BL/6N mice (Charles River Laboratories, Sulzfeld, Germany) were used. Pulmonary emphysema was introduced by orotracheal application of a solution of pancreatic elastase (80 U** per kg bodyweight) in sterile phosphate-buffered saline (PBS). Pulmonary fibrosis was provoked by orotracheal insertion of 2.5 U bleomycin per kg bodyweight. The control animal was treated with PBS only. Treatments were performed under anesthesia by intraperitonal injection of medetomidine (500 µg/kg), midazolam

**The enzyme unit U is defined as the amount of the enzyme that produces a certain amount of enzymatic activity, i.e. the amount that catalyzes the conversion of 1 micro mole of substrate per minute.

(5 mg/kg) and fentanyl (50 µg/kg). Control and emphysema mouse were scanned 21 days, fibrosis mouse 14 days after insertion.
Scanner setup: The images were acquired using the dedicated small-animal x-ray dark-field and phase-contrast CT scanner Skyscan 1190 (for details, see Section 3.2). The analyzer grating G2 with deeper grating structures (45 µm) was used.
Acquisition: The mice were anesthetized as during emphysema/fibrosis introduction (see *Murine model*) and placed on the sample bed in supine position. During acquisition they were breathing freely. Body temperature and respiratory movement were constantly monitored and the temperature was kept stable via a built-in warm-air fan. All scans were acquired at a source voltage of 35 kVp and a current of 524 µA. The detector was operated in 2-by-2 binning mode, resulting in an effective pixel size of 58 µm. For each angular gantry position, a phase-stepping set of five images was recorded, applying an exposure of 5 s per image. For each animal, 139 angular views distributed over 360° were taken, resulting in a total exposure time of approximately one hour and an accumulated dose of 200 mGy. For processing of the raw phase stepping data, reference sets of phase steps were acquired each time when the scan had progressed ten angular gantry positions. For these images, the mice were temporarily moved out of the beam path.
Raw data processing: The raw stepping images were sharpened using Richardson-Lucy deconvolution with the measured PSF of the imaging system. Since the three modalities have differing noise behaviors (Chabior, 2011; Raupach and Flohr, 2011, 2012), the number of deconvolution iterations was optimized for each imaging channel individually, resulting in one iteration for attenuation, zero iterations for dark field, and three iterations for differential phase images. To extract attenuation, differential phase and dark-field signal from the phase-stepping sets, a pixel-wise statistical phase-retrieval via a sinusoidal fit as described in Section 3.3.3.1 was carried out, to additionally obtain the variances of the signals. To counteract distortions in the phase image caused by thermal and mechanical influences on the grating structures, EADPR (see Section 3.3.4) was applied. Transmission and dark-field images were corrected for variations in intensity by a simple background normalization using areas with no sample coverage. Since all three imaging channels are extracted from the same raw stepping set, the modalities are inherently perfectly co-registered.
Tomographic reconstruction: As the mice cover approximately 675 pixels in width of the field of view, the scans are severely undersampled due to time constraints posed by the anesthesia duration. To partly cope with the resulting artifacts in the tomographic reconstruction, the statistical iterative reconstruction technique, described in detail by Hahn (2014) and briefly in Section 3.3.5, was applied with 10 iterations and parameters optimized for each modality individually but consistent between the datasets of the three mice: attenuation $\lambda_{\text{Huber}} = 0.01$, $\gamma_{\text{Huber}} = 0.0001$,

dark field $\lambda_{\text{Huber}} = 1.0$, $\gamma_{\text{Huber}} = 0.1$, phase $\lambda_{\text{Huber}} = 0.01$, $\gamma_{\text{Huber}} = 0.1$.[††] To counteract over-regularization and loss of detail in case of the attenuation CT, the noise power spectra of the three mice datasets were adjusted by weighting iterative reconstruction and conventional filtered back-projection reconstruction (with Ram-Lak filter) with 0.75 and 0.25 respectively.

Post-processing: For representation and analysis purposes, simple semi-automated threshold-based segmentation was applied to differentiate mouse torso, skeleton, lung, and surrounding air/animal bed by use of the commercially available Software VGStudioMax 2.0 (VolumeGraphics, Heidelberg, Germany). In doing so, only minor manual corrections were necessary. The segmentation of the mouse torso from surrounding structures was performed on the phase-contrast dataset, because it contained the fewest artifacts influencing the outer shape of the mouse. Segmentation of the bones and the lungs was performed based on the attenuation data and the dark-field data respectively, exploiting their modality-inherent strongest signal differences to the surrounding tissue. The perfect co-registration allows for simple transfer of a segmentation in one modality to the volumes of the other modalities. The volume/surface rendering for the three-dimensional representations (Fig. 3.19) and the movie (Screenshots provided in Fig. 3.20) of the datasets was performed by VolumeGraphics based on the aforementioned segmentations. The fusion images shown in Figure 3.18 were created from the isolated torsos in attenuation (gray) and dark field (hot color scheme) using the image fusion tool of OsiriX Imaging Software v.3.7.1 64-bit (by Antoine Rosset) with the setting of 50 % fusion and a manual windowing for best visual appearance.

Histogram analysis: To obtain a voxel set that objectively fully contains the lung for comparison of the dark-field CT gray-value distributions between the mice, the threshold-based segmentations (optimized for visual appearance) were strongly dilated, so that a volume that comprises lung and partly surrounding non-scattering soft tissue was achieved. Apart from lung tissue, only the granular structure of bones can be a possible source of scattering in this region, so the rib cage was subtracted from this volume. The histograms shown in Figure 3.21 represent the gray-value distribution of the remaining volumes. Since the signal extraction, tomographic reconstruction and post-processing was equal for each mouse dataset, the distributions can be assumed quantitatively comparable among each other. A peak-finder algorithm was applied to a multi-Gauss fit of the histogram curves to determine the positions of the zero-scatter peaks of all three mice and the lung peaks of control and emphysematous mouse without influence of local extrema. Subsequently, the gray values (TIFF range) were rescaled to scatter Hounsfield Units (HUs) (see Section 3.6.3 for definition) by setting the mean of the three

[††]Those parameters refer to the SVN checkout of D. Hahn's SIR dpyc package from the effective date of July 26th, 2013.

zero-scatter peak positions to 0 HUs and the location of the lung peak of the control mouse to 1000 HUs.
Histology: After excision, the lungs were fixated in paraformaldehyde for conservation during transport. They were subsequently washed to remove the formalin solution and then decalcified in a 10 % EDTA solution for 5 days. The samples were dehydrated and embedded in paraffin. In the coronal plane, multiple 10 µm thin slices were prepared at an interval of 0.5 mm. After deparaffinization and hydration the slices were stained using Mayers hematoxylin and eosin (HE). Ultimately, they were dehydrated and scanned.

3.6.3 Results and discussion

Figure 3.16 provides an overview over the CT datasets of this study comprising three *in vivo* cases imaged in conventional attenuation, dark field and phase contrast. The correspondent histological slices to illustrate the nature of the respective disease are provided in Figure 3.17. Comparing the conventional CT scan of the emphysematous mouse (Fig. 3.16b, e) with the control (Fig. 3.16a, d), one observes only subtle differences towards darker gray values in peripheral lung tissue in the emphysematous case. The resolution of the imaging system does not allow a direct depiction of the alveolar wall structure. In the respective CT slices of the DF channel (Fig. 3.16g, j for control, h, k for emphysema) the strong difference in signal allows for striking discernibility between control and diseased case. The destruction of alveolar walls and resulting enlargement of air spaces (as displayed in the corresponding histological section in Fig. 3.17b) causes significantly reduced x-ray scattering, while the overall loss of tissue and the resulting attenuation decrease is weak.
In the case of lung fibrosis (Fig. 3.16c, f for attenuation, i, l for DF) the replacement of functional alveolar network by solid scar tissue is clearly apparent in both modalities, since the presented case is at an advanced stage. The DF image reveals areas with remaining functional alveolar structure. Histology illustrates the scarring in the lung (Fig. 3.17c), compared to healthy lung tissue (Fig. 3.17a).
The phase-contrast CT (Fig. 3.16m-r) images provide similar information as the attenuation-based CT images.

Figure 3.18 shows a volumetric overview of the fusion of the attenuation CT and DFCT for the two pathological cases emphysema (a-f) and fibrosis (g-l). The fused representation, which is easily possible due to the perfect co-registration inherent to the method, provides a simultaneous impression of anatomy, depicted by the attenuation CT, and functionality, indirectly displayed by DFCT, since alveolar structure can be related to quality of gas exchange (Haraguchi et al.,

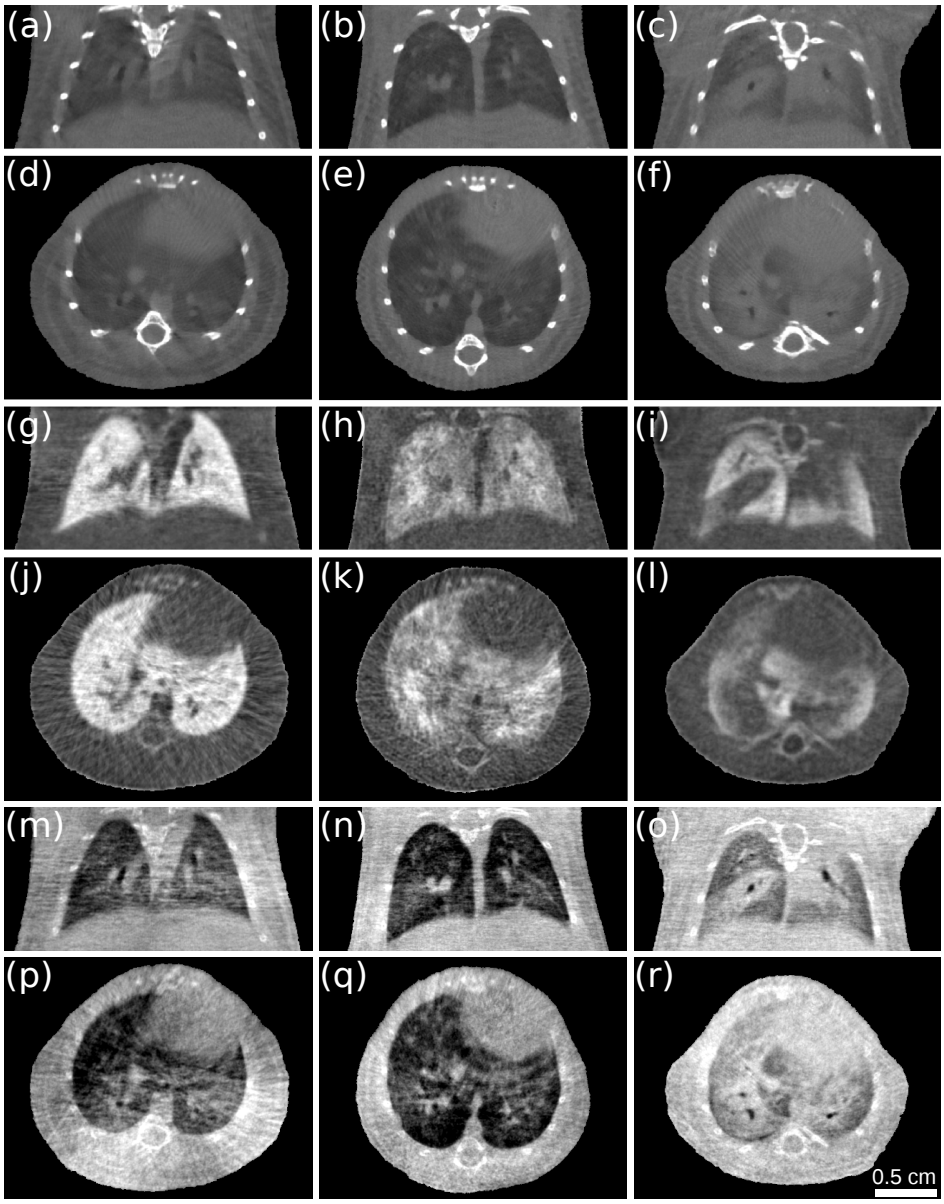

Figure 3.16: Exemplary attenuation, dark-field and phase-contrast CT slices of lungs of three in vivo mice. Pathophysiological changes are subtle in the attenuation-based, but striking in scatter-based CT images. In this particular case, the phase-contrast images provide similar information as the attenuation contrast images. Gray-value windows are chosen for best visual appearance, but consistent within the same modality, respectively. Left column: Control mouse. Center column: Emphysematous mouse. Right column: Fibrotic mouse. (a)-(c): Coronal slices of attenuation CT. (d)-(f): Axial slices of attenuation CT. (g)-(i): Coronal slices of dark-field CT. (j)-(l): Axial slices of dark-field CT. (m)-(o): Coronal slices of phase-contrast CT. (p)-(r): Axial slices of phase-contrast CT.

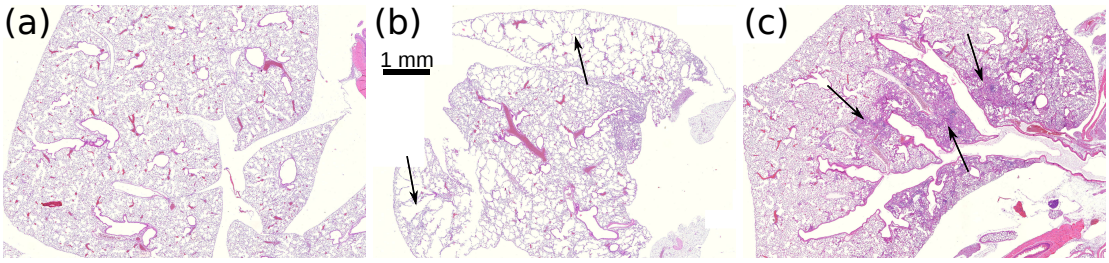

Figure 3.17: Histopathological slices (HE-stained) of the measured murine lungs. (a) Healthy lung: The alveolar structure is intact. (b) Emphysematous lung: Alveolar walls are destroyed and air spaces are enlarged. (c) Fibrotic lung: The lung exhibits scar tissue of higher density than healthy pulmonary tissue.

1998). Similar to the function-anatomy combination in well-known multi-modal datasets like PET-CT (PET: positron emission tomography), the conventional attenuation CT images in gray shades were overlaid by DF data in PET-typical hot color scheme. Note, however, that contrary to PET, where hot areas indicate accumulation of tracer and therefore generally diseased tissue, in the displayed fusion images, the brighter color codes the stronger scattering, corresponding to the more intact or healthier lung tissue. The combined representation allows for a comprehensive depiction of the three-dimensional distribution of the diseases over the lung volume in the anatomical frame. In the case of emphysema, Figure 3.18 shows that destruction of alveolar structures and size increase of air voids predominantly appears in peripheral regions of the lung as indicated by white arrows. On the contrary, in Fig. 3.18g-l, arrows illustrate that the proliferation of the induced fibrosis concentrates on the central, peribronchial areas. Regarding the inherent complementarity of the two signals, note that in DF large air-filled voids such as the bronchi are coded identically to solid soft tissue, whereas they are distinguishable in attenuation data.

For a better three-dimensional impression, Figure 3.19 provides exemplary views of volume renderings of the acquired datasets. Bones were segmented from the attenuation signal, whereas lung tissue was extracted from the DFCTs and represented by a semi-transparent hot color map to enhance inter- and intra-pulmonary structural variations. The 3D views confirm the earlier findings from the 2D slices: The control lung exhibits a strong homogeneous scattering pattern all over its volume, whereas the emphysema lung shows reduced scattering in the periphery and the fibrotic lung lacks scattering areas in the central, peribronchial regions. A better three-dimensional assessment of the differences between the three cases, an animation of the rendered multi-modal volumes was generated. Example screenshots of the movie are shown in Figure 3.20.

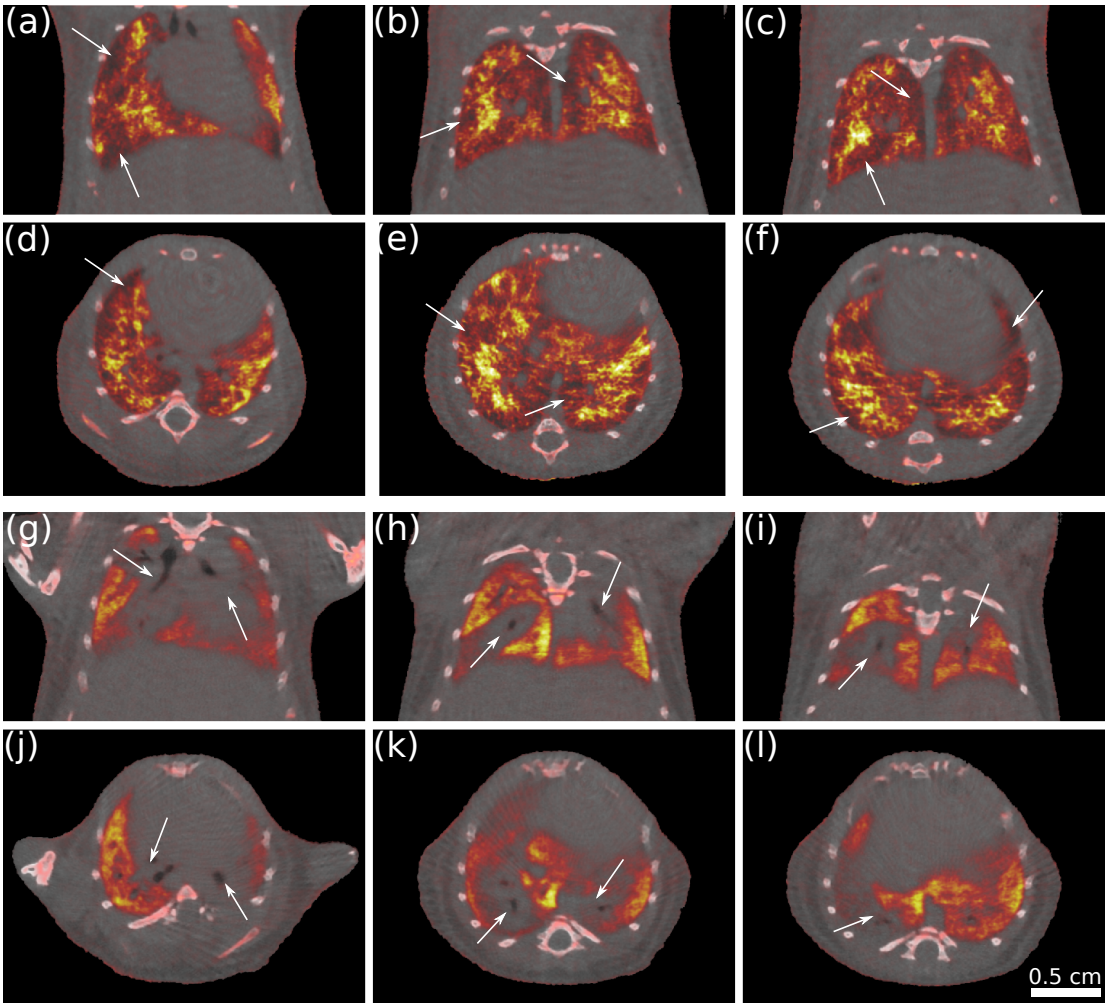

Figure 3.18: Fusion images of attenuation and dark-field CT of a mouse with emphysematous lung ((a)-(f)) and a mouse with fibrotic lung ((g)-(l)) at different positions in the three-dimensional volume. Emphysema case: Dark red areas indicating regions with strongly reduced scattering abilities (but little absorption) appear preferentially in the peripherals of the lung (white arrows). (a)-(c): Anterior to posterior coronal slices. (d)-(f): Cranial to caudal axial slices. Fibrosis case: Red areas exhibit reduced scattering ability compared to bright yellow regions and match here with excessive tissue marked by enhanced absorption in attenuation CT. Arrows indicate the preferential spreading of the scarring along the bronchi. (g)-(i): Anterior to posterior coronal slices. (j)-(l): Cranial to caudal axial slices.

The strong difference in the identically windowed scatter-based gray-values between the cases (Fig. 3.16g-l), suggests that differentiation between diseased and healthy tissue merely based on DF signal strength is possible. For a closer analysis, the histograms of the three lung-tissue volumes (including a non-scattering soft-tissue margin) are shown in Figure 3.21. In attenuation-based CT — and

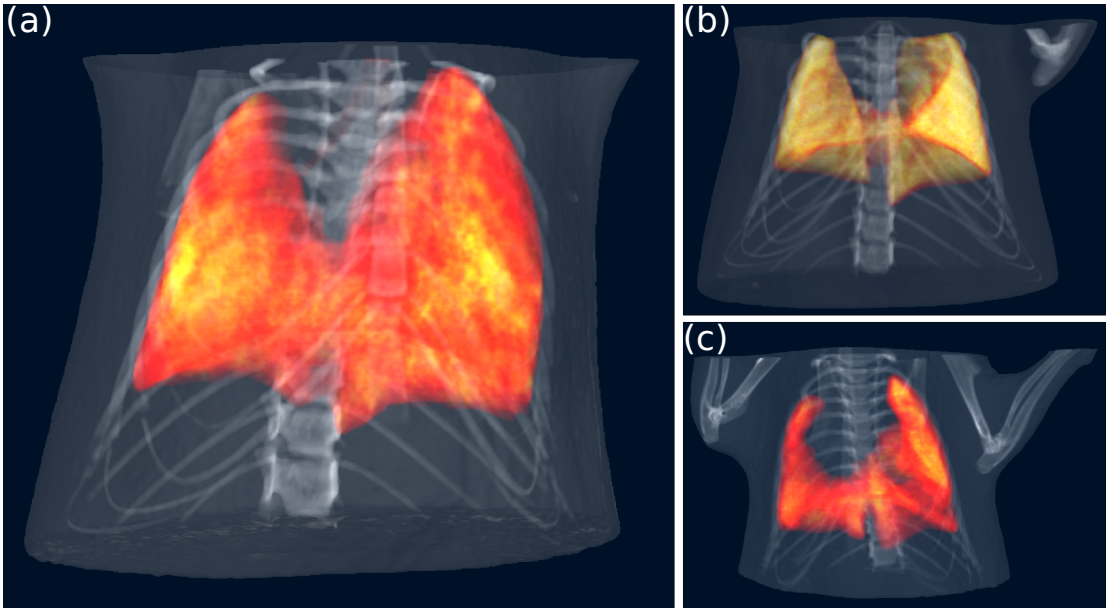

Figure 3.19: Volume renderings of (a) emphysematous, (b) control and (c) fibrotic case. The skeletal structure was segmented from attenuation CT, whereas the lung tissue was extracted from dark-field CT and represented by a semi-transparent hot color map.

recently in phase-contrast CT (Donath et al., 2010) — , universal Hounsfield Units (HU) were established to facilitate comparability of data acquired at different scanners. As an analogue approach, we introduce scatter-based Hounsfield Units (HUs). The established HU scales are defined via their tomographically reconstructed signals for water (0 HU) and for air (-1000 HU), such that the HU number for tissue x is calculated via the linear attenuation coefficient μ_x in case of the attenuation HU scale:

$$\mathrm{HU}_x = 1000 \cdot \frac{\mu_x - \mu_{\mathrm{water}}}{\mu_{\mathrm{water}} - \mu_{\mathrm{air}}}. \tag{3.16}$$

However, this definition cannot be transferred to DFCT directly, since both water and air do not scatter and thus produce identical signals. Therefore, we suggest the usage of a zero-scatter reference area to determine 0 HUs. This can be either water or air, or – in our case – non-scattering solid soft-tissue, as it is included in the histogram-analyzed volume for each of the three cases. The non-scattering parts form the three overlapping peaks to the left of the histogram range. To span a range of 1000 HUs the peak position of the strongest scatterer in the measurements, the control lung, is proposed as reference point for 1000 HUs. Using the linear diffusion coefficient ε_x as a measure for the scattering strength of

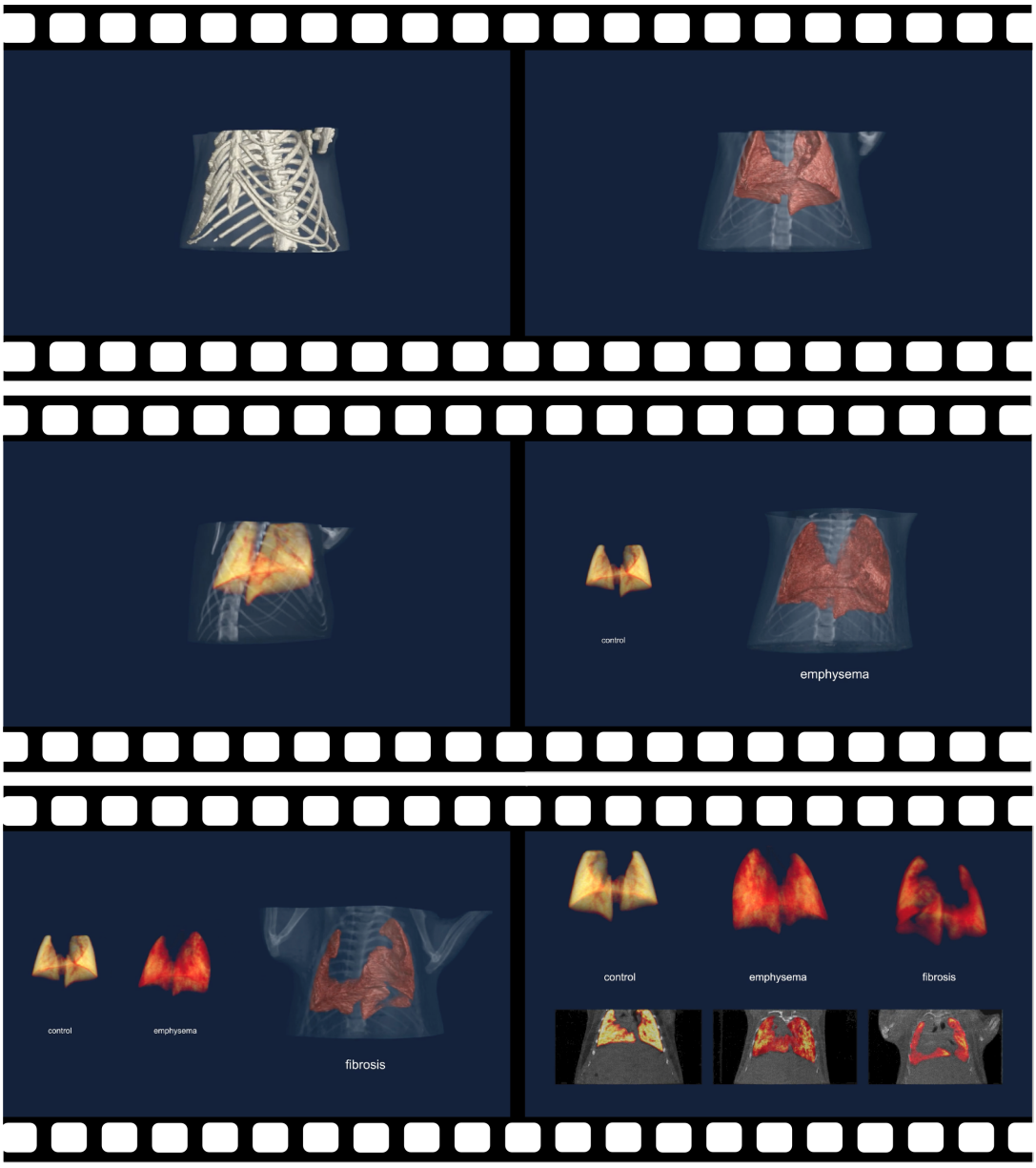

Figure 3.20: Screenshots of a movie containing the multi-modal volume renderings of the three imaged *in vivo* mice. The movie first provides a naturalistic depiction of the anatomy for healthy, emphysematous and fibrotic lung contained in the rib cage. It then switches to a display of the three-dimensional scattering power, i.e. the functional alveoli distribution. Finally, a tour through the fused datasets is shown in comparison for all three cases in coronal view. The movie can be watched here: http://youtu.be/WeiADQ0h3B4.

a material x as suggested by Bech et al. (2010), the following definition is obtained:

$$\mathrm{HUs}_x = 1000 \cdot \frac{\varepsilon_x - \varepsilon_0}{\varepsilon_{\mathrm{Control}} - \varepsilon_0}. \tag{3.17}$$

where ε_0 is the linear diffusion coefficient of a non-scattering area, ideally equal to 0, and $\varepsilon_{\text{Control}}$ describes healthy lung tissue. Hereby, destruction of alveolar structures results in a shift of the main pulmonary peak towards the zero-scatter point, as it is the case for the emphysematous lung with a peak position at approximately 373 HUs. Elimination of the air-filled voids is so advanced in some areas of the fibrotic lung, that the pulmonary peak merges into the zero-scatter peak in this case. The increased peak height of the zero-scatter peak reflects the substitution of those voids by non-scattering solid soft tissue.

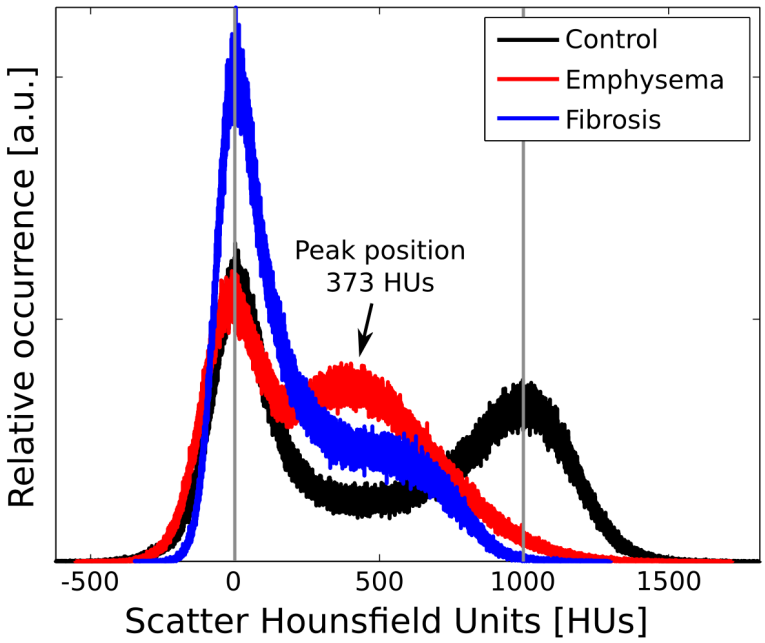

Figure 3.21: Histograms of the scatter-based gray values of the extended lung region of dark-field CT volumes of control (black), emphysematous (red) and fibrotic (blue) mouse. The gray values are scaled according to the novel scatter Hounsfield Units (HUs) introduced in the text. The pathophysiological changes of emphysematous and fibrotic lung cause a shift towards lower HUs. Peaks at 0 HUs correspond to non-scattering solid soft-tissue areas surrounding the actual alveolar lung region.

The presented results reflect a proof-of-principle demonstration of *in vivo* DFCT imaging and its possible benefits for non-invasive evaluation of pulmonary pathophysiology. For a detailed analysis of sensitivity and specificity for diagnosing various lung diseases, studies with larger sample sizes and several disease stages are required. To this end, the results show that this is in general feasible, as dose-compatibility for longitudinal studies on small animals is given. Moreover, to serve for sound establishment of the suggested lung-specific HUs reference point, a whole atlas of healthy lung measurements should be developed, which

is beyond the scope of this proof-of-principle study. Ultimately, a standardized lung phantom needs to be developed based on this atlas to guarantee reliable comparability of the HUs scale from different scanners, because the DF signal strength depends on various parameters such as feature (alveolar) size, x-ray energy, and interferometer specifications. Note that the applicability of a lung-based HUs scale to other DFI applications, for example bones (Potdevin et al., 2012), remains to be verified, since different applications may demand setups of higher sensitivity.
Despite the limited sample size of three cases, the presented results prove great potential for future lung imaging where volumetric information such as disease distribution is required. One example is the use of x-ray scatter CT for the evaluation of potential lung-volume–reduction surgery candidates (Washko et al., 2008) in case of emphysema. In general, mild stages of emphysema are difficult to diagnose solely by projection radiography and often dose-intensive HRCT is needed. Projection-based DFI may ultimately serve as a screening method (Schleede et al., 2012; Yaroshenko et al., 2013; Meinel et al., 2014b). It may be complemented by limited-angle or coarse-resolution DFCT to gain additional three-dimensional information without the necessity of very high dose, exploiting that DFI generates a signal from structure sizes below the resolution limit of the imaging system (Chen et al., 2010; Yashiro et al., 2010; Lynch et al., 2011). The presented CT results already serve as an example for non-optimized resolution settings, because they are subject to undersampling and breathing-motion artifacts due to non-gated acquisition and long exposure times. Another conceivable application of thoracic DFCT is to map suspicious pulmonary parenchyma in case of suspected fibrosis, without the need to force the spatial resolution down to the level of the secondary pulmonary lobule. This may allow to optimize the location choice for biopsy, which is still the gold standard for diagnosing idiopathic interstitial pneumonias and is currently done with the help of attenuation-based HRCT (Gross and Hunninghake, 2001).

3.7 Summary and outlook

In this chapter, the technological development of the first small-animal phase-contrast and dark-field CT scanner with rotating gantry, as presented by Tapfer (2013), was complemented by the adaption and development of various algorithmic approaches specifically to the scanner data in order to counteract image artifacts arising from instabilities of the interferometer and shortcomings of the imaging system in the CT scanner. Besides illustrating the effects of the algorithms on

scans of a phantom and a plastic toy, it was shown that the introduced software facilitates phase-contrast CT imaging of a fixated *ex vivo* mouse specimen with increased quality concerning sharpness and noise level. In particular, the application of regularized statistical iterative reconstruction was proven to allow for considerable undersampling while maintaining the information content in the image, compared to conventional filtered back-projection.
The most important result presented in this chapter is the successful application of x-ray grating interferometry with a conventional x-ray source and a rotating gantry to imaging of living animals. It covers proof-of-principle studies on both projection-based radiographic imaging as well as CT imaging (with SIR) with all three contrast modalities. The radiographic images showed a healthy mouse, whereas the CT study presented two mice with pulmonary disorders in addition to a healthy one.
In case of lung diagnostics, it was shown that the DF channel provides excellent information gain in CT. In contrast, the PC channel is more interesting for imaging of the abdomen, as Tapfer et al. (2013, 2014) showed for various mouse disease models. However, the signal-to-noise ratio for PC-CT at the Skyscan 1190 needs to be further improved to allow for *in vivo* abdomen CT.
Several technological measures are suggested for this purpose: The replacement of the gratings with structures on thinner silicon wafers would allow for a higher flux and consequently reduced noise. A more sensitive detector with a narrower PSF would support noise reduction and increase image sharpness. To improve the sensitivity, i.e. to be able to resolve smaller refraction angles, gratings with smaller periods would be necessary, because the inter-grating distances are fixed at the current rotating gantry, so that a transition to higher Talbot orders is not readily possible. However, smaller grating periods come at the cost of increased shadowing towards the margins. A way to counteract this effect is the use of gratings that are bent according to the fan angle as suggested by Thüring et al. (2011a). Both bent gratings (especially with very small radii as necessary for a source grating) as well as gratings with very small periods are still technologically challenging to produce for grating manufacturers.
To avoid the shadowing problem, the rotation of the grating-bar directions from along the long body axis of the animal to perpendicular to it is possible. In this case, instead of the width of the usable FOV, the height would be restricted by shadowing. Acquisition schemes constituting many height steps or helical patterns present a possible solution to overcome this restriction. However, rotating the grating-bar direction requires the integration of the differential phase signal prior to reconstruction and does not allow quantitative phase-contrast CT because of the unknown integration constant. DFCT, on the other hand, would still be feasible.

The use of gratings that are not composed of binary, but triangular structures, may represent a beneficial alternative for short setup designs as in the Skyscan 1190 (Yaroshenko et al., 2014). Triangular grating structures exhibit maximal visibility at very low distances behind the grating, due to their characteristic wave-propagation pattern.
To further reduce scan time, alternative acquisition schemes such as interlaced stepping (Zanette et al., 2011, 2012) or Fourier-based single-shot imaging (Bennett et al., 2010) can be applied, however – at least in the latter case – at the cost of spatial resolution.
The scanner with its current setup is ideally suited for the identification and evaluation of the diagnostic benefit of DF radiography and CT of pulmonary diseases. In this area of application the limited sensitivity of the setup actually represents a plus, as the strong scattering at lung alveoli saturates the dark-field signal at setups with higher sensitivity. Regarding radiography, two proof-of-principle studies performed at the Skyscan 1190 on excised murine lungs, one on emphysema (Yaroshenko et al., 2013) and one on lung tumor detectability (Meinel et al., 2014a) and several *in vivo* studies on the sensitivity and specificity of the method for pulmonary emphysema (Meinel et al., 2014b; Hellbach et al.) and fibrosis (Yaroshenko et al.) have been published or are submitted. Additional research on the possible diagnostic benefit at different stages of the diseases and on other pulmonary disorders are ongoing for radiography and CT.

Chapter 4

Contrast-enhanced dark-field radiography

After a brief introduction to microbubble-based contrast agents in Section 4.1, three in vitro studies on their use as potential dark-field contrast media are presented in this chapter. The first study (Section 4.2) evaluated the scattering ability of existing preclinical and clinical microbubble contrast media in a fixated state and has been published in Velroyen et al., "Microbubbles as a scattering contrast agent for grating-based x-ray dark-field imaging", Physics in Medicine and Biology (2013). In the second study an experimental agent based on polyvinyl-shell microbubbles was investigated in the presence of realistic noise-inducing structures. Its content presented in Section 4.3 has been submitted for publication in Velroyen et al., "Ex-vivo perfusion-simulation measurements of microbubbles as a scattering contrast agent for grating-based x-ray dark-field imaging". The third study in Section 4.4 addresses the influence of the coating of the bubbles onto the measured signal. With respect to the previously published and submitted manuscripts, the following changes have been carried out: Table 4.1 has been corrected for mistakes. The description of the setup has been shortened to avoid repetition and the introduction to this chapter has been adapted to the context of this thesis.

4.1 Introduction

Conventional x-ray imaging techniques in medical applications are based on the physical effect of attenuation of the rays in the tissue, including absorption and Compton scattering. Since the attenuation depends on the material density, the generated contrast is optimal for structures with large density differences, for

example between bone and soft tissue. To increase the otherwise poor contrast within soft-tissue types that have only slight density differences, the application of contrast media with high atomic numbers is common practice (Dawson, 1996). In conventional attenuation-based x-ray radiography and computed tomography, the use of iodinated contrast agents represents the gold standard for many diagnostic questions, for example for blood-vessel representation in projection angiography.
As discussed previously, recent technological developments in the area of x-ray PCI and DFI have advanced significantly towards the clinical applicability of the technique, for example PCI at high photon energies (Willner et al., 2013), interferometry using a rotating gantry (Tapfer et al., 2012), the usage of bent gratings for larger cone angles (Thüring et al., 2011a), grating manufacturing for larger fields of view (Meiser et al., 2014), and first *in vivo* imaging of mice (Bech et al., 2013; Velroyen et al., b). Even a first feasibility study for a clinically applicable PCI/DFI mammography setup has been conducted (Roessl et al., 2014). In the course of this general trend towards clinical applicability, naturally the question about dedicated contrast agents for this new technology arises, to improve feature visibility in a directed manner.
As suggested by various applications of DFI, i.e. representation of changes of the alveolar structure in lungs (Schleede et al., 2012; Yaroshenko et al., 2013), microcalcifications in breast tissue (Michel et al., 2013; Hauser et al., 2014) and depiction of scattering at the trabecular structure of bones (Potdevin et al., 2012), an agent consisting of many interfaces between materials of strongly different indices of refraction is considered optimal for DFI.
Therefore, a straightforward approach is the investigation of the scattering properties of clinically used microbubble-based contrast agents, which are widely applied in ultrasound imaging (Correas et al., 2001). The microbubbles consist of shells of lipid monolayers, protein, sugar, or polymer encapsulating air or inert gases, which are less soluble in water, resulting in an increased stability of the contrast agent in blood vessels (Dietrich, 2008). They usually have a diameter of several micrometers. This means that their size is comparable to erythrocytes, and they are able to pass small capillaries (Lindner et al., 2002). In ultrasound imaging, the compressibility and therefore high sensitivity to acoustic waves of the microspheres is exploited to yield enhanced image contrast(Morgan et al., 2000). Their diagnostic capabilities are numerous: They are used for imaging of the vascularization of tumours, in echocardiography, brain perfusion, and for investigations of various organs (Clark and Dittrich, 2000; Rim et al., 2001; Nielsen and Bang, 2004; Forsberg et al., 2007). In addition, targeted microbubbles allow for imaging of molecular and metabolic processes (Heppner and Lindner, 2005). A comprehensive review about the wide variety in composition and properties of available microbubbles and their biomedical applications in imaging and drug delivery is

given by Sirsi and Borden (2009).
Kogan et al. (2010) reported applications of microbubbles in imaging techniques other than ultrasound. Regarding x-ray imaging, Arfelli et al. (2010) first exploited the ultra-small-angle scattering of x-rays at gas-to-shell interfaces of the microbubble for contrast generation, using analyzer-based diffraction enhanced imaging (DEI) (Chapman et al., 1997) at a synchrotron source. Furthermore, microbubbles have been shown to increase contrast in propagation-based phase-contrast imaging using synchrotron radiation (Tang et al., 2011). Recently, Millard et al. (2013) presented a Monte-Carlo simulation approach for a quantitative description of scattering due to bubbles.
In the first study included in this chapter (Section 4.2, published in Velroyen et al. (2013)), clinically established microbubble-based contrast agents were measured *in vitro* to investigate their x-ray scattering ability. In one of the commercially available agents, Optison, x-ray scattering could be detected using Talbot-Lau interferometry and a polychromatic x-ray source. Furthermore, the feasibility of dark-field contrast-enhancement with a pixel size in the range of those of clinical x-ray scanners was demonstrated.
Unfortunately, Optison was taken off market and was not even available for *in vitro* research purposes any more, so that follow-up experiments were made impossible. Instead, in a subsequent study presented in Section 4.3 (Velroyen et al., a) an experimental contrast agent based on microbubbles consisting of a polyvinyl-alcohol (PVA) shell (Cavalieri et al., 2005) with an iron-oxide coating (Mahmoudi et al., 2011) was investigated. The agent is under development for multiple purposes, such as magnetic resonance (MR) imaging, molecular imaging, or ultrasound (US) imaging depending on the exact design parameters and functionalization of the surface (for example Brismar et al. (2012); Barrefelt et al. (2013)). Biocompatibility has been shown (Paradossi et al., 2010) and is further supported by a recent study that successfully applies a subspecies of this new agent to *in vivo* rats for MR and Single Photon Emission CT (SPECT) (Barrefelt et al., 2013).
To mimic conditions closer to the actual application to an animal, the PVA contrast agent was tested with the scattering background signal provided by a mouse carcass in DFI and compared to a clinically used iodine-based contrast agent. Hereby, the potential for application of microbubbles in *in vivo* small-animal angiography was evaluated.
Complementary to the study of PVA bubbles with mouse-background structures, two versions of the PVA-based microbubbles (one with and one without the iron-oxide coating) were tested in a more quantitative manner, to evaluate the influence of the coating onto to dark-field signal strength. The detailed methods and results of this study are presented in Section 4.4.

4.2 First *in vitro* study on (pre-)clinical microbubbles

This study demonstrates that ultrasound contrast agents based on microbubbles can be used to produce strongly enhanced dark-field contrast, with superior contrast-to-noise ratio compared to the attenuation signal. It is shown that this method works well with an x-ray tube-based setup and that the relative contrast gain even increases when the pixel size is increased from tenths of micrometers to clinically compatible detector resolutions of about up to a millimeter.

4.2.1 Materials and methods

4.2.1.1 Microbubble contrast agents and sample preparation

In this study, the x-ray scattering characteristics of three second-generation ultrasound microbubble contrast-agents were investigated.
Optison™ (by GE Healthcare AS, Oslo, Norway) is a suspension of microspheres consisting of human serum albumin, filled with the inert gas perflutren. The average amount of gas is 0.19 mg per ml contrast agent; one millilitre contains 5 - 8 $\times$ 10^8 protein-type-A microspheres with a mean diameter of 3.0 - 4.5 µm, a maximum diameter of 32 µm and 95% of them being smaller than 10 µm. No reconstitution of the contrast agent was necessary: By gentle mixing, the microbubbles were re-suspended to form an opaque, white liquid.
SonoVue® (by Bracco Imaging S.p.A., 10010 (TO), Italy) is a suspension of microbubbles consisting of a phospholipid shell filled with stabilized sulphur hexafluoride. After reconstitution of the agent by adding 0.9% saline solution to the powder-like lyophilisate, the concentration was 8 µl powder per ml contrast media, providing a bubble concentration of up to 5 $\times$ 10^8 per ml (Schneider, 1999). The mean diameter of the microbubbles is 2.5 µm with more than 90% smaller than 8 µm (Schneider, 1999).
Vevo MicroMarker™ (manufactured by Bracco Imaging, sold by VisualSonics, Amsterdam, Netherlands) is a microbubble contrast agent of similar constitution as SonoVue, with a shell made up of phospholipids. The bubbles contain a mixture of nitrogen and perfluorobutane gas. The freeze-dried powder in the vial was reconstituted by adding 0.7 ml of 0.9% saline solution. This way, a microbubble concentration of approximately 2.9 $\times$ 10^9 per ml was obtained. The median diameter in volume of these microbubbles is 2.3 - 2.9 µm.
If no flow or agitation was applied to the re-suspended contrast agents, bubbles accumulated at the air-liquid interface already within a few seconds. To avoid

this non-physiological accumulation of contrast in one distinct area, samples of contrast agent fixated in gelatin were prepared. For this purpose, 5 g of gelatin from porcine skin (Type A, Sigma-Aldrich Chemie GmbH, Steinheim, Germany) were dissolved in 100 ml desalted water during constant boiling, until a solution of about 40 ml was left. The gelatin mixture was allowed to cool down to approximately 40°C under permanent stirring. 0.5 ml of each of the three contrast agents, which had been reconstituted or re-suspended at room temperature as described above, were distributed to 1.5 ml plastic centrifuge vials and gently heated in a water bath to 37°C. Finally, 0.5 ml of the gelatin solution was added to each vial. The liquid in the vial was then gently sucked into and extruded from a pipette several times to gain a homogeneously mixed contrast-agent/gelatin solution and to re-suspend accumulated microbubbles. Afterwards, the vials were cooled down quickly in an icy water bath to avoid de-mixing or re-accumulation of the microbubbles and to encourage fast hardening of the gelatin. Desalted water instead of the contrast agent was used to create a reference sample.

4.2.1.2 Scan parameters

The experiments were performed at the Skyscan 1190, which is presented in detail in Section 3.2. The scanner was operated with the G2 grating with 25 µm high grating bars installed. The samples were placed in horizontal position on the sample stage. Phase stepping sets of 10 images each were taken at a source voltage of approximately 30 kVp and with an exposure time of 10 s per step, i.e. a total exposure of 100 s, to create one set of the trimodal images. The processed images cover a detector area of 930 × 970 pixels.

4.2.1.3 Data analysis

To obtain a quantitative measure for the contrast in the images of the three different microbubble contrast-agents, the contrast-to-noise ratio (CNR) of the absorption-based and dark-field images was calculated as

$$\mathrm{CNR} = \frac{|S_{\mathrm{CA}} - S_{\mathrm{Ref}}|}{\sigma_{\mathrm{Ref}}}. \tag{4.1}$$

S_{CA} and S_{Ref} denote the mean of the absorption or dark-field signal in a certain region of interest (ROI) in the contrast-agent (CA) sample and the reference (Ref) sample, respectively. The regions of interests were manually chosen areas of 64 x 64 pixels in the center of the cylindrical part of the vials, shown for the Optison exsample by the blue boxes in Figure 4.2. σ_{Ref} represents the standard

deviation of the according signal in the ROI of the reference sample, as a measure for noise in the image.
To demonstrate the feasibility of dark-field contrast enhancement in setups with potentially larger pixel size, a series of binned images of the Optison measurement was created, using 2 × 2, 4 × 4, 8 × 8, 16 × 16, and 32 × 32 binning of the raw image data, before extracting the absorption-based and dark-field images from the raw stepping scan data. The ROI size was adapted accordingly to cover the same physical region. The same CNR analysis as described above was then applied to the binned images.

4.2.2 Results and discussion

Figure 4.1 displays the Optison sample next to the reference sample imaged in three different contrast modalities. The conventional absorption-based projection image in Figure 4.1a shows no significant contrast enhancement between the reference and the contrast-agent sample, because the microbubbles mainly consist of elements with low atomic numbers. The differential phase-contrast image (Figure 4.1b) enhances the edges of the sample containers, because they strongly refract the x-ray wave-front passing through the sample. The wavefront perturbation induced by the bubbles is not resolved in the differential phase signal. On the contrary, the scattering-based dark-field image in Figure 4.1c shows a clearly enhanced signal in the right vial containing the Optison contrast agent, due to x-ray scattering at the interfaces between the gas and the shell of the bubbles.

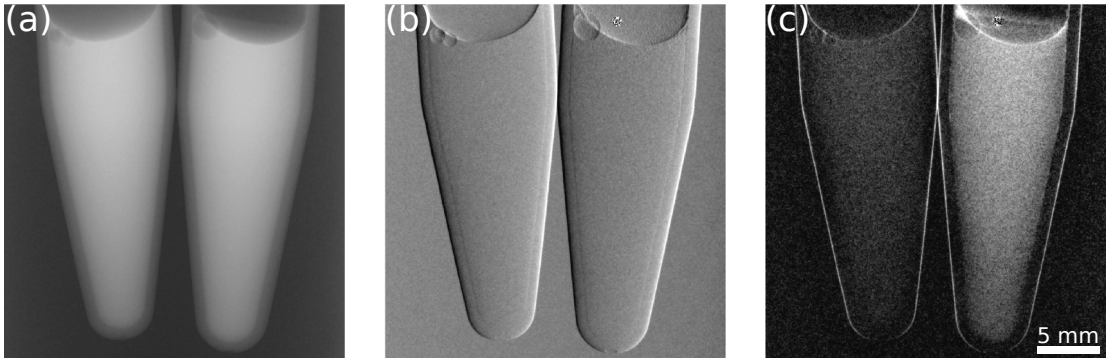

Figure 4.1: Microsphere-based contrast agent Optison fixed in gelatin (right container) versus reference sample (water in gelatin, left container), imaged in three different modalities with the range of the grey values given in brackets. (a) conventional absorption-based image [0, 0.6], (b) differential phase-contrast image [-0.6, 0.6], (c) dark-field contrast image [0, 0.4].

Figure 4.2a-c shows the unbinned dark-field image in comparison to the 4 × 4 and the 16 × 16 binned dark-field images of the Optison sample measurement at

30 kVp. Noise reduction and contrast gain due to binning are clearly visible. Figure 4.3 shows the resulting CNR values of dark-field and absorption-based images for the binning series. The values clearly indicate that the dark-field signal gains much more from the noise reduction due to binning than the absorption signal, since the CNR of the dark-field signal increases from 6.88 to 78.82 in the binning series up to 32-fold binning. The CNR of the absorption signal only rises slightly from 1.41 to 1.75 for the binning series up to 8-fold binning. For the 16- and 32-fold binning case, the dark-field CNR is still increasing, whereas the absorption CNR drops to 1.62 and 1.06. This phenomenon could be caused by low statistics, since for example the region of interest in the 32-fold binning case only consists of 2×2 pixels. Taken as a whole, the binning series demonstrates clearly the ability of the dark-field signal to generate contrast from microstructures with sub-pixel sizes (Chen et al., 2010; Bech et al., 2010).

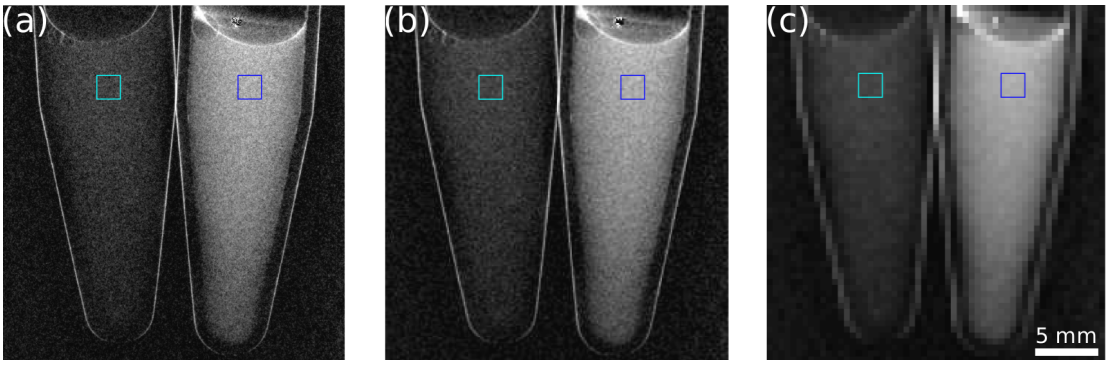

Figure 4.2: Dark-field images of the reference (left container) and Optison sample (right container) in three different binning stages: (a) 1×1 pixels, (b) 4×4 pixels, (c) 16×16 pixels. The blue boxes indicate the regions of interest in which the CNR was calculated (see Figure 4.3). The greyscale range is [0, 0.4].

Unexpectedly, not all contrast-agent samples provided an equally strong x-ray dark-field signal enhancement. Table 4.1 lists the raw signal values in the ROI as well as the CNR values calculated from the dark-field and absorption signals for each of the three contrast agents, for the unbinned case. Unlike the contrast enhancement observed with the Optison sample, the CNRs of SonoVue and Vevo MicroMarker are not significantly different between dark field and absorption.

The reason for the different contrast behavior of the Optison sample compared to the SonoVue and Vevo MicroMarker samples is not clear. The dark-field contrast sensitivity for different microstructure particles is dependent on the imaging-system parameters (Lynch et al., 2011) and thus varies for different bubble sizes in one system. Since the exact bubble-size distributions of each tested contrast-agent brand is not publicly available except for SonoVue (Schneider et al., 1995), it can-

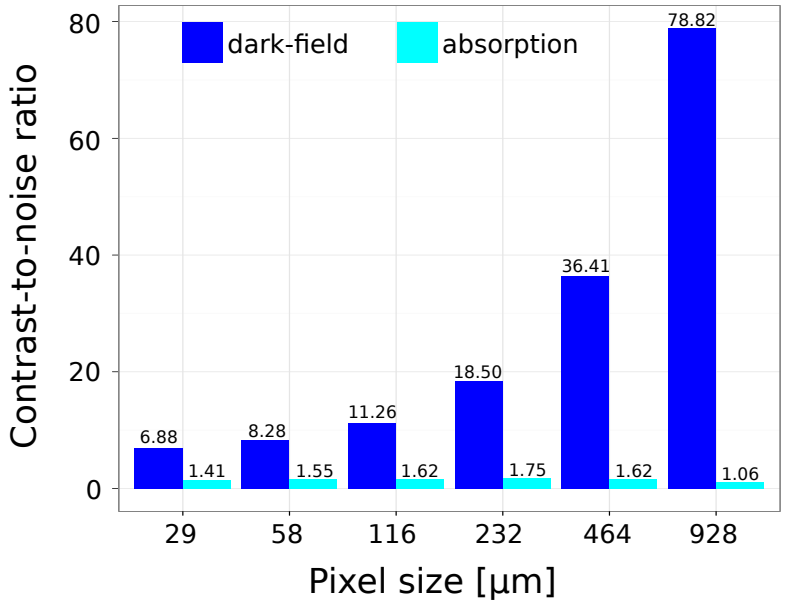

Figure 4.3: Bar plot of the contrast-to-noise ratio (CNR) in comparison for dark-field and absorption image at different binning stages for the Optison sample. The CNR was calculated in a region of interest of 64 × 64 pixels for the unbinned case, and down to 2 × 2 pixels in the 32-fold-binning case.

		S_{CA}	S_{Ref}	σ_{Ref}	CNR
SonoVue	dark field	0.889	0.905	0.029	0.55
	attenuation	0.540	0.538	0.003	0.67
Vevo MicroMarker	dark field	0.898	0.933	0.027	1.30
	attenuation	0.517	0.524	0.005	1.40
Optison	dark field	0.735	0.904	0.025	6.76
	attenuation	0.547	0.542	0.004	1.25

Table 4.1: Signal strength of the contrast agent sample (S_{CA}) and the reference sample (S_{Ref}), and the standard deviation (σ_{Ref}) of the reference sample as a measure for noise, for dark-field and absorption images in comparison for different contrast agents. The contrast-to-noise ratio (CNR) was calculated from these values taken from regions of interest of 64 × 64 pixels in the center of the cylindrical part of the centrifuge vials.

not be stated whether or not these differ significantly such that they could cause the strong difference in contrast enhancement. To investigate the bubble-size dependence more generally, a simulation study for different sizes of gas-filled spheres in water, similar to those presented in Malecki et al. (2012), was performed* with parameters adapted to the geometry and the interferometric components of the

*The simulation was carried out by A. Malecki, co-author of the according publication.

experimental setup used in this work. Different volumes were simulated: In between the different simulated volumes the diameter and the number of spheres was varied, while keeping the volume fraction occupied by the gas constant. As a simplification, within the same volume all spheres had the same diameter. The variation of the diameter revealed an optimal dark-field contrast sensitivity at diameters between 2 and 5 µm, as can be seen in Figure 4.4. Thus, the mean bubble sizes of the tested microbubble brands already comply well with the optimal diameter.

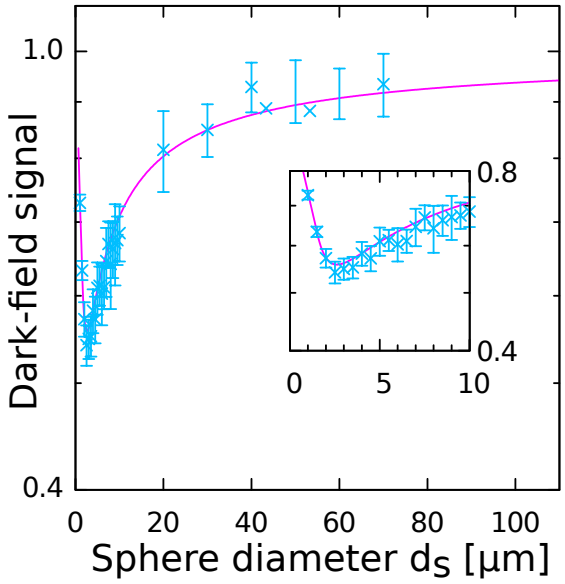

Figure 4.4: Simulated dependence of the dark-field signal on the diameter d_s of the microbubbles. The simulations were carried out according to Malecki et al. (2012) with a point source to create a cone beam as in the experiment. The total volume fraction of the gas distributed on the equally sized spheres was kept constant. From left to right the sphere diameter increases from 1 µm up to 10 µm in steps of 0.5 µm and from 10 µm up to 75 µm in steps of 5 µm. The number of spheres changes accordingly. To visualize the details in the region of maximum sensitivity the inset shows a magnification of the results below 10 µm. The magenta-colored line shows the theoretical value according to Lynch et al. (2011), modified by a magnification factor that takes the cone-beam geometry into account.

The refractive index change between gas and the surrounding medium (i.e. water and gelatine) dominates over a comparatively thin, and thus negligible, lipid or protein shell and over diminutive variations of the refractive index of different gas fillings. Therefore, the contrast-agent inherent difference in the shell constitution of the microbubbles is assumed not to cause such large variations in dark-field contrast level, as seen in this study.
Since SonoVue and Vevo MicroMarker shells consist of phospholipids, whereas the Optison shell is based on human serum albumin, the question can be posed

whether the phospholipid shell does not properly form in the *in vitro* situation. As this case cannot be ruled out completely, it is of high importance to test the potential dark-field contrast agents in the *in vivo* situation for which they were designed and in which they would stay intact. *In vivo*, the requirement of flow and turbulence to avoid accumulation of bubbles is fulfilled without any potential changes of the microbubbles because of an unphysiological environment. To exclude that the process of gelatin-mixing and hardening affected the contrast agent types differently, a control measurement with the pure, non-fixated, and - to avoid any possible reason for destruction - very gently reconstituted contrast agents was performed, hazarding the consequence of bubble accumulation. This measurement confirmed the result obtained with the gelatin-fixated samples: Optison showed a much more enhanced dark-field contrast than SonoVue and Vevo MicroMarker, although the accumulation of bubbles appeared similar to the naked eye (see Figure 4.5).

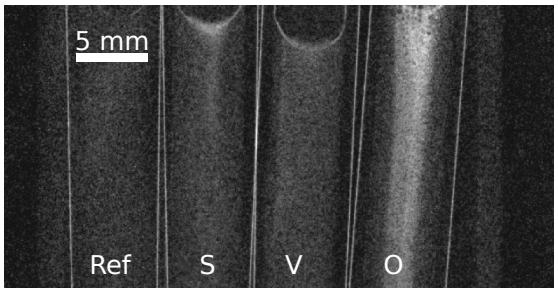

Figure 4.5: Dark-field image of a reference sample (Ref) of pure water, and the three pure microbubble contrast agents: SonoVue (S), Vevo MicroMarker (V), and Optison (O), in 1 ml syringes. DF values scaled from 0.0 to 0.4.

Another finding to be pointed out is that the Vevo MicroMarker cannot generate enhanced dark-field contrast, even though its concentration of microbubbles is one order of magnitude higher than the concentration of Optison.
The contrast strength of the microbubble contrast-agent depends on different parameters: The dark-field signal strength scales with the number of bubbles (or shell-gas-interfaces) in the beam path. Therefore, the bubble concentration in the contrast agent as well as the sample thickness contribute to the signal strength in a dark-field radiography image. This implies that an *in vitro* simulation of the signal to be expected *in vivo* is challenging due to varying blood vessel or lumen size in the animal, as well as the dynamic intermixture of blood and contrast agent resulting in locally different concentrations. These open questions can only be reasonably approached by actual proof-of-principle *in vivo* measurements. The influence of the structures present in a living animal that contribute to a background signal, such as bones and fur, is investigated in a subsequent

study presented in Section 4.3. Besides these environmental dependencies, the contrast also depends on the grating pitch and x-ray energy, i.e. the design of the grating interferometer.
The objective of this work was to show the feasibility of using microbubble-based ultrasound contrast agents as a contrast medium for x-ray dark-field imaging. Future experiments have to identify the optimal microbubble contrast-agent for x-ray dark-field imaging concerning stability, bubble size, and concentration. Also, a redesign of existing microbubble contrast agents specifically for dark-field imaging should be considered to optimize parameters like concentration or microbubble size within the limits of pharmacological safety and tolerance. Furthermore, the acquisition protocol for contrast enhanced dark-field projections needs to be optimized in terms of time and dose reduction, which exceeds the scope of this study. Further investigations might allow new clinical applications such as multimodal ultrasound and x-ray imaging, for example in angiography, as well as a diagnostic alternative to the administration of iodine-based contrast agents, once dark-field imaging is clinically established.

4.2.3 Summary

Based on the investigation shown in this section, it can be concluded that the clinical ultrasound microbubble contrast-agents Optison can be successfully employed to create contrast-enhanced dark-field images that are acquired using a Talbot-Lau interferometer. In particular, the contrast enhancement was demonstrated to be excellent for large pixel sizes. This, together with the high potential of the implementation of Talbot-Lau interferometry into a clinical environment, strongly promote the use of microbubbles as a dedicated dark-field x-ray contrast-agent. This has so far only been shown at analyzer-based setups with synchrotron radiation.

4.3 *Ex vivo* perfusion-simulation measurements of microbubbles

In this study, an experimental contrast agent based on microbubbles consisting of a polyvinyl-alcohol shell with an iron oxide coating is investigated, which has been originally developed for multimodal imaging and drug delivery. Its performance as a possible contrast medium for small-animal angiography is examined using a mouse carcass to realistically consider the attenuating and scattering background signal. Subtraction images of dark field, phase contrast and attenuation

are acquired for a concentration series to mimic different stages of dilution of the contrast agent in the vascular system. The images are compared to corresponding ones generated with the gold-standard, iodine-based contrast agent Solutrast, showing a strong contrast improvement by microbubbles in dark-field imaging. This study proves the feasibility of microbubble-based dark-field contrast enhancement in the presence of scattering and attenuation due to mouse body structures like bone and fur. Therefore, it suggests a high potential of the use of polymer-based microbubbles for small-animal dark-field angiography.

4.3.1 Materials and methods

4.3.1.1 Contrast agents

Two different contrast agents were used in this study. The main focus lies on the magnetically coated microbubbles with the notation DMM150 manufactured by Surflay Nanotec GmbH, Berlin, Germany. The bubbles consist of a shell based on polyvinylalcohol (PVA), coated with four layers of super paramagnetic iron oxide (Fe_3O_4) nanoparticles (SPION). A 100 % PVA bubbles suspension corresponds to a concentration of 5×10^9 bubbles/ml. In addition, the PVA bubbles were also measured diluted to 10 % and 1.3 % concentration. According to the manufacturer, the relative magnetization of this batch corresponds to 6.95 mg iron per 10^9 bubbles, resulting in an iron oxide amount of 9.6×10^{-12} g per bubble. The amount of PVA per bubble is reported by the manufacturer as 3.2×10^{-12} g. The thickness of the PVA shell lies between 400 and 600 nm. The SPION layers are coated onto the outside of the PVA shell by covalent coupling with alternating thin polyelectrolyte layers. The manufacturer determined the mean outer diameter of the bubbles by visual inspection via a microscope of a stained batch on 20 bubbles to be 5.5 ± 0.7 µm.
For gold standard comparison, the clinically used iodine-based x-ray contrast agent Solutrast® 300 (Bracco Imaging Deutschland GmbH, Konstanz, Germany) was used as a reference, pure and diluted to 10 % volume concentration.

4.3.1.2 Scan parameters

As in the previous study, the measurements were performed at the Skyscan 1190, which is presented in detail in Section 3.2. The improved G2 grating with deeper line structures (45 µm) was used. The detector was operated in 2x2 binning mode, resulting in an effective pixel size of 58 µm. The x-ray source was operated at maximum power at the peak voltage of 35 kVp, with a current of 525 µA. For a

preliminary contrast comparison, a reference sample of pure water and the pure PVA bubble suspension were measured in identical plastic vials of 4.2 mm inner diameter (in the cylindrical part). Each phase-stepping scan had 5 phase steps with 3.33 s exposure, resulting in a total exposure time of 16.65 s for one set of trimodal images.
For the main experiment, a mouse carcass was used to gain a proper representation of background signal in terms of bone structure and fur for contrast-agent testing. To be able to reliably locate the contrast-medium position, a plastic tube with an inner diameter of 1.6 mm was surgically implanted underneath the peritoneum entering at the chest and exiting in the lower abdominal area. The tube was fixated using thin sewing threads. The experimental protocol used with PVA bubbles (100 %, 10 %, 1.3 %) and Solutrast (100 %, 10 %) started with the injection of 0.3 to 0.4 ml of contrast agent, so that the main part of the implanted tube was filled with contrast medium. In each experiment the carcass was imaged twice: once with contrast agent in the tube, and once with water flushed into the tube. Both sets were taken with 10 steps and 5 s exposure time per step. The accumulated dose corresponds to approximately 5.7 mGy for both sets together (for the determination of the dose, see Section 3.5, Table 3.2).
To verify that the bubbles from the measured batches were intact, a small amount was imaged using a Zeiss Axiovert Light Microscope with 20-fold magnification lens.

4.3.1.3 Subtraction image processing

Prior to subtraction of the non-enhanced from the contrast-enhanced scan, the three complementary image signals of transmission, dark-field and differential phase were extracted from the raw phase stepping sets.
Opening the specimen chamber and attaching the syringe in between the two scans (with and without contrast agent) could have introduced a relative displacement of carcass and tube. To reduce the resulting artifacts in the subtraction images, a simple rigid registration procedure was performed based on the dark-field signal channel: The non-enhanced and the contrast-enhanced images were shifted relative to each other to find the maximum correlation between the two scans. After this, the non-enhanced image was subtracted from the contrast-enhanced image so that an image containing only residual noise and the signal created by the contrast agent was obtained.
Towards lower contrast-agent concentrations, the contrast agent signal started to enter the regime of statistical image noise, but was still visually distinguishable. For a clearer discrimination, in addition to the raw subtraction signal, a second representation of the subtraction images was created by further re-binning by a

factor of two and additional means of noise reduction: First, to isolate the true contrast-agent induced signal, any signal that would appear outside of the sample area (i.e. where the transmission was around unity) was masked out. Second, due to the deep grating structures, the cone-beam geometry of the setup causes shadowing in regions far from the optical axis (Thüring et al., 2011a) leading to fewer counts, increased noise and reduced visibility. Thus, the areas near the left and right margins of the field of view were masked out using a visibility map from a reference scan. Third, individual median filtering was applied to reduce noise and enhance connected areas. Subsequently, the masked and median-filtered signal was displayed by a hot colour scheme superimposed on the original transmission image in the areas where a threshold was reached. The individual parameters for filter kernel size and threshold were chosen based on best visual appearance and feature clarity as follows: PVA 100 % 5 pixels squared, 0.05 threshold; PVA 10 % 9 pixels squared, 0.025 threshold; PVA 1.3 % 9 pixels squared, 0.015 threshold; Solutrast 100 % 5 pixels squared, 0.05 threshold; Solutrast 10 % 9 pixels squared, 0.015 threshold.

4.3.2 Results and discussion

In vitro images of the magnetically coated PVA bubbles and a water reference sample are shown in Figure 4.6b and c. The PVA bubbles clearly show a stronger dark-field signal than water. Transmission is also reduced by the coated PVA bubbles, but this reduction is not as strong as in the dark-field signal. Note that, as common in radiology, in the presented attenuation images black corresponds to high transmission or low attenuation and white to low transmission or high attenuation. In case of the dark field signal, black codes low scattering, whereas white depicts strong scattering. Since the PVA bubbles had not been fixated, they accumulated at the upper surface of the round vial (i.e. along the vertical axis of the containers). Because of the resulting inhomogeneous bubble distribution, a reliable quantitative analysis of the signal could not be performed. However, these images serve to deliver a qualitative impression of the difference in x-ray scattering power between pure water and coated PVA bubbles. In this study, fixation or gelification was abstained from in order not to alter the chemical and osmotic environment and risk bubble destruction. To check if intact bubbles were present in the sample, small amounts of the suspensions were extracted and inspected via visible-light microscopy: Figure 4.6d shows intact bubbles.

The results of the subtraction imaging series are shown in Figures 4.7-4.10. As expected, the pure, clinically available, iodine-based Solutrast strongly absorbs x-rays, so that in the attenuation image in Figure 4.7b the contrast-agent filled

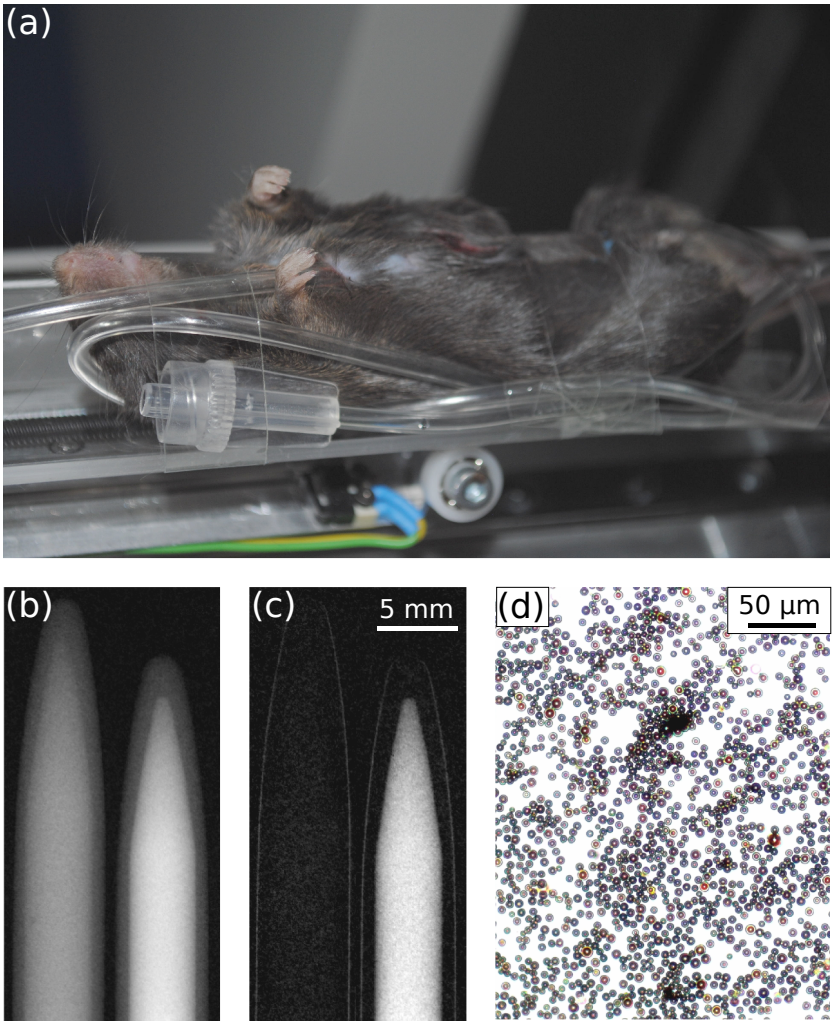

Figure 4.6: (a) Mouse carcass fixated on the animal bed of a preclinical phase-contrast and dark-field CT scanner. A plastic tube was surgically inserted underneath the peritoneum and some spare volume of the tube for flushing the contrast agent downwards was attached to the right side of the mouse. (b) Conventional attenuation image of plastic vials containing water (left) and PVA microbubbles (right). Grey values ranging from 0 to 0.35. (c) Dark-field image of plastic vials containing water (left) and PVA microbubbles (right). Grey values ranging from 0 to 0.75. (d) Visible-light brightfield microscopy image of PVA microbubbles.

tube is clearly visible. The subtraction image in Figure 4.7c shows that the signal strength is well above the noise background. In Figure 4.7a, the tube inserted underneath the peritoneum is filled with water. Since this image was acquired after the one in Figure 4.7b, the contrast agent that was pushed onward is visible in the spare tube part positioned next to the carcass on the left margin of the image. These left-over contrast agent portions from prior measurements are the reason

why also in some of the following subtraction images signal enhancement can appear in this area. For the sake of completeness, Figure 4.7d through f show the differential phase signal of the measurement with water and the one with Solutrast in the tube, as well as the subtraction image. They demonstrate that, due to the differential nature of the phase signal, the subtraction is dominated by movement of the spare tube and evolving gas bubbles in the intestines. Figure 4.7 g through i show the dark-field signal of the acquisition with water, with pure Solutrast and their subtraction. The tube containing the contrast-agent hardly shows up in the direct dark-field image, but is visible in the subtraction image. However, the generated dark-field signal is much weaker than the attenuation signal, since Solutrast is a homogeneous fluid. In fact, the occurring reduction in visibility, which leads to the visible dark-field signal, can most likely be attributed to beam-hardening of the x-ray spectrum. Since the visibility of the interferometric image is strongly dependent on the energy of the x-rays, it can decrease if the (more optimal) lower energies are filtered out by the sample (Chabior et al., 2011), i.e. the contrast agent, resulting in an enhanced dark-field signal.

Figure 4.8 shows the corresponding non-enhanced, contrast-enhanced, and subtraction images for all three modalities for the pure, SPION-coated PVA bubbles. Contrary to the Solutrast measurements, in the case of PVA bubbles, the dark-field signal generated by the bubbles in the tube is sufficiently strong to clearly stand out in the contrast-enhanced dark-field image (Figure 4.8h). The subtraction image in Figure 4.8i shows a signal strength well above the noise background. The absorption in the coated shell generates a visible, but much weaker, signal in the attenuation image (Figure 4.8b and c). In fact, the attenuation subtraction image is dominated by gassing in the intestines. As in Figure 4.7, the differential phase signal does not show a relevant change due to the contrast agent (Figure 4.8d through f).

Although the pure PVA bubble contrast agent used for Figure 4.8 is not compatible with *in vivo* measurements in mice, other animals (e.g. rats) are tolerant to such a high dose of magnetite-coated PVA microbubbles, and images could be obtained under the assumption that the imaging system was fast enough to capture the first pass of a bolus injection into a large vessel. To simulate lower contrast-agent doses or dilution in the blood vessels, contrast-enhanced subtraction imaging with lower PVA bubble concentrations was performed. Figure 4.9 shows the dark-field subtraction images of 100 %, 10 % and 1.3 % PVA bubbles concentration in comparison, as well as the respective filtered subtraction signal superimposed on the original transmission image for an improved anatomical orientation. Although the signal strength of the contrast-agent filled tube reaches the noise level when the bubble concentration is reduced, the human eye can

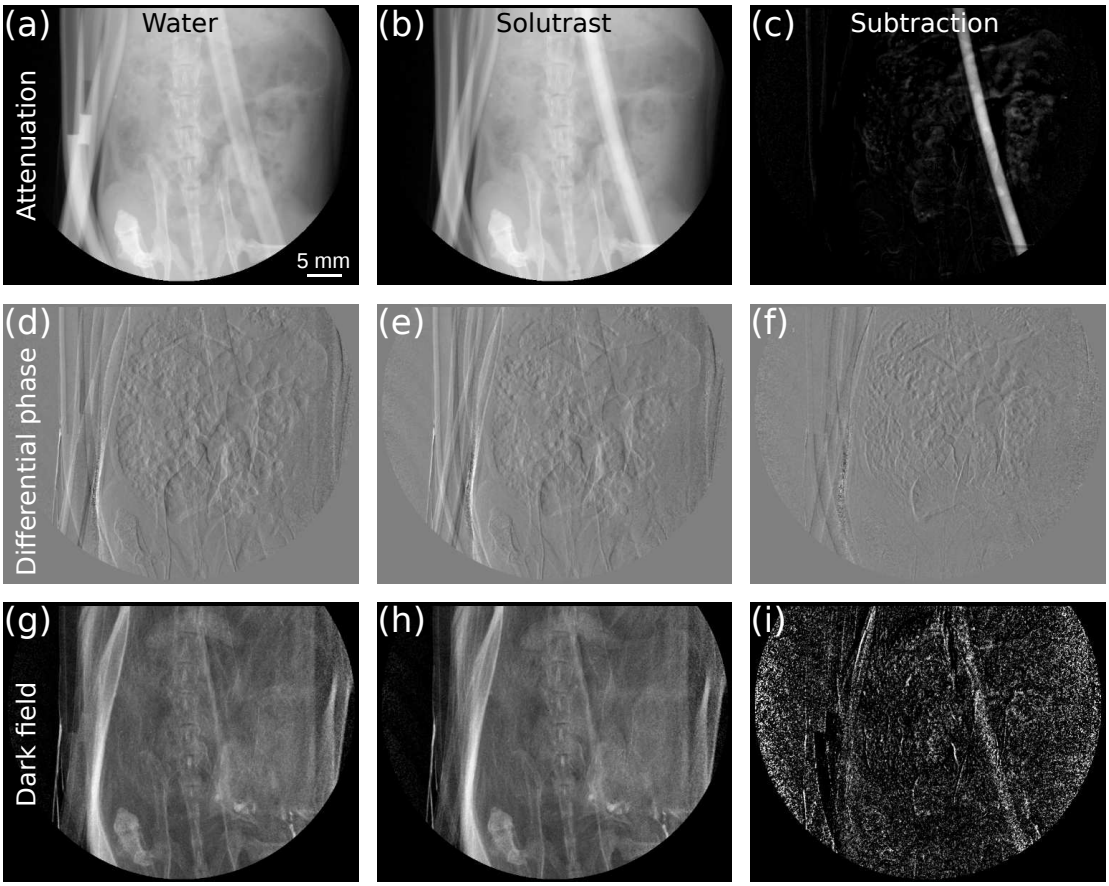

Figure 4.7: Measurement of pure Solutrast contrast agent. Grey value scaling is given in brackets. The first column shows the same image with the tube filled with water for three different contrast modalities: (a) attenuation [0, 0.9], (d) differential phase $[-\frac{\pi}{2}, \frac{\pi}{2}]$, (g) dark field [0, 1.0]. The second column shows the same image with the tube filled with pure Solutrast: (b) attenuation [0, 0.9], (e) differential phase $[-\frac{\pi}{2}, \frac{\pi}{2}]$, (h) dark field [0, 1.0]. The third column shows the subtraction of the image with contrast agent (second column) from the image with water (first column) for the three different contrast modalities: (c) attenuation [0, 0.2], (f) differential phase $[-\frac{\pi}{2}, \frac{\pi}{2}]$, (i) dark field [0, 0.13].

still discern the tube-shaped true signal from the noise background even for the lowest measured concentration. The overlaid and filtered signals in hot colour scheme in Figure 4.9d and f show that, besides the true signal in the tube of interest, only the signal in the spare volume of the tube (fully explicable by residual contrast agent from the prior contrast-agent shot with higher concentration) and some smaller noise patches due to residual motion artefacts light up in the mouse anatomy. These results indicate the feasibility of contrast-enhanced perfusion dark-field imaging of the larger vessels in small animals.

For a complete comparison with the gold-standard iodine contrast agent, the cor-

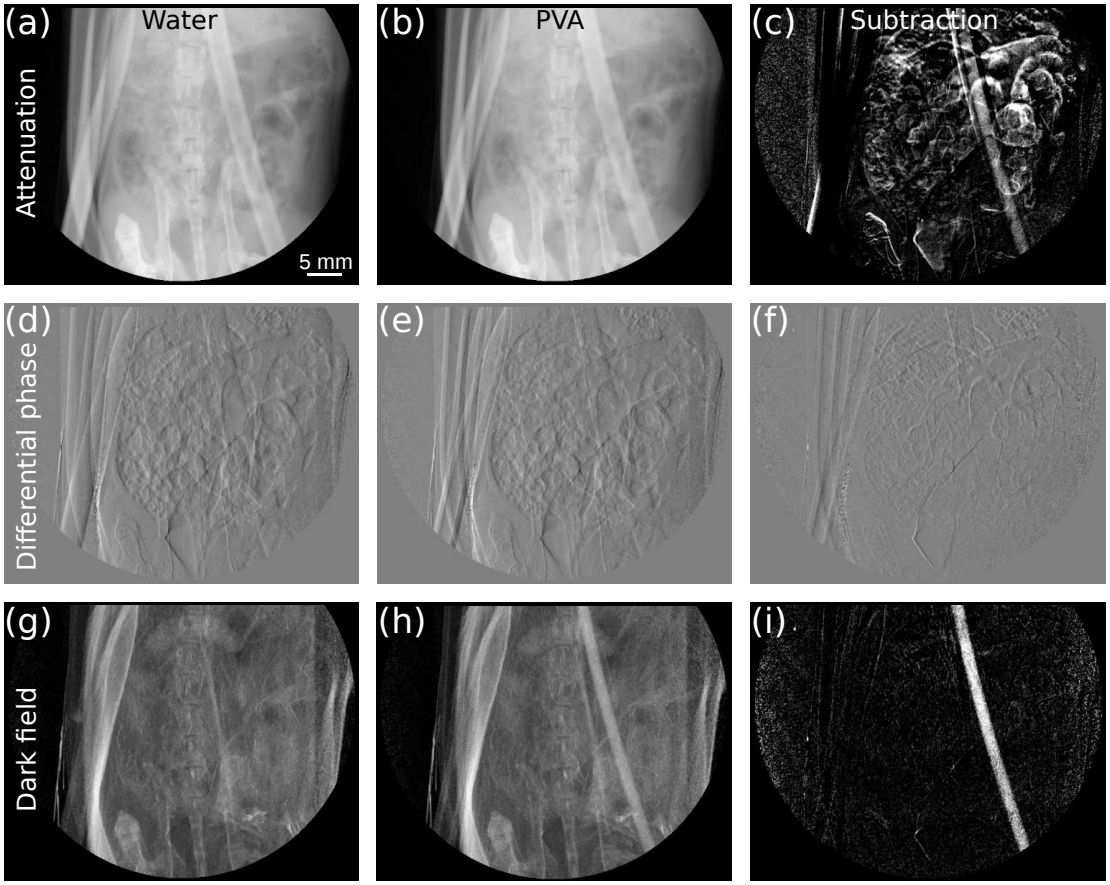

Figure 4.8: Measurement of pure PVA bubbles contrast agent. Grey value scaling is given in brackets. The first column shows the same image with the tube filled with water for three different contrast modalities: (a) attenuation [0, 0.9], (d) differential phase $[-\frac{\pi}{2}, \frac{\pi}{2}]$, (g) dark field [0, 1.0]. The second column shows the same image with the tube filled with pure PVA-microbubbles suspension: (b) attenuation [0, 0.9], (e) differential phase $[-\frac{\pi}{2}, \frac{\pi}{2}]$, (h) dark field [0, 1.0]. The third column shows the subtraction of the image with contrast agent (second column) from the image with water (first column) for the three different contrast modalities: (c) attenuation [0, 0.04], (f) differential phase $[-\frac{\pi}{2}, \frac{\pi}{2}]$, (i) dark field [0, 0.3].

responding transmission subtraction images and the filtered, superimposed signals of the 100 % and 10 % concentration of Solutrast are shown in Figure 4.10. Here, the main contribution to the residual signal in the filtered images, besides the true signal in the tube, is due to movement of the tube and evolving gas in the abdominal area of the mouse.

In the preceding *in vitro* study on clinically established ultrasound microbubbles (see Velroyen et al. (2013) or Section 4.2), the albumin-based Optison (Podell et al., 1999) had been identified as a promising candidate for contrast-enhanced

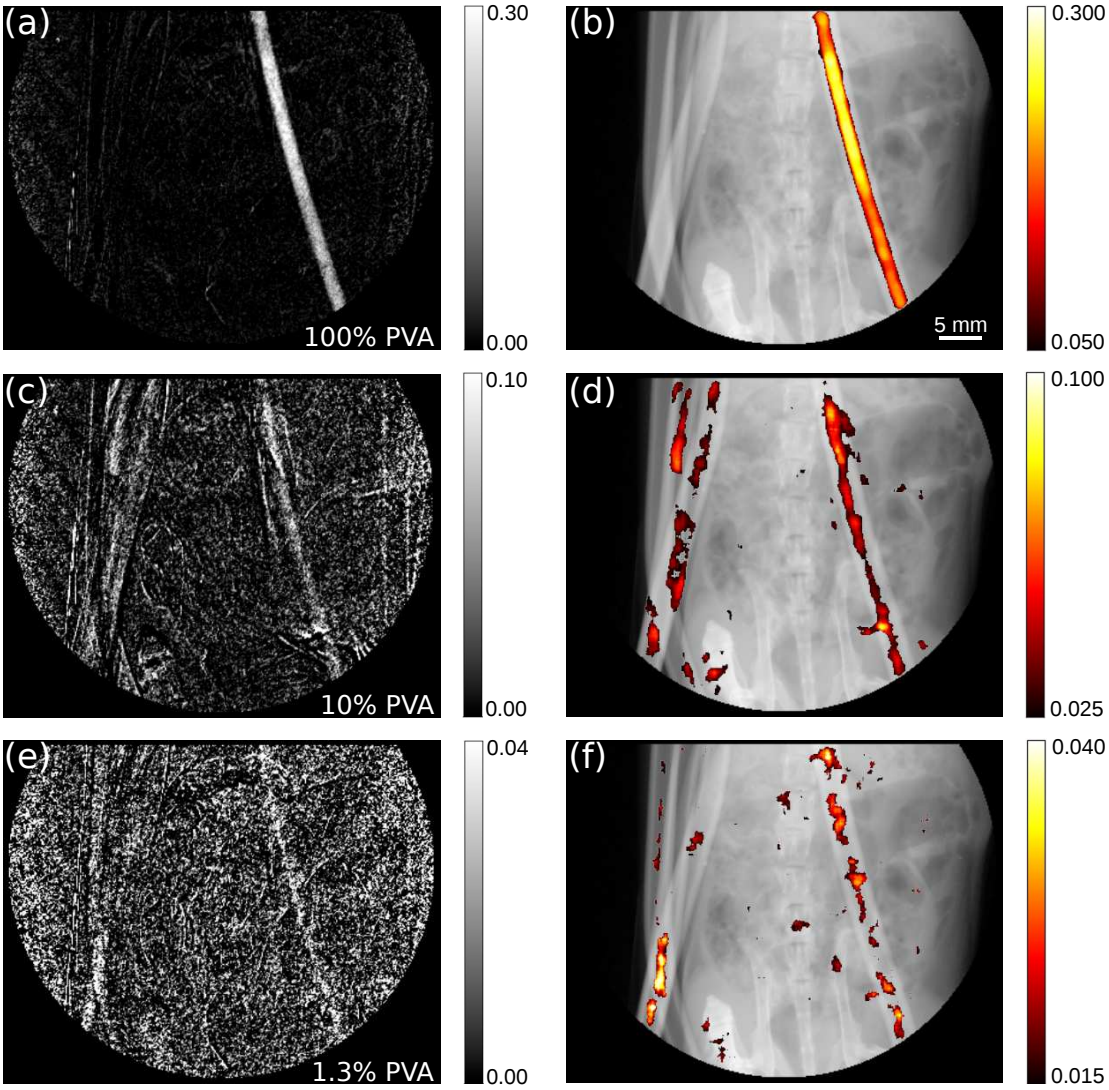

Figure 4.9: Dark-field signal subtraction images (left column) and their threshold-limited, filtered superimposition on the respective original attenuation image (right column, grey values range: [0, 0.9]). (a)-(b) 100 % PVA microbubbles suspension, (c)-(d) 10 % PVA microbubbles suspension, (e)-(f) 1.3 % PVA microbubbles suspension.

dark-field imaging. Unfortunately, a quantitatively reliable comparison between Optison and the PVA bubbles, which would be of strong interest for benchmarking, was not possible, because Optison has been taken off market and is not even available for research-only purposes any more. It is known that microbubbles based on lipid/albumin shells are less stable than polymer-based bubbles (Brismar et al., 2012), and that unfavourable osmotic conditions can effect bubble size or even destroy them (Stolz and Kaps, 2005). The Optison in stock from the

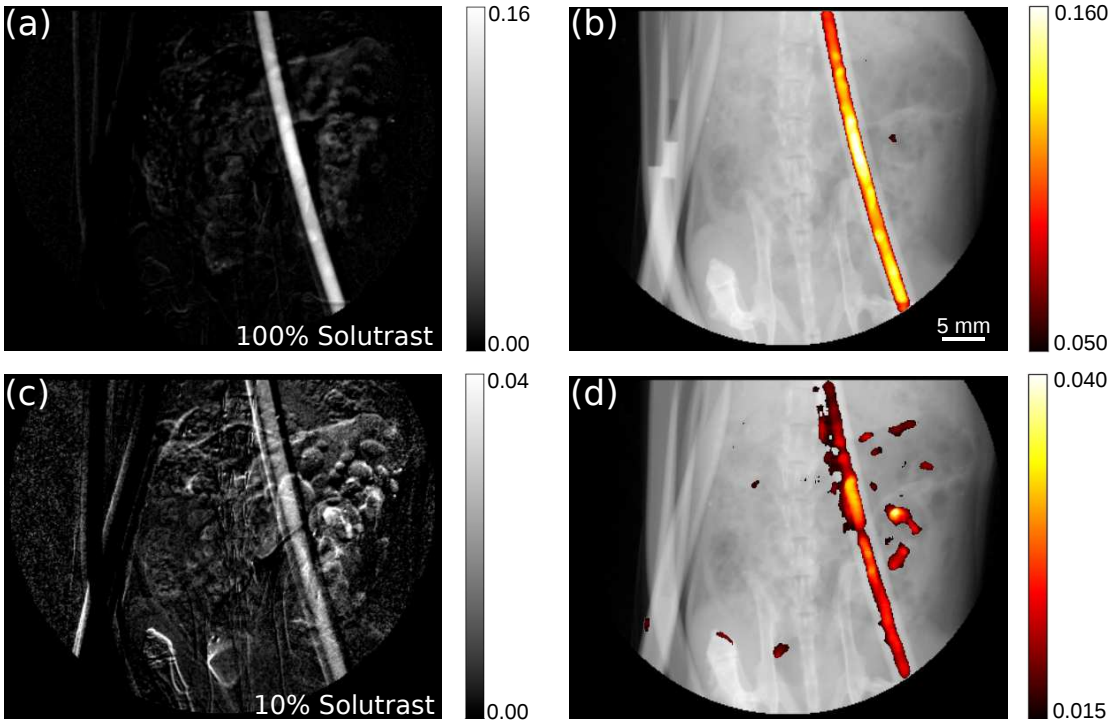

Figure 4.10: Attenuation signal subtraction images (left column) and their threshold-limited, filtered superimposition on the respective original attenuation image (right column, grey values range: [0, 0.9]). (a)-(b) 100 % Solutrast, (c)-(d) 10 % Solutrast.

previous study turned out to have a reduced scattering power and consequently Optison is not included in this study.
Note that the maximum concentration of PVA bubbles presented here is one order of magnitute larger than the concentration that Optison was available at. Concentration along with *in vivo* tolerance is of high importance in terms of contrast agent design for dark-field imaging.
It is interesting to note that the contribution to the scatter signal attributed to the SPION coating of the PVA bubbles, which contains higher-density material, can be assumed to be negligible. Calculations indicate that the amount of magnetite per bubble distributed over the shell is so low that the overall density difference between the shell and the surrounding water is insignificant compared to the density difference between the air filling and the shell. A detailed analysis of the contributions of different shell layers of varying materials is beyond the scope of this purely experimental work and thus will be addressed in a subsequent publication using a wave-optical simulation framework (Malecki et al., 2012) to evaluate different bubble designs based on the underlying physical principles of the dark-field signal (Yashiro et al., 2010; Lynch et al., 2011). Another question

that will be approached in the follow-up work is whether sub-structuring of the shell into more complex nanoclusters—as it is the case for the PVA bubbles used in this work (see Figure 4.11)—can be a reason for the dark-field signal increase.

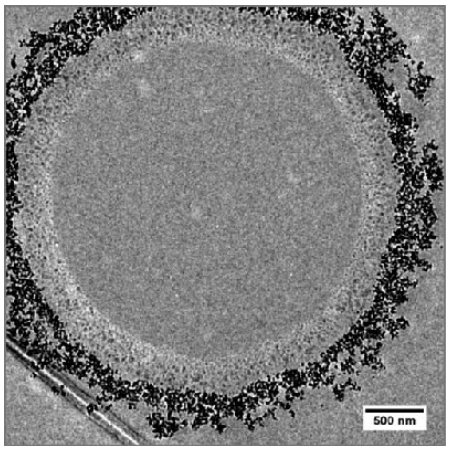

Figure 4.11: Transmission electron microscopy image of a PVA microbubble coated with iron-oxide nanoparticles (black dots), manufactured by Surflay nanotec GmbH, Berlin, Germany. Image courtesy Johan Härmark, School of Technology and Health, KTH Royal Institute of Technology, Sweden.

In this study, no quantitative comparison of absolute values of measured dark-field signals was provided, because measuring a reliable quantitative value of the microbubbles in a vial with round cross section is rendered extremely difficult by the fact that the bubbles float on the surface after already a few seconds if no agitation or fixation is applied. However, fixation was not performed, because it changes the osmotic environment and can consequently lead to (partial) destruction of the bubbles and a change in the signal.
Nevertheless, qualitative conclusions can still be drawn from the measurements: The perfusion-simulation experiments, where the strength of the dark-field signal generated by the coated PVA bubbles was measured in a tube against the noise sources of an ex-vivo animal, support the feasibility of contrast-enhanced dark-field angiography in small animals with adequately designed microbubbles. The PVA microbubbles tested in this work with the given setup are very likely at the edge of detectability when injected into a living animal, depending on the dose tolerance and image acquisition speed. However, they were originally optimized for other imaging modalities such as US, MR, and molecular imaging (Barrefelt et al., 2013; Brismar et al., 2012), and not specifically designed for dark-field imaging, for example in terms of concentration and size. Also, the sensitivity of the setup used in this work is rather low compared to other grating based x-ray imaging setups due to the compactness of the interferometer on the gantry. Using a setup with improved sensitivity, for example by smaller grating periods or higher Talbot

orders, a stronger dark-field signal detectability is expected. The application of alternative measurement schemes, for example fourier-based single-shot image acquisition (Takeda et al., 1982; Bennett et al., 2010), which also provide phase and dark-field information, but with a much shorter acquisition time, may allow for first-pass bolus imaging before the contrast-agent is diluted beyond detectability. It is safe to say that the imaging protocol can be improved in terms of motion artifacts of skeletal structures and the tubes. However, when translated to the *in vivo* situation, breathing and cardiac motion are an additional challenge. Subtraction imaging and adaptive filtering of the signal proved to be helpful tools for improved signal representation, especially for lower doses of contrast agent, and can surely be optimized for example by widely available non-rigid registration algorithms to tackle motion artefacts (Crum et al., 2004; Mani and Arivazhagan, 2013). The presented scans have not been optimized in terms of dose, but the accumulated dose of 5.7 mGy is compatible with repeated *in vivo* studies.

4.3.3 Summary

In this section, it was shown that SPION-coated PVA microbubbles in a small plastic tube generate a sufficiently large dark-field signal in projection imaging in front of a small-animal background to be detected, even when strongly diluted. Therefore, potential of PVA bubbles to be used in dark-field subtraction angiography in small animals is anticipated. Optimized design of the bubbles may further improve the scattering properties.

4.4 Polyvinyl-alcohol bubbles with and without coating

In this study, the question of the influence of the magnetite coating on the PVA bubbles used in Section 4.3 was addressed. The PVA bubbles were measured in a quantitative manner, one batch with magnetite coating and one batch without any coating. The coating was found to have no significant influence on the dark-field signal, but to generate clearly visible attenuation.

4.4.1 Materials and methods

In this study, two contrast agents were tested, namely the PVA bubbles with magnetite coating (DMM150 by Surflay Nanotec GmbH, Berlin, Germany), as

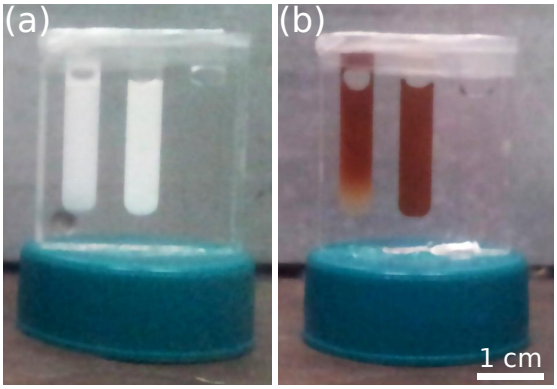

Figure 4.12: Photograph of the phantom made of PMMA, comprising channels with rectangular profiles, filled with different contrast agents. (a) 10 % PVA microbubbles without coating (left), 100 % PVA microbubbles without coating (center), water (right). (b), 10 % PVA microbubbles with magnetite coating (left), 100 % PVA microbubbles with magnetite coating (center), water (right). The water blends in with the PMMA container.

introduced in Section 4.3, and the same type of bubbles without any coating provided by the same manufacturer. The new batch of coated microbubbles had a relative magnetization of 8.74 mg iron per 5×10^9 bubbles. Concentrations of 100 % (5×10^9 bubbles/ml) and 10 % were measured.
The measurements were performed with a phantom made of polymethyl methacrylate (PMMA), which contained three fluid chambers (Figure 4.13). The chambers had rectangular profiles, so that the length of the beam path through the contrast agent can be assumed to be constant 3 mm at at any point in the projection image, neglecting the small cone angle of the beam. The images were acquired with the long axis of the phantom in a horizontal position, so that the bubbles would accumulate in a homogeneously distributed fashion over the whole length of the fluid chamber, rather than at one end of the fluid chamber. The phantom was filled with the 100 % bubbles suspension, the 10 % bubbles suspension, and water as a reference.
Images were acquired at 34 kVp source voltage and approximately 500 µA tube current with 5 steps of 5 seconds exposure per step. The signals were retrieved using the EM algorithm and EADPR correction, described in Chapter 3, Section 3.3.3.2 and 3.3.4, respectively. The average signal strength and standard deviation for the attenuation and dark-field signals were calculated from rectangular regions of interest corresponding to the channels in the phantom, omitting the margins. As a noise reference, the standard deviation of the signal in the two regions between the contrast agent chambers where only PMMA with a constant thickness of 7 mm was in the beam path was calculated. As a non-scattering reference, water was measured within each projection repeatedly, to decouple the

retrieved signal value from slight spectral deviations between different projections.

4.4.2 Results and discussion

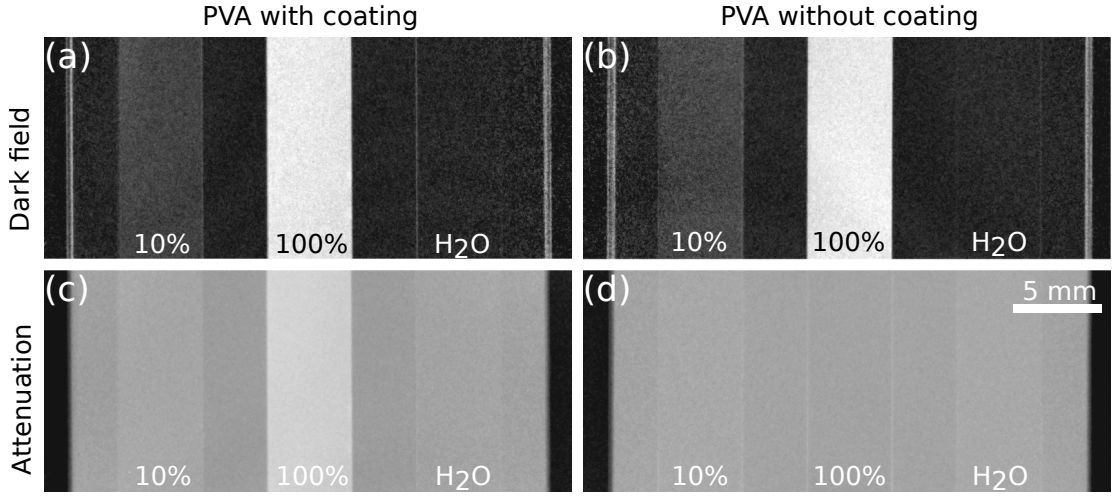

Figure 4.13: Dark-field (top row) and attenuation (bottom row) projection images of a phantom filled with different PVA-bubble contrast agents and water, measured at 34 kVp source voltage. (a), (c) 10 % PVA microbubbles with magetite coating (left), 100 % PVA microbubbles with magnetite coating (center), water (right). (b), (d) 10 % PVA microbubbles without coating (left), 100 % PVA microbubbles without coating (center), water (right). Dark-field images were windowed from 0.0 to 0.7, attenuation images were scaled from 0.0 to 0.4 to represent an appropriate dynamic range for the signal generated by the fully concentrated PVA bubbles.

Figure 4.13 shows the dark-field (top row) and attenuation (bottom row) imaging results for the PVA microbubbles without (left panel) and with (right panel) magnetite coating. Comparing the visual impression of the dark-field signal of the two bubble types, no significant difference is noticeable. Within each type of PVA-bubble contrast agent, the suspension of the full concentration in the central channel scatters a lot stronger than the 10 % suspension in the lefthand channel. The comparison of the two bubble types in the attenuation image reveals that the magnetite coating exhibits a significantly higher absorption of x-rays than the non-coated bubbles. In the attenuation image of the non-coated bubbles, the 100 % suspension exhibits even slightly lower absorption than the water reference because of the substantial amount of air entrapped in the bubbles.

Table 4.2 shows the averaged signal values for dark field $V = V^{\mathrm{s}}/V^{\mathrm{r}}$ (as defined in Section 2.3.3) and transmission $T = \frac{a_0^{\mathrm{s}}}{a_0^{\mathrm{r}}} = I/I_0$ (for definition, see Equation 2.33) and their standard deviations σ_V and σ_T for the two PVA bubble types and water. Additionally, the standard deviation for the noise reference (denoted by

	V	σ_V	CNR_V	T	σ_T	CNR_T
PVAm 100 %	0.37	0.03	19.00	0.627	0.007	16.50
PVAm 10 %	0.86	0.03	2.67	0.707	0.006	3.16
H_2O	0.94	0.03		0.726	0.007	
noise ref		0.03			0.006	
PVA 100 %	0.36	0.02	19.33	0.719	0.005	-0.40
PVA 10 %	0.85	0.04	3.00	0.727	0.007	-2.00
H_2O	0.94	0.03		0.717	0.006	
noise ref		0.03			0.005	

Table 4.2: Signal strength of dark field $V = V^{\mathrm{s}}/V^{\mathrm{r}}$ and transmission $T = \frac{a_0^{\mathrm{s}}}{a_0^{\mathrm{r}}} = I/I_0$ for different PVA-bubble contrast agents (CA). As non-scattering reference, water (H_2O) was measured within each projection repeatedly, to decouple the value from slight spectral deviations between projections. The noise was measured in the flat areas with only PMMA in the beam path, denoted by 'noise ref'. CNR = contrast-to-noise ratio, PVA = polyvinyl-alcohol microbubbles without coating, PVAm = polyvinyl-alcohol microbubbles with magnetite coating.

'noise ref') is given. From those values, the contrast-to-noise ratio (CNR) for the PVA bubble types was calculated via

$$\mathrm{CNR}_V = \frac{V_{\mathrm{H_2O}} - V_{\mathrm{CA}}}{\sigma_{V_{\mathrm{noise\ ref}}}} \tag{4.2}$$

for the dark-field value and analogously for the transmission value. Thereby, the CNR can be understood as a signal-to-noise ratio, where the signal was corrected by an offset defined by the equivalent amount of water in the beam.
The values in the table confirm the visual impression: The dark-field signal in the coated PVA bubbles is equal to the one of the bubbles without coating within the standard deviation for each of the measured concentrations. Thus, also the CNR is approximatly equal with ~ 19 for the 100 % suspension and ~ 3 for the 10 % suspension. The transmission signal of the coated PVA bubbles, however, is significantly lower than the one of the uncoated bubbles for the 100 % suspension (0.627 ± 0.007 vs. 0.719 ± 0.005). The difference decreases with only 10 % concentration (0.707 ± 0.006 vs. 0.727 ± 0.007). The resulting CNRs show a strong contrast for the 100 % suspension of the coated bubbles of 16.5 and a weaker contrast of 3.16 for the respective 10 % suspension. The transmission values of the uncoated bubbles do not significantly deviate from the transmission through the water reference (0.719 ± 0.005 and 0.727 ± 0.007 vs. 0.717 ± 0.006), thus the corresponding CNRs of -0.4 for the full concentration and -2 for the diluted suspension are of little informative value. However, the negative sign indicates an inverse contrast, as the suspensions absorb x-rays less than the water reference.

4.4.3 Summary

The scattering and attenuating behavior of the measured suspensions is in agreement with calculations performed with the wave-optical simulation package of Malecki et al. (2012) by J. Wolf: The computations revealed that the amount of magnetite on the shell of the microbubble as given by the manufacturer does not contribute significantly to the scattering power of the contrast agent suspension (manuscript in preparation). The same statement can be made from the images and quantitative values presented in this section. However, the magnetite coating strongly alters the attenuation signal.

4.5 Summary and conclusions

This chapter comprises three studies on the use of microbubbles as a scattering contrast agent for dark-field radiography. The first study in Section 4.2 showed that a clinically-used ultrasound contrast-agent, Optison, provides dark-field contrast-enhancement measured *in vitro*. A binning series showed superior CNR of dark-field in comparison with the attenuation signal for pixel sizes in the clinically relevant range, exploiting that in dark field structures below the resolution limit of the imaging system generate a signal. The second study, presented in Section 4.3, showed the feasibility of dark-field contrast-enhancement on the small-animal scale, in the presence of scattering background structures like bone and fur. For this study, an experimental PVA-bubble contrast agent was used, because Optison was not available anymore. As the PVA bubbles were coated with magnetite, the last study (Section 4.4) addressed the question about the influence of the coating on the scattering signal: It was found that the amount of magnetite is insignificant for the dark-field signal, but exhibits a measurable x-ray attenuation.

The different studies presented in this chapter lead to the conclusion that microbubble-based contrast agents can be used to successfully generate contrast enhancement in dark-field radiography. On which scale this contrast enhancement can be made use of is an open and complex question.

The results of the study in Section 4.3 show that contrast-enhanced dark-field imaging in small animals such as rats seems not too far fetched. The used experimental contrast agent is tolerated by rats (Barrefelt et al., 2013). However, as the dilution of the injected contrast medium in the blood vessels has to be taken into account, it needs to be evaluated whether the contrast enhancement would still be sufficient, for example for angiographic applications. One can think of several means from the technological and methodological side to improve contrast

enhancement: By using single-shot acquisition approaches (Bennett et al., 2010) and a sufficiently short exposure time, recording an image of the first bolus of the injection, i.e. when the contrast agent is still rather concentrated in the blood vessel, should be possible. Moreover, as already discussed in Section 3.7, the Skyscan 1190 has a rather low sensitivity to refraction and scattering of x-rays. This is very helpful in the case of lung imaging in dark field, as the abundance of air-tissue-interfaces would saturate a more sensitive setup. However, it poses a drawback for the use of microbubbles as contrast agents in dark-field imaging. Thus, the potential of *in vivo* microbubble-based contrast enhancement for small-animal studies should be evaluated more deeply, once a more sensitive and faster setup is available that, in addition, allows for imaging of living animals. The bubbles have not been investigated systematically at other, more sensitive, setups available in the research group, because none of those allow for imaging of the bubbles with a vertical beam path, which is necessary to avoid bubble accumulation at one tip of the containing vial.

Successful contrast enhancement by microbubbles in small-animal dark-field radiography would open up an abundance of applications in preclinical studies, as the bubbles can be designed to accumulate in a targeted manner, for example specifically at tumor tissue (Heppner and Lindner, 2005; Sirsi and Borden, 2009). Also, their versatile applicability could allow for multi-modal imaging in combination with molecular, ultrasound, or magnetic resonance imaging (Brismar et al., 2012; Barrefelt et al., 2013).

Because the hurdle of contrast enhancement in *in vivo* small-animal imaging still needs to be taken, the application of microbubbles for enhanced dark-field contrast in radiography of humans is to be seen in the very far future, if at all. The x-ray energy for human dark-field radiography would need to be considerably higher than the one applied at the Skyscan 1190 to be able to penetrate the body. This comes at the cost of decreased sensitivity, because x-rays of higher energy are refracted by smaller angles than photons of lower energy. Consequently, this does not support the possible use of microbubbles in humans, from the current point of view. The presently still authorized and clinically-established US microbubbles tested in Section 4.2 did not show scattering, which means that efforts would have to be undertaken to either find an authorized agent that scatters sufficiently or to bring a newly designed contrast agent through the certification process.

The strength of the dark-field signal in the context of microbubbles depends on many different parameters (Yashiro et al., 2010; Lynch et al., 2011; Malecki et al., 2012), such as interferometer design, mean x-ray energy, size of the spherical scatterers, number of scattering interfaces in the beam path (i.e. concentration of the agent), and density difference between bubble filling and surrounding medium. As air or a similar gas already provides a strong density difference to blood and tissue,

it is hard to find a better design concept for a dark-field contrast agent than air entrapped in a micro-balloon. To gain a similar electron density difference, one would have to go to elements with high atomic numbers, which usually come at the cost of low biocompatibility or high prices (for example for gold). For instance, although the established iodine-based contrast agents for attenuation-based x-ray imaging have been improved in recent years, they still have a non-negligible toxicity, especially for patients with renal impairment or thyroid dysfunction (Morcos and Thomsen, 2001).

Another important parameter in terms of bubble design is their stability. In that regard, polymer-based bubbles like the tested PVA bubbles are superior over lipid or protein-based shells (Brismar et al., 2012).

The complete biochemical design of a dedicated microbubble-based dark-field contrast-agent is beyond the scope of this thesis and beyond the possibilities of our research laboratory. A future analysis by J. Wolf will focus on systematic wave-optical simulations dedicated to finding optimal bubble design parameters such as size and concentration, appropriate for various setups that are laid out for different design energies. This study may then serve as a guideline for biochemical preclinical and clinical contrast-agent development.

A different concept is the use of pure CO_2 gas for contrast enhancement in blood vessels. In fact, carbon dioxide digital subtraction angiography in attenuation-based imaging is an established clinical procedure, applied in particular to patients whose renal function does not allow for the use of iodinated contrast agents (Selby, 2008). Lundström et al. (2012b,a) introduced CO_2 as a contrast agent for the depiction of small blood vessels in *ex vivo* mice using propagation-based phase-contrast imaging. The differential phase-contrast projection image of the living mouse presented in Section 3.5 showed that air-filled structures show up clearly in the differential phase signal (Figure 3.14). Therefore, it is probable that larger vessels filled with gas could be resolved by the phase signal in the Skyscan 1190, while gas-filled vessels smaller than the resolution limit should show up as scattering structures in the dark-field channel. Consequently, CO_2 gas may be worth evaluating as an alternative contrast agent for phase- and dark-field imaging.

Chapter 5

Summary, conclusions and perspectives

In this chapter, the main results of the work carried out in the context of this thesis are briefly summarized and further steps are pointed out. For an in-depth discussion of the results, also with regard to other existing studies, the reader is referred to the according sections of the results chapters, i.e. Sections 3.7 and 4.5.

Imaging at the small-animal scanner. The methodological work concerning the small-animal phase-contrast and dark-field CT scanner aimed to cope algorithmically with shortcomings of the system and resulting artifacts. In the following, the accomplished solutions within the dedicated processing and reconstruction framework for the data acquired at the Skyscan 1190 are presented. Possible next steps and future solutions are addressed.

- To counteract the rather strong blurring induced by the detector, Richardson-Lucy deconvolution with the measured point spread function was successfully applied to the raw data of a fixated *ex vivo* mouse specimen. Enhanced sharpness was obtained. The deconvolution also increased noise, which could be successfully suppressed by bilateral filtering prior to reconstruction and by regularized statistical iterative reconstruction. The deconvolution can be further optimized by a parallelized implementation to increase processing speed and by the addition of an inherent regularization to selectively enhance edges and not the noise.
- Instabilities of the interferometer due to mechanical and thermal influences cause medium-range Moiré fringes in the images processed with standard algorithms. The fringes were successfully removed by application of an

expectation-maximization–based signal retrieval, which accounts for imprecise stepping and fluctuations in intensity and visibility. As a next step, a parallelized implementation would shorten processing time, which is significantly longer than for the standard algorithms.

- Insufficient correction of medium-range phase variations in the background of an image by ADPR could be overcome by an extension of the algorithm to a more versatile higher-order surface fit onto the sample-free projection areas. By means of a homogeneous sample, the resulting improvement towards more quantitative CT data was demonstrated. A CT with a separate flatfield tomography was shown to be successful only with the extended version of the algorithm.

- A high-performance CT scan of a fixated *ex vivo* mouse specimen demonstrated that superior soft-tissue contrast in the abdominal area is reached with phase-contrast CT, compared to attenuation-based CT. This was facilitated by the advanced correction algorithms and an exchange of the analyzer grating leading to higher visibility of the interferometer.

- The application of regularized statistical iterative reconstruction to the high-performance fixated-mouse scan yielded excellent image quality. Systematic reduction of the number of projections used for reconstruction revealed clear superiority of the iterative approach over simple filtered backprojection for undersampled CT data. However, even with iterative reconstruction, the signal breakdown of the abdominal structures (which do not exhibit large electron density differences) was reached at a number of projections that is still incompatible with scan time constraints posed by anesthesia duration in living animals. The corresponding dose would be compatible with *in vivo* mouse scans. Several technological and methodological optimization measures should be undertaken in the future to improve signal-to-noise ratio in PCCT at the Skyscan 1190 and, consequently, to allow for *in vivo* abdominal PCCT with sufficient contrast. They should aim at increased sensitivity and visibility, shorter exposure times, and faster acquisition schemes, and are discussed more thoroughly in Section 3.7.

The most important scientific milestone reached in the framework of this thesis is the successful performance of dose-compatible *in vivo* phase-contrast and dark-field imaging:

- Trimodal radiographic projection images of a healthy living mouse were presented. They demonstrate clearly complementary information in all three signal channels. Especially, the air-filled airways and the lung are highlighted in the differential phase-contrast and dark-field projections, respec-

tively. Note that it is difficult to image air-filled organs in an *ex vivo* state. This initial observation has triggered several projection-based *in vivo* studies at the Skyscan 1190 on the diagnostic benefit of lung disorders such as emphysema and fibrosis. First promising results have been published, but more, and in particular, longitudinal studies are ongoing, as the potential of dark-field to highlight pulmonary disease models and related structural changes is not yet fully exploited.

- The algorithmic solutions listed above, primarily the statistical iterative reconstruction, have allowed to overcome the scan time limitation posed by the anesthesia duration with regard to thoracic CT. In this work, the first successful dark-field and phase-contrast CT scans of living mice were presented. The lung regions of a healthy mouse, a mouse with emphysema and a mouse with fibrosis were imaged. The dark-field signal shows a strong variation between all three cases, whereas emphysema and control mouse appear very similar in the conventional attenuation CT. Thus, *in vivo* DFCT provides complementary information to the other signal channels. PCCT and conventional CT gave access to equivalent information in this study. These results open up a wide field of preclinical research with DFCT, as further studies on pulmonary diseases are ongoing.

Contrast-enhanced dark-field imaging. The *in vitro* studies on the use of microbubble-based contrast agents for dark-field projection radiography yielded the following results:

- The formerly clinically available ultrasound contrast agent Optison showed scattering of x-rays strong enough to be translated into a dark-field signal measured with Talbot-Lau interferometry at a conventional x-ray source. In general, the CNR of Optison in DF was superior to the CNR in attenuation. Previously, scattering by Optison was only demonstrated in the context of crystal-based diffraction-enhanced imaging and synchrotron radiation.

- The scattering signal caused by microbubbles with diameters in the range of several micrometers was maintained even with pixel sizes in the range used in clinical scanners. In fact, the noise reduction of the DF channel profited more from larger pixels than in attenuation, which resulted in a stronger improvement of the CNR for DF than for attenuation.

- An experimental microbubble contrast agent with PVA shell and iron-oxide coating performed well in DF subtraction imaging for different dilution stages, while using a mouse carcass as source of background noise.

- A quantitative phantom measurement of coated and uncoated PVA bubbles revealed that the coating does not provide a significant change in the dark-field signal.

The conclusion that can be drawn from those studies is that microbubbles can be used to enhance the dark-field signal. However, the signal strength, for example of the PVA agent, in the *in vivo* case in the particular setup used in this thesis is most probably at the edge of detectability due to dilution of the agent in the blood vessel system. The most fundamental aspects that can be optimized in future to reach *in vivo* visibility are:

- a contrast agent with a higher concentration of bubbles that is still tolerated by animals,
- faster acquisition schemes for instant imaging before contrast agent dilution,
- an interferometer that is more sensitive to smaller refraction angles than the one installed in the used setup, e.g. by the use of higher Talbot orders.

The conclusions reached in this thesis contribute to the quest of pushing phase-contrast and dark-field imaging with Talbot-Lau interferometry further towards clinical applicability. In particular, *in vivo* preclinical applicability of radiographic and CT imaging was reached in this work, which was one of the remaining milestones of the translation of the technique from bench to bedside. With that goal accomplished, a wide range of preclinical research is now rendered possible, especially with dark-field imaging. This may help to gain better understanding of diseases and even of therapeutic approaches for those, as longitudinal studies on mouse models are now feasible. Ultimately, the experience gained with the small-animal CT scanner may help to make the transition to a human-size scanner.

Bibliography

S. Allner. *Local Tomography Alignment and Bilateral Filter Post-Processing for Phase-Contrast Imaging*. Master Thesis, Technische Universität München, 2013.
(Referenced on pages 71, 75, 151.)

J. Als-Nielsen and D. McMorrow. *Elements of Modern X-ray Physics*. John Wiley and Sons, Chichester, 2nd edition, 2011. ISBN 9780470973943.
(Referenced on pages 7, 12, 13, 13, 14.)

A. H. Andersen and A. C. Kak. Simultaneous algebraic reconstruction technique (SART): a superior implementation of the ART algorithm. *Ultrasonic Imaging*, 6(1):81–94, 1984.
(Referenced on page 35.)

F. Arfelli, L. Rigon, and R. H. Menk. Microbubbles as x-ray scattering contrast agents using analyzer-based imaging. *Physics in Medicine and Biology*, 55(6): 1643–58, 2010.
(Referenced on page 99.)

A. A. Barrefelt, T. B. Brismar, G. Egri, P. Aspelin, A. Olsson, L. Oddo, S. Margheritelli, K. Caidahl, G. Paradossi, L. Dähne, R. Axelsson, and M. Hassan. Multimodality imaging using SPECT/CT and MRI and ligand functionalized 99mTc-labeled magnetic microbubbles. *EJNMMI Research*, 3(1):1–14, 2013.
(Referenced on pages 99, 99, 117, 122, 123.)

M. Bech. *X-ray Imaging with a Grating Interferometer*. Dissertation, University of Copenhagen, 2009.
(Referenced on pages 2, 11, 15, 25, 28, 36.)

M. Bech, O. Bunk, T. Donath, R. Feidenhans'l, C. David, and F. Pfeiffer. Quantitative x-ray dark-field computed tomography. *Physics in Medicine and Biology*,

55(18):5529–39, 2010.
(Referenced on pages 92, 103.)

M. Bech, A. Tapfer, A. Velroyen, A. Yaroshenko, B. Pauwels, J. Hostens, P. Bruyndonckx, A. Sasov, and F. Pfeiffer. In-vivo dark-field and phase-contrast x-ray imaging. *Scientific Reports*, 3:3209, 2013. doi: 10.1038/srep03209.
(Referenced on pages 48, 98.)

E. E. Bennett, R. Kopace, A. F. Stein, and H. Wen. A grating-based single-shot x-ray phase contrast and diffraction method for in vivo imaging. *Medical Physics*, 37(11):6047–6054, 2010.
(Referenced on pages 48, 79, 96, 118, 123.)

B. Bertrand, F. Estève, H. Elleaume, C. Nemoz, S. Fiedler, A. Bravin, G. Berruyer, T. Brochard, M. Renier, J. Machecourt, W. Thomlinson, and J.-F. Le Bas. Comparison of synchrotron radiation angiography with conventional angiography for the diagnosis of in-stent restenosis after percutaneous transluminal coronary angioplasty. *European Heart Journal*, 26(13):1284–91, 2005.
(Referenced on page 45.)

U. Bonse and M. Hart. An x-ray interferometer. *Applied Physics Letters*, 6(8): 155, 1965.
(Referenced on page 2.)

S. J. Bourke. Interstitial lung disease: progress and problems. *Postgraduate Medical Journal*, 82(970):494–9, 2006.
(Referenced on page 84.)

T. B. Brismar, D. Grishenkov, B. Gustafsson, J. Härmark, A. A. Barrefelt, S. V. V. N. Kothapalli, S. Margheritelli, L. Oddo, K. Caidahl, H. Hebert, and G. Paradossi. Magnetite nanoparticles can be coupled to microbubbles to support multimodal imaging. *Biomacromolecules*, 13(5):1390–1399, 2012.
(Referenced on pages 99, 115, 117, 123, 124.)

W. R. Brody. Digital subtraction angiography. *IEEE Transactions on Nuclear Science*, 29(3):1176–1180, 1982.
(Referenced on page 45.)

F. Cavalieri, A. El Hamassi, E. Chiessi, and G. Paradossi. Stable polymeric microballoons as multifunctional device for biomedical uses: synthesis and characterization. *Langmuir: the ACS Journal of Surfaces and Colloids*, 21(19): 8758–64, 2005.
(Referenced on page 99.)

M. Chabior. *Contributions to the Characterization of Grating-Based X-ray Phase-Contrast Imaging*. Dissertation, Technische Universität Dresden, 2011.
(Referenced on pages 9, 28, 57, 78, 85.)

M. Chabior, T. Donath, C. David, O. Bunk, M. Schuster, C. Schroer, and F. Pfeiffer. Beam hardening effects in grating-based x-ray phase-contrast imaging. *Medical Physics*, 38(3):1189, 2011.
(Referenced on pages 21, 112.)

M. Chabior, M. Schuster, C. Schroer, and F. Pfeiffer. Grating-based phase-contrast computed tomography of thick samples. *Nuclear Instruments and Methods in Physics Research Section A: Accelerators, Spectrometers, Detectors and Associated Equipment*, 693:138–142, 2012.
(Referenced on page 42.)

C. Chantler. Theoretical form factor, attenuation and scattering tabulation for Z=1-92 from E=1-10 eV to E=0.4-1.0 MeV. *J. Phys. Chem. Ref. Data*, 24: 71–643, 1995.
(Referenced on page 11.)

D. Chapman, W. Thomlinson, R. E. Johnston, D. Washburn, E. Pisano, N. Gmür, Z. Zhong, R. Menk, F. Arfelli, and D. Sayers. Diffraction enhanced x-ray imaging. *Physics in Medicine and Biology*, 42(11):2015–25, 1997.
(Referenced on pages 2, 99.)

G.-H. Chen, N. Bevins, J. Zambelli, and Z. Qi. Small-angle scattering computed tomography (SAS-CT) using a Talbot-Lau interferometer and a rotating anode x-ray tube: theory and experiments. *Optics Express*, 18(12):12960–70, 2010. doi: 10.1364/OE.18.012960.
(Referenced on pages 94, 103.)

L. N. Clark and H. C. Dittrich. Cardiac imaging using Optison. *The American Journal of Cardiology*, 86(4):14–18, 2000.
(Referenced on page 98.)

P. Cloetens, W. Ludwig, J. Baruchel, D. Van Dyck, J. Van Landuyt, J. P. Guigay, and M. Schlenker. Holotomography: Quantitative phase tomography with micrometer resolution using hard synchrotron radiation x-rays. *Applied Physics Letters*, 75(19):2912, 1999.
(Referenced on page 2.)

P. Coan, A. Wagner, A. Bravin, P. C. Diemoz, J. Keyriläinen, and J. Mollenhauer. In vivo x-ray phase contrast analyzer-based imaging for longitudinal

osteoarthritis studies in guinea pigs. *Physics in Medicine and Biology*, 55(24): 7649–62, 2010.
(Referenced on page 79.)

J.-M. Correas, L. Bridal, A. Lesavre, A. Méjean, M. Claudon, and O. Hélénon. Ultrasound contrast agents: properties, principles of action, tolerance, and artifacts. *European Radiology*, 11(8):1316–1328, 2001.
(Referenced on page 98.)

G. J. Criner and A. J. Mamary. Lung volume reduction surgery and lung volume reduction in advanced emphysema: who and why? *Seminars in Respiratory and Critical Care Medicine*, 31(3):348–364, 2010.
(Referenced on page 84.)

W. R. Crum, T. Hartkens, and D. L. G. Hill. Non-rigid image registration: theory and practice. *British Journal of Radiology*, 77(2):S140–S153, 2004.
(Referenced on page 118.)

C. David, B. Nohammer, H. H. Solak, and E. Ziegler. Differential x-ray phase contrast imaging using a shearing interferometer. *Applied Physics Letters*, 81 (17):3287, 2002.
(Referenced on page 47.)

T. J. Davis, D. Gao, T. E. Gureyev, A. W. Stevenson, and S. W. Wilkins. Phase-contrast imaging of weakly absorbing materials using hard x-rays. *Nature*, 373: 595–598, 1995.
(Referenced on page 2.)

P. Dawson. X-ray contrast-enhancing agents. *European Journal of Radiology*, 23 (3):172–7, 1996.
(Referenced on page 98.)

N. M. Dempster, A. P. Laird, and D. B. Rubin. Maximum Likelihood from incomplete data via the EM algorithm. *Journal of the Royal Statistical Society. Series B (Methodological)*, 39(1):1–38, 1977.
(Referenced on page 59.)

C. F. Dietrich. *Endosonographie: Lehrbuch und Atlas des endoskopischen Ultraschalls*. Georg Thieme Verlag KG, Stuttgart, 2008. ISBN 9783131456014.
(Referenced on page 98.)

C. B. Do and S. Batzoglou. What is the expectation maximization algorithm? *Nature Biotechnology*, 26(8):897–9, 2008.
(Referenced on page 59.)

T. Donath, F. Pfeiffer, O. Bunk, C. Grünzweig, E. Hempel, S. Popescu, P. Vock, and C. David. Toward clinical x-ray phase-contrast CT: demonstration of enhanced soft-tissue contrast in human specimen. *Investigative Radiology*, 45(7): 445–52, 2010.
(Referenced on pages 48, 91.)

S. Ehn. *Experimental Investigation of the new LAMBDA Detector for X-ray Spectral Phase Contrast*. Diploma Thesis, Technische Universität München, 2013.
(Referenced on page 17.)

M. Engelhardt, J. Baumann, M. Schuster, C. Kottler, F. Pfeiffer, O. Bunk, and C. David. High-resolution differential phase contrast imaging using a magnifying projection geometry with a microfocus x-ray source. *Applied Physics Letters*, 90(22):224101, 2007.
(Referenced on page 29.)

M. Engelhardt, C. Kottler, O. Bunk, C. David, C. Schroer, J. Baumann, M. Schuster, and F. Pfeiffer. The fractional Talbot effect in differential x-ray phase-contrast imaging for extended and polychromatic x-ray sources. *Journal of Microscopy*, 232(1):145–57, 2008.
(Referenced on page 21.)

A. Fehringer, T. Lasser, I. Zanette, P. B. Noël, and F. Pfeiffer. A versatile tomographic forward- and back-projection approach on multi-GPUs. *Proceedings of SPIE Medical Imaging*, page 90344F, 2014. doi: 10.1117/12.2043860.
(Referenced on pages 41, 68, 68.)

L. A. Feldkamp, L. C. Davis, and J. W. Kress. Practical cone-beam algorithm. *Journal of the Optical Society of America A*, 1(6):612–619, 1984.
(Referenced on page 39.)

J. Fessler. Statistical image reconstruction methods for transmission tomography. *Handbook of Medical Imaging Volume 2 Medical Image Processing and Analysis*, pages 1–70, 2000.
(Referenced on pages 43, 70.)

A. A. Fingerle, M. Willner, J. Herzen, D. Münzel, D. Hahn, E. J. Rummeny, P. B. Noël, and F. Pfeiffer. Simulated cystic renal lesions: quantitative x-ray phase-contrast CT – an in vitro phantom study. *Radiology*, 272(3):130876, 2014.
(Referenced on page 48.)

F. Forsberg, C. W. Piccoli, D. A. Merton, J. J. Palazzo, and A. L. Hall. Breast lesions: imaging with contrast-enhanced subharmonic US – initial experience.

Radiology, 244(3):718–26, 2007.
(Referenced on page 98.)

J. W. Goodman. *Introduction to Fourier Optics*. Viva Books Private Limited, New Dehli, 3rd edition, 1996. ISBN 0974707724.
(Referenced on page 15.)

T. Gross and G. Hunninghake. Idiopathic pulmonary fibrosis. *New England Journal of Medicine*, 345(7):517–25, 2001.
(Referenced on page 94.)

D. Hahn. *Statistical Iterative Reconstruction for X-ray Phase-Contrast Computed Tomography*. Dissertation, Technische Universität München, 2014.
(Referenced on pages 42, 43, 43, 55, 58, 58, 68, 68, 69, 70, 85.)

M. Haraguchi, S. Shimura, W. Hida, and K. Shirato. Pulmonary function and regional distribution of emphysema as determined by high-resolution computed tomography. *Respiration; International Review of Thoracic Diseases*, 65(2): 125–9, 1998.
(Referenced on page 87.)

N. Hauser, Z. Wang, R. Kubik-Huch, M. Trippel, G. Singer, M. M. K. Hohl, E. Roessl, T. Köhler, U. van Stevendaal, N. Wieberneit, and M. Stampanoni. A study on mastectomy samples to evaluate breast imaging quality and potential clinical relevance of differential phase contrast mammography. *Investigative Radiology*, 49(3):131–137, 2014.
(Referenced on page 98.)

K. Hellbach, A. Yaroshenko, F. G. Meinel, A. O. Yildirim, T. Conlon, M. Bech, M. Müller, A. Velroyen, M. Notohamiprodjo, F. Bamberg, S. Auweter, M. F. Reiser, O. Eickelberg, and F. Pfeiffer. In vivo dark-field radiography for early pulmonary emphysema diagnosis: quantitative and qualitative analysis. *Submitted*.
(Referenced on pages 83, 96.)

P. Heppner and J. R. Lindner. Contrast ultrasound assessment of angiogenesis by perfusion and molecular imaging. *Expert Review of Molecular Diagnostics*, 5(3):447–55, 2005.
(Referenced on pages 98, 123.)

M. Hermville. *Moire Interferometry at Compact X-Ray Synchrotron Sources*. Diploma Thesis, Technische Universität München, 2013.
(Referenced on page 52.)

J. Herzen, M. S. Willner, A. A. Fingerle, P. B. Noël, T. Köhler, E. Drecoll, E. J. Rummeny, and F. Pfeiffer. Imaging liver lesions using grating-based phase-contrast computed tomography with bi-lateral filter post-processing. *PloS One*, 9(1):e83369, 2014. doi: 10.1371/journal.pone.0083369.
(Referenced on page 48.)

H. Hetterich, M. Willner, S. Fill, J. Herzen, F. Bamberg, A. Hipp, U. Schüller, S. Adam-Neumair, S. Wirth, M. Reiser, F. Pfeiffer, and T. Saam. Phase-contrast CT: qualitative and quantitative evaluation of atherosclerotic carotid artery plaque. *Radiology*, 271(3):870–8, 2014.
(Referenced on page 48.)

J. Hsieh. *Computed Tomography - Principles, Design, Artifacts, and Recent Advances*. SPIE and John Wiley & Sons, Inc., Bellingham, 2nd edition, 2009.
(Referenced on pages 41, 42, 42, 43, 43.)

P. J. Huber. Robust estimation of a location parameter. *The Annals of Mathematical Statistics*, 35(1):73–101, 1964.
(Referenced on page 70.)

P. M. Joseph. An improved algorithm for reprojecting rays through pixel images. *IEEE Transactions on Medical Imaging*, 1(3):192–196, 1982.
(Referenced on page 69.)

A. C. Kak and M. Slaney. *Principles of Computerized Tomographic Imaging*. Society for Industrial and Applied Mathematics, Philadelphia, 2001. ISBN 978-0-89871-494-4.
(Referenced on pages 30, 31, 32, 33, 37, 39, 39, 42, 43, 68.)

T. E. King. Clinical advances in the diagnosis and therapy of the interstitial lung diseases. *American Journal of Respiratory and Critical Care Medicine*, 172(3): 268–79, 2005.
(Referenced on pages 84, 84.)

G. Knoll. *Radiation Detection and Measurement*. Wiley, Phoenix, 2010. ISBN 9780470131480.
(Referenced on page 18.)

T. Koehler, G. Martens, U. van Stevendaal, and E. Roessl. Non-scatter contributions to the dark-field signal in differential phase contrast imaging. *Proceedings of International Workshop on X-ray and Neutron Phase Imaging with Gratings*, pages 205–210, 2012.
(Referenced on page 73.)

P. Kogan, R. Gessner, and P. A. Dayton. Microbubbles in imaging: applications beyond ultrasound. *Bubble Science Engineering Technology*, 2(1):3–8, 2010.
(Referenced on page 99.)

E. Lau. Beugungserscheinungen an Doppelrastern. *Annalen der Physik*, 437(7-8): 417–423, 1948.
(Referenced on page 23.)

J. Ley-Zaporozhan, S. Ley, and H.-U. Kauczor. Morphological and functional imaging in COPD with CT and MRI: present and future. *European Radiology*, 18(3):510–21, 2008.
(Referenced on page 83.)

J. R. Lindner, J. Song, A. R. Jayaweera, J. Sklenar, and S. Kaul. Microvascular rheology of Definity microbubbles after intra-arterial and intravenous administration. *Journal of the American Society of Echocardiography*, 15(5):396–403, 2002.
(Referenced on page 98.)

A. W. Lohmann, H. Knuppertz, and J. Jahns. Fractional Montgomery effect: a self-imaging phenomenon. *Journal of the Optical Society of America A*, 22(8): 1500, 2005.
(Referenced on page 20.)

L. B. Lucy. An iterative technique for the rectification of observed distributions. *The Astronomical Journal*, 79:745, 1974.
(Referenced on page 55.)

U. Lundström, D. H. Larsson, A. Burvall, L. Scott, U. K. Westermark, M. Wilhelm, M. Arsenian Henriksson, and H. M. Hertz. X-ray phase-contrast CO_2 angiography for sub-10 μm vessel imaging. *Physics in Medicine and Biology*, 57(22):7431–41, 2012a.
(Referenced on page 124.)

U. Lundström, D. H. Larsson, A. Burvall, P. A. Takman, L. Scott, H. Brismar, and H. M. Hertz. X-ray phase contrast for CO_2 microangiography. *Physics in Medicine and Biology*, 57(9):2603–17, 2012b.
(Referenced on page 124.)

H. Lusic and M. W. Grinstaff. X-ray computed tomography contrast agents. *Chemical Reviews*, 113(3):1641–66, 2013.
(Referenced on pages 44, 45.)

S. K. Lynch, V. Pai, J. Auxier, A. F. Stein, E. E. Bennett, C. K. Kemble, X. Xiao, W.-K. Lee, N. Y. Morgan, and H. H. Wen. Interpretation of dark-field contrast and particle-size selectivity in grating interferometers. *Applied Optics*, 50(22): 4310–9, 2011.
(Referenced on pages 94, 103, 116, 123.)

M. Mahmoudi, S. Sant, B. Wang, S. Laurent, and T. Sen. Superparamagnetic iron oxide nanoparticles (SPIONs): development, surface modification and applications in chemotherapy. *Advanced Drug Delivery Reviews*, 63(1-2):24–46, 2011.
(Referenced on page 99.)

A. Malecki, G. Potdevin, and F. Pfeiffer. Quantitative wave-optical numerical analysis of the dark-field signal in grating-based x-ray interferometry. *Europhysics Letters*, 99(4):48001, 2012.
(Referenced on pages 15, 104, 116, 122, 123.)

V. Mani and S. Arivazhagan. A survey of medical image registration. *Journal of Biomedical Engineering and Technology*, 1(2):8–25, 2013.
(Referenced on page 118.)

E. H. Meijering, W. J. Niessen, and M. A. Viergever. Retrospective motion correction in digital subtraction angiography: a review. *IEEE Transactions on Medical Imaging*, 18(1):2–21, 1999.
(Referenced on page 45.)

F. G. Meinel, F. Schwab, A. Yaroshenko, A. Velroyen, M. Bech, K. Hellbach, J. Fuchs, T. Stiewe, A. O. Yildirim, F. Bamberg, M. F. Reiser, F. Pfeiffer, and K. Nikolaou. Lung tumors on multimodal radiographs derived from grating-based x-ray imaging – a feasibility study. *Physica Medica: European Journal of Medical Physics*, 30(3):352–7, 2014a.
(Referenced on page 96.)

F. G. Meinel, A. Yaroshenko, K. Hellbach, M. Bech, M. Müller, A. Velroyen, F. Bamberg, O. Eickelberg, K. Nikolaou, M. F. Reiser, F. Pfeiffer, and A. O. Yildirim. Improved diagnosis of pulmonary emphysema using in vivo dark-field radiography. *Investigative Radiology*, 49(10):653–658, 2014b.
(Referenced on pages 83, 94, 96.)

J. Meiser, M. Amberger, M. Willner, D. Kunka, P. Meyer, F. Koch, A. Hipp, M. Walter, F. Pfeiffer, and J. Mohr. Increasing the field of view of x-ray phase contrast imaging using stitched gratings on low absorbent carriers. 01:903355,

2014. doi: 10.1117/12.2043479.
(Referenced on pages 48, 98.)

T. Michel, J. Rieger, G. Anton, F. Bayer, M. W. Beckmann, J. Durst, P. A. Fasching, W. Haas, A. Hartmann, G. Pelzer, M. Radicke, C. Rauh, A. Ritter, P. Sievers, R. Schulz-Wendtland, M. Uder, D. L. Wachter, T. Weber, E. Wenkel, and A. Zang. On a dark-field signal generated by micrometer-sized calcifications in phase-contrast mammography. *Physics in Medicine and Biology*, 58(8):2713–32, 2013.
(Referenced on page 98.)

T. P. Millard, M. Endrizzi, L. Rigon, F. Arfelli, R. H. Menk, J. Owen, E. Stride, and A. Olivo. Quantification of microbubble concentration through x-ray phase contrast imaging. *Applied Physics Letters*, 103(11):114105, 2013.
(Referenced on page 99.)

A. Momose. Phase-sensitive imaging and phase tomography using X-ray interferometers. *Optics Express*, 11(19):2303–14, 2003. doi: 10.1364/OE.11.002303.
(Referenced on page 2.)

A. Momose. Recent advances in x-ray phase imaging. *Japanese Journal of Applied Physics*, 44(9A):6355–6367, 2005.
(Referenced on page 47.)

A. Momose, S. Kawamoto, I. Koyama, Y. Hamaishi, K. Takai, and Y. Suzuki. Demonstration of x-ray talbot interferometry. *Japanese Journal of Applied Physics*, 42(Part 2, No. 7B):L866–L868, 2003.
(Referenced on page 47.)

A. Momose, W. Yashiro, Y. Takeda, Y. Suzuki, and T. Hattori. Phase tomography by x-ray Talbot interferometry for biological imaging. *Japanese Journal of Applied Physics*, 45(6A):5254–5262, 2006.
(Referenced on page 48.)

W. D. Montgomery. Self-imaging objects of infinite aperture. *Journal of the Optical Society of America*, 57(6):772, 1967.
(Referenced on page 20.)

S. Morcos and H. Thomsen. Adverse reactions to iodinated contrast media. *European Radiology*, 11(7):1267–75, 2001.
(Referenced on pages 44, 124.)

K. E. Morgan, J. S. Allen, P. a. Dayton, J. E. Chomas, a. L. Klibaov, and K. W. Ferrara. Experimental and theoretical evaluation of microbubble behavior: effect of transmitted phase and bubble size. *IEEE Transactions on Ultrasonics, Ferroelectrics, and Frequency Control*, 47(6):1494–509, 2000.
(Referenced on page 98.)

K. Müller. *Fast and Accurate Three-Dimensional Reconstruction from Cone-Beam Projection Data Using Algebraic Methods*. Dissertation, Ohio State University, 1998.
(Referenced on page 34.)

K. Müller, R. Yagel, and J. J. Wheller. Fast and accurate projection algorithm for 3D cone-beam reconstruction with the Algebraic Reconstruction Technique (ART). 3336(1):724–732, 1998.
(Referenced on page 69.)

M. Müller. *Experimental Characterization of the first Preclinical X-ray Phase-Contrast CT Scanner*. Diploma Thesis, Technische Universität München, 2013.
(Referenced on pages 53, 53, 53, 78.)

S. Namasivayam, M. K. Kalra, W. E. Torres, and W. C. Small. Adverse reactions to intravenous iodinated contrast media: a primer for radiologists. *Emergency Radiology*, 12(5):210–5, 2006.
(Referenced on page 44.)

M. B. Nielsen and N. Bang. Contrast enhanced ultrasound in liver imaging. *European Journal of Radiology*, 51 Suppl:S3–8, 2004.
(Referenced on page 98.)

P. B. Noël, A. A. Fingerle, B. Renger, D. Münzel, E. J. Rummeny, and M. Dobritz. Initial performance characterization of a clinical noise-suppressing reconstruction algorithm for MDCT. *American Journal of Roentgenology*, 197(6):1404–1409, 2011.
(Referenced on page 68.)

P. B. Noël, B. Renger, M. Fiebich, D. Münzel, A. A. Fingerle, E. J. Rummeny, and M. Dobritz. Does iterative reconstruction lower CT radiation dose: evaluation of 15,000 examinations. *PloS One*, 8(11):e81141, 2013. doi: 10.1371/journal.pone.0081141.
(Referenced on page 68.)

J. Nuyts, B. De Man, J. A. Fessler, W. Zbijewski, and F. J. Beekman. Modelling the physics in the iterative reconstruction for transmission computed tomogra-

phy. *Physics in Medicine and Biology*, 58(12):R63–96, 2013.
(Referenced on page 43.)

D. M. Paganin. *Coherent X-Ray Optics*. Oxford University Press, Oxford, 2006. ISBN 9780198567288.
(Referenced on pages 11, 11, 11.)

G. Paradossi, P. Pellegretti, and A. Trucco. *Ultrasound Contrast Agents: Targeting and Processing Methods for Theranostics*. Springer, Milan, 2010. ISBN 8847014948.
(Referenced on page 99.)

D. W. Parsons, K. Morgan, M. Donnelley, A. Fouras, J. Crosbie, I. Williams, R. C. Boucher, K. Uesugi, N. Yagi, and K. K. W. Siu. High-resolution visualization of airspace structures in intact mice via synchrotron phase-contrast x-ray imaging (PCXI). *Journal of Anatomy*, 213(2):217–227, 2008.
(Referenced on page 79.)

J. J. Pasternak and E. E. Williamson. Clinical pharmacology, uses, and adverse reactions of iodinated contrast agents: a primer for the non-radiologist. *Mayo Clinic Proceedings*, 87(4):390–402, 2012. doi: 10.1016/j.mayocp.2012.01.012.
(Referenced on pages 44, 44.)

F. Pfeiffer, T. Weitkamp, O. Bunk, and C. David. Phase retrieval and differential phase-contrast imaging with low-brilliance x-ray sources. *Nature Physics*, 2(4): 258–261, 2006.
(Referenced on pages 23, 48.)

F. Pfeiffer, O. Bunk, C. David, M. Bech, G. Le Duc, A. Bravin, and P. Cloetens. High-resolution brain tumor visualization using three-dimensional x-ray phase contrast tomography. *Physics in Medicine and Biology*, 52(23):6923–30, 2007a.
(Referenced on pages 2, 48.)

F. Pfeiffer, C. Kottler, O. Bunk, and C. David. Hard x-ray phase tomography with low-brilliance sources. *Physical Review Letters*, 98(10):1–4, 2007b.
(Referenced on pages 36, 48.)

F. Pfeiffer, M. Bech, O. Bunk, P. Kraft, E. F. Eikenberry, C. Brönnimann, C. Grünzweig, and C. David. Hard-x-ray dark-field imaging using a grating interferometer. *Nature Materials*, 7(2):134–7, 2008.
(Referenced on pages 2, 47, 48.)

S. Podell, C. Burrascano, M. Gaal, B. Golec, J. Maniquis, and P. Mehlhaff. Physical and biochemical stability of Optison, an injectable ultrasound contrast agent. *Biotechnology and Applied Biochemistry*, 30(3):213–223, 1999.
(Referenced on page 114.)

G. Potdevin, A. Malecki, T. Biernath, M. Bech, T. H. Jensen, R. Feidenhans'l, I. Zanette, T. Weitkamp, J. Kenntner, J. Mohr, P. Roschger, M. Kerschnitzki, W. Wagermaier, K. Klaushofer, P. Fratzl, and F. Pfeiffer. X-ray vector radiography for bone micro-architecture diagnostics. *Physics in Medicine and Biology*, 57(11):3451–61, 2012.
(Referenced on pages 94, 98.)

Z. Qi and G.-H. Chen. Direct fan-beam reconstruction algorithm via filtered backprojection for differential phase-contrast computed tomography. *X-Ray Optics and Instrumentation*, 2008:1–8, 2008.
(Referenced on page 42.)

J. Radon. On the determination of functions from their integrals along certain manifolds. *Berichte über die Verhandlungen der Sächsischen Akademie der Wissenschaften*, 69:262–277, 1917.
(Referenced on page 30.)

R. Raupach and T. Flohr. Performance evaluation of x-ray differential phase contrast computed tomography (PCT) with respect to medical imaging. *Medical Physics*, 39(8):4761–74, 2012.
(Referenced on pages 75, 85.)

R. Raupach and T. G. Flohr. Analytical evaluation of the signal and noise propagation in x-ray differential phase-contrast computed tomography. *Physics in Medicine and Biology*, 56(7):2219–44, 2011.
(Referenced on pages 75, 85.)

W. H. Richardson. Bayesian-based iterative method of image restoration. *Journal of the Optical Society of America*, 62(1):55, 1972.
(Referenced on page 55.)

S. J. Riederer and C. A. Mistretta. Selective iodine imaging using K-edge energies in computerized x-ray tomography. *Medical Physics*, 4(6):474, 1977.
(Referenced on page 45.)

S.-J. Rim, H. Leong-Poi, J. R. Lindner, D. Couture, D. Ellegala, H. Mason, M. Durieux, N. F. Kassel, and S. Kaul. Quantification of cerebral perfusion with "real-time" contrast-enhanced ultrasound. *Circulation*, 104(21):2582–87,

2001.
(Referenced on page 98.)

E. Roessl, H. Daerr, T. Koehler, G. Martens, and U. van Stevendaal. Clinical boundary conditions for grating-based differential phase-contrast mammography. *Philosophical Transactions of the Royal Society*, 372, 2014.
(Referenced on page 98.)

S. Schleede. *X-Ray Phase-Contrast Imaging at a Compact Laser-Driven Synchrotron Source*. Dissertation, Technische Universität München, 2013.
(Referenced on pages 15, 74.)

S. Schleede, F. G. Meinel, M. Bech, J. Herzen, K. Achterhold, G. Potdevin, A. Malecki, S. Adam-Neumair, S. F. Thieme, F. Bamberg, K. Nikolaou, A. Bohla, A. O. Yildirim, R. Loewen, M. Gifford, R. Ruth, O. Eickelberg, M. Reiser, and F. Pfeiffer. Emphysema diagnosis using x-ray dark-field imaging at a laser-driven compact synchrotron light source. *Proceedings of the National Academy of Sciences of the United States of America*, 109(44):17880–5, 2012.
(Referenced on pages 48, 83, 94, 98.)

J. P. Schlomka, E. Roessl, R. Dorscheid, S. Dill, G. Martens, T. Istel, C. Bäumer, C. Herrmann, R. Steadman, G. Zeitler, A. Livne, and R. Proksa. Experimental feasibility of multi-energy photon-counting K-edge imaging in pre-clinical computed tomography. *Physics in Medicine and Biology*, 53(15):4031–47, 2008.
(Referenced on page 45.)

M. Schneider. SonoVue, a new ultrasound contrast agent. *European Radiology*, 9 (S3):S347–8, 1999.
(Referenced on pages 100, 100.)

M. Schneider, M. Arditi, M. Barrau, J. Brochot, A. Broillet, R. Ventrone, and F. Yan. BR1: a new ultrasonographic contrast agent based on sulfur hexafluoride-filled microbubbles. *Investigative Radiology*, 30(8):451–7, 1995.
(Referenced on page 103.)

G. Schulz, T. Weitkamp, I. Zanette, F. Pfeiffer, F. Beckmann, C. David, S. Rutishauser, E. Reznikova, and B. Müller. High-resolution tomographic imaging of a human cerebellum: comparison of absorption and grating-based phase contrast. *Journal of the Royal Society*, 7(53):1665–76, 2010.
(Referenced on page 48.)

J. B. Selby. Carbon dioxide angiography, principles, techniques, and practices. 191(5):W211–W211, 2008.
(Referenced on pages 44, 124.)

R. L. Siddon. Calculation of the radiological depth. *Medical Physics*, 12(1):84, 1985.
(Referenced on page 69.)

S. Sirsi and M. Borden. Microbubble compositions, properties and biomedical applications. *Bubble Science Engineering and Technology*, 1(1-2):3–17, 2009.
(Referenced on pages 99, 123.)

K. K. W. Siu, K. S. Morgan, D. M. Paganin, R. Boucher, K. Uesugi, N. Yagi, and D. W. Parsons. Phase contrast x-ray imaging for the non-invasive detection of airway surfaces and lumen characteristics in mouse models of airway disease. *European Journal of Radiology*, 68(3 Suppl):S22–6, 2008.
(Referenced on page 79.)

G. E. Smith. The invention and early history of the CCD. *Nuclear Instruments and Methods in Physics Research, Section A: Accelerators, Spectrometers, Detectors and Associated Equipment*, 607(1):1–6, 2009.
(Referenced on page 17.)

A. Snigirev, I. Snigireva, V. Kohn, S. Kuznetsov, and I. Schelokov. On the possibilities of x-ray phase contrast microimaging by coherent high-energy synchrotron radiation. *Review of Scientific Instruments*, 66(12):5486, 1995.
(Referenced on page 2.)

M. Stampanoni, Z. Wang, T. Thüring, C. David, E. Roessl, M. Trippel, R. A. Kubik-Huch, G. Singer, M. K. Hohl, and N. Hauser. The first analysis and clinical evaluation of native breast tissue using differential phase-contrast mammography. *Investigative Radiology*, 46(12):801–6, 2011.
(Referenced on page 48.)

A. Stanton and W. C. Röntgen. Über eine neue Art von Strahlen. *Sitzungsberichte der Würzburger Physik.-medic. Gesellschaft*, 1895.
(Referenced on page 7.)

E. P. Stolz and M. Kaps. Ultrasound contrast agents and imaging of cerebrovascular disease. *Seminars in Cerebrovascular Diseases and Stroke*, 5(2):111–131, 2005.
(Referenced on page 115.)

M. Strauss, I. Naday, I. Sherman, M. Kraimer, E. Westbrook, and N. Zaluzec. CCD sensors in synchrotron x-ray detectors. *Nuclear Instruments and Methods in Physics Research. Section A, Accelerators, Spectrometers, Detectors and Associated Equipment*, 19(17):563–577, 1988.
(Referenced on page 17.)

D. Stutman, T. J. Beck, J. A. Carrino, and C. O. Bingham. Talbot phase-contrast x-ray imaging for the small joints of the hand. *Physics in Medicine and Biology*, 56(17):5697—-720, 2011.
(Referenced on page 48.)

A. Sztrókay, J. Herzen, S. D. Auweter, S. Liebhardt, D. Mayr, M. Willner, D. Hahn, I. Zanette, T. Weitkamp, K. Hellerhoff, F. Pfeiffer, M. F. Reiser, and F. Bamberg. Assessment of grating-based x-ray phase-contrast CT for differentiation of invasive ductal carcinoma and ductal carcinoma in situ in an experimental ex vivo set-up. *European Radiology*, 23(2):381–7, 2013.
(Referenced on page 48.)

M. Takeda, H. Ina, and S. Kobayashi. Fourier-transform method of fringe-pattern analysis for computer-based topography and interferometry. *Journal of the Optical Society of America*, 72(1):156, 1982.
(Referenced on page 118.)

T. Takeda, A. Yoneyama, J. Wu, Thet-Thet-Lwin, A. Momose, and K. Hyodo. In vivo physiological saline-infused hepatic vessel imaging using a two-crystal-interferometer-based phase-contrast x-ray technique. *Journal of Synchrotron Radiation*, 19(Pt 2):252–6, 2012.
(Referenced on page 79.)

H. F. Talbot. Facts relating to optical science. *The London and Edinburgh Philosophical Magazine and Journal of Science*, 9(56):401–407, 1836.
(Referenced on page 19.)

R. Tang, Y. Xi, W.-M. Chai, Y. Wang, Y. Guan, G.-Y. Yang, H. Xie, and K.-M. Chen. Microbubble-based synchrotron radiation phase contrast imaging: basic study and angiography applications. *Physics in Medicine and Biology*, 56(12): 3503–12, 2011.
(Referenced on pages 79, 99.)

A. Tapfer. *Small Animal X-ray Phase-Contrast Imaging*. Dissertation, Technische Universität München, 2013.
(Referenced on pages 3, 3, 10, 11, 16, 21, 22, 24, 48, 49, 49, 50, 62, 62, 66, 73, 94.)

A. Tapfer, M. Bech, B. Pauwels, X. Liu, P. Bruyndonckx, A. Sasov, J. Kenntner, J. Mohr, M. Walter, J. Schulz, and F. Pfeiffer. Development of a prototype gantry system for pre-clinical x-ray phase-contrast computed tomography. *Medical Physics*, 38(11):5910–15, 2011.
(Referenced on page 48.)

A. Tapfer, M. Bech, A. Velroyen, J. Meiser, J. Mohr, M. Walter, J. Schulz, B. Pauwels, P. Bruyndonckx, X. Liu, A. Sasov, and F. Pfeiffer. Experimental results from a preclinical x-ray phase-contrast CT scanner. *Proceedings of the National Academy of Sciences of the United States of America*, 109(39): 15691–6, 2012.
(Referenced on pages 48, 84, 98.)

A. Tapfer, R. Braren, M. Bech, M. Willner, I. Zanette, T. Weitkamp, M. Trajkovic-Arsic, J. T. Siveke, M. Settles, M. Aichler, A. Walch, and F. Pfeiffer. X-ray phase-contrast CT of a pancreatic ductal adenocarcinoma mouse model. *PloS One*, 8(3):e58439, 2013. doi: 10.1371/journal.pone.0058439.
(Referenced on pages 71, 95.)

A. Tapfer, M. Bech, I. Zanette, P. Symvoulidis, S. Stangl, G. Multhoff, M. Molls, V. Ntziachristos, and F. Pfeiffer. Three-dimensional imaging of whole mouse models: comparing nondestructive x-ray phase-contrast micro-CT with cryotome-based planar epi-illumination imaging. *Journal of Microscopy*, 253 (1):24–30, 2014.
(Referenced on pages 71, 95.)

A. C. Thompson, editor. *X-ray Data Booklet*. Center for X-ray optics and advanced light source, Lawrence Berkeley National Laboratory, University of California, Berkeley, 3rd edition, 2009.
(Referenced on page 45.)

T. Thüring, P. Modregger, T. Grund, J. Kenntner, C. David, and M. Stampanoni. High resolution, large field of view x-ray differential phase contrast imaging on a compact setup. *Applied Physics Letters*, 99(4):041111, 2011a.
(Referenced on pages 29, 95, 98, 110.)

T. Thüring, P. Modregger, B. R. Pinzer, Z. Wang, and M. Stampanoni. Non-linear regularized phase retrieval for unidirectional x-ray differential phase contrast radiography. *Optics Express*, 19(25):25545–58, 2011b. doi: 10.1364/OE.19.025545.
(Referenced on pages 74, 150.)

S. Tilley, J. H. Siewerdsen, and J. W. Stayman. Iterative CT reconstruction using models of source and detector blur and correlated noise. *The Third International Conference on Image Formation in X-ray Computed Tomography*, pages 363–367, 2014.
(Referenced on page 75.)

H. Turbell. *Cone-Beam Reconstruction Using Filtered Backprojection*. Dissertation, Linköpings Universitet, 2001.
(Referenced on pages 38, 39.)

U. van Stevendaal, Z. Wang, T. Köhler, G. Martens, M. Stampanoni, and E. Roessl. Reconstruction method incorporating the object-position dependence of visibility loss in dark-field imaging. *Proceedings of SPIE Medical Imaging*, page 86680Z, 2013. doi: 10.1117/12.2006711.
(Referenced on page 42.)

A. Velroyen, M. Bech, A. Tapfer, A. Yaroshenko, M. Müller, P. Paprottka, M. Ingrisch, C. C. Clemens, S. D. Auweter, M. F. Reiser, and F. Pfeiffer. Ex-vivo perfusion-simulation measurements of microbubbles as a scattering contrast agent for grating-based x-ray dark-field imaging. *Submitted*, a.
(Referenced on page 99.)

A. Velroyen, A. Yaroshenko, D. Hahn, A. Fehringer, A. Tapfer, M. Müller, P. B. Noël, B. Pauwels, A. Sasov, A. O. Yildirim, O. Eickelberg, K. Hellbach, S. D. Auweter, F. G. Meinel, M. F. Reiser, M. Bech, and F. Pfeiffer. X-Ray Dark-Field Computed Tomography of Living Mice. *Submitted*, b.
(Referenced on pages 48, 98.)

A. Velroyen, M. Bech, A. Malecki, A. Tapfer, A. Yaroshenko, M. Ingrisch, C. C. Cyran, S. D. Auweter, K. Nikolaou, M. Reiser, and F. Pfeiffer. Microbubbles as a scattering contrast agent for grating-based x-ray dark-field imaging. *Physics in Medicine and Biology*, 58(4):N37–46, 2013.
(Referenced on pages 99, 114.)

G. R. Washko. Diagnostic imaging in COPD. *Seminars in Respiratory and Critical Care Medicine*, 31(3):276–285, 2010.
(Referenced on pages 84, 84.)

G. R. Washko, E. Hoffman, and J. J. Reilly. Radiographic evaluation of the potential lung volume reduction surgery candidate. *Proceedings of the American Thoracic Society*, 5(4):421–6, 2008.
(Referenced on pages 84, 94.)

S. Weinberg. *The Quantum Theory of Fields, Volume I: Foundations*. Cambridge University Press, Cambridge, 1995. ISBN 0521670535.
(Referenced on page 9.)

T. Weitkamp, A. Diaz, B. Nohammer, F. Pfeiffer, M. Stampanoni, E. Ziegler, and C. David. Moiré interferometry formulas for hard x-ray wavefront sensing.

Proceedings of SPIE, 5533:140–144, 2004. doi: 10.1117/12.559695.
(Referenced on page 52.)

T. Weitkamp, A. Diaz, C. David, F. Pfeiffer, M. Stampanoni, P. Cloetens, and E. Ziegler. X-ray phase imaging with a grating interferometer. *Optics Express*, 13(16):6296–304, 2005. doi: 10.1364/OPEX.13.006296.
(Referenced on pages 2, 25, 47.)

T. Weitkamp, C. David, C. Kottler, O. Bunk, and F. Pfeiffer. Tomography with grating interferometers at low-brilliance sources. *Proceedings of SPIE*, 6318: 1–10, 2006. doi: 10.1117/12.683851.
(Referenced on pages 19, 23.)

P. Willmott. *An Introduction to Synchrotron Radiation: Techniques and Applications*. John Wiley and Sons, Chichester, 1st edition, 2011. ISBN 9780470745786.
(Referenced on pages 7, 15, 17, 17.)

M. Willner, M. Bech, J. Herzen, I. Zanette, D. Hahn, J. Kenntner, J. Mohr, A. Rack, T. Weitkamp, and F. Pfeiffer. Quantitative x-ray phase-contrast computed tomography at 82 keV. *Optics Express*, 21(4):4155–66, 2013. doi: 10.1364/OE.21.004155.
(Referenced on pages 48, 98.)

World Health Organization. The top 10 causes of death, 2011 (accessed July 18, 2014). URL `http://www.who.int/mediacentre/factsheets/fs310/en/`.
(Referenced on page 83.)

A. Yaroshenko, K. Hellbach, A. O. Yildirim, T. Conlon, M. Bech, A. Velroyen, F. G. Meinel, M. Reiser, S. Auweter, O. Eickelberg, and F. Pfeiffer. X-ray dark-field longitudinal quantitative in vivo study of pulmonary fibrosis in small animals. *Submitted*.
(Referenced on page 96.)

A. Yaroshenko, F. G. Meinel, M. Bech, A. Tapfer, A. Velroyen, S. Schleede, S. Auweter, A. Bohla, A. O. Yildirim, K. Nikolaou, F. Bamberg, O. Eickelberg, M. F. Reiser, and F. Pfeiffer. Pulmonary emphysema diagnosis with a preclinical small-animal x-ray dark-field scatter-contrast scanner. *Radiology*, 269(2):427–33, 2013.
(Referenced on pages 83, 94, 96, 98.)

A. Yaroshenko, M. Bech, G. Potdevin, A. Malecki, T. Biernath, J. Wolf, A. Tapfer, M. Schüttler, J. Meiser, D. Kunka, M. Amberger, J. Mohr, and F. Pfeiffer. Non-binary phase gratings for x-ray imaging with a compact Talbot interferometer. *Optics Express*, 22(1):547–56, 2014. doi: 10.1364/OE.22.000547.
(Referenced on page 96.)

W. Yashiro, Y. Terui, K. Kawabata, and A. Momose. On the origin of visibility contrast in x-ray Talbot interferometry. *Optics Express*, 18(16):16890–901, 2010.
(Referenced on pages 94, 116, 123.)

W. Yashiro, S. Harasse, K. Kawabata, H. Kuwabara, T. Yamazaki, and A. Momose. Distribution of unresolvable anisotropic microstructures revealed in visibility-contrast images using x-ray Talbot interferometry. *Physical Review B*, 84(9):094106, 2011.
(Referenced on page 42.)

I. Zanette, M. Bech, F. Pfeiffer, and T. Weitkamp. Interlaced phase stepping in phase-contrast x-ray tomography. *Applied Physics Letters*, 98(9):094101, 2011.
(Referenced on page 96.)

I. Zanette, M. Bech, A. Rack, G. Le Duc, P. Tafforeau, C. David, J. Mohr, F. Pfeiffer, and T. Weitkamp. Trimodal low-dose x-ray tomography. *Proceedings of the National Academy of Sciences of the United States of America*, 109(26):10199–204, 2012.
(Referenced on page 96.)

G. Zech. Iterative unfolding with the Richardson-Lucy algorithm. *Nuclear Instruments and Methods in Physics Research Section A: Accelerators, Spectrometers, Detectors and Associated Equipment*, 716:1–9, 2013.
(Referenced on page 57.)

B. Zvezdin, S. Milutinov, M. Kojicic, M. Hadnadjev, S. Hromis, M. Markovic, and O. Gajic. A postmortem analysis of major causes of early death in patients hospitalized with COPD exacerbation. *Chest*, 136(2):376–80, 2009.
(Referenced on page 83.)

Appendix A

Options of processing and reconstruction framework

This appendix lists the functionalities and options of the processing and reconstruction chain that was specifically developed for streamlining the raw data acquired at the 'Skyscan 1190' into tomographic volume data.

A.1 Options of processing framework

For better streamlining of the processing from raw stepping data to corrected, ready-to-reconstruct projection data, the user can choose several options when calling the Skyscan-specific processing script:

- Test mode: The user can try the selected options on one defined projection, rather than the whole scan. Display of figures is automatically activated.
- Type of processing: The user can choose between conventional Fourier-transform-based processing of the phase stepping curve or several sine-fit based processing approaches, such as conventional sine fit, statistical phase retrieval (Section 3.3.3.1) or expectation maximization phase retrieval (Section 3.3.3.2).
- Masking: For representative single projection images, the part of the field of view that is not covered by the phase grating can be masked out.
- Cropping: Tomographic reconstruction requires to crop the images to a rectangular phase-sensitive area. The user can choose the default values or enter values that are preferred for the specific sample shape.

- Background region: For background corrections the user can choose between a default background region, a user-defined background region, or an automatically detected region where the sample is not covering the field of view.
- Background correction: Dark-field and absorption images are automatically normalized. Differential phase images can be processed using the (extended) adaptive phase recovery described in Section 3.3.4.
- Gray-value scaling: The gray-value scaling for storing TIFF files can be chosen.
- Image quality test options: For some studies, for example dose vs. image quality estimations, it is handy to be able to change parameters post acquisition. Therefore, options to introduce artificial binning or to skip steps from the phase stepping series were implemented.
- Flatfield use: Flatfield images can be taken either in blocks at certain gantry positions during a tomographic scan or afterwards during a separate tomography. The software allows to randomly choose a flatfield from the nearest block or to interpolate flatfields between neighboring blocks with a distance weight, or to use the separate flatfield tomography, if available.
- Plot results: All processed images, i.e. absorption, differential phase and dark field, can be displayed. Additionally, the phase stepping curve and a visibility map are shown. Optionally, the background correction stages and the used background region can be plotted for investigation.
- Integration: Differential phase projections can be integrated using a regularized integration algorithm (Thüring et al., 2011b).
- Naming: To ensure backwards compatibility, different naming options of the image files produced by the acquisition software can be chosen.

A.2 Options of reconstruction framework

The tomographic reconstruction script, which was tailored to Skyscan data, is callable with various options to optimize image quality of the reconstructed volume:

- Ring removal: Imperfections and locally differing sensitivity of the detector can be a source of severe ring artifacts in the tomographic reconstruction. The usual solution that most microCT manufacturers apply is to shift either

sample or detector by a few micrometers for each projection. The shift distance is logged, so that it can be corrected for before reconstruction. Thereby, the imperfection is no longer concentrated on the same location in the images and does not show up as rings. Since the relative geometry of sample stage, detector and source is fixed, this approach is not feasible in the Skyscan 1190. Instead, a ring removal algorithm can be applied that works as follows: All processed projections of one modality are averaged to gain a mean projection. There, imperfections show up as clear spikes, since they appear always in identical pixels and do not average out. This mean projection is median-filtered with a selectable kernel size and the difference between original mean projection and median-filtered mean projection is subtracted from each projection prior to reconstruction.

- Gaussian blur: Gaussian filtering with selectable kernel size can be applied to smooth noisy images.

- Test mode: Before reconstructing the whole dataset, the script can be run in test mode, which reconstructs only the slice that is fastest to reconstruct, i.e. the slice where no x-ray beam with angular inclination in vertical direction contributed to image formation (often called 'central slice'), using FBP. The test mode automatically turns on the display of the reconstructed slice.

- Output format: The user can choose to save the reconstructed volume as *.tif* and/or *.hdf* files.

- Gray scaling: For TIFF output, the user can select a range of the reconstructed values to map to the dynamic range of TIFF values. Other options are to use default values that may not be optimal for every measured sample, or to automatically scale from minimal to maximal value of a part of or of the full reconstructed volume.

- Center of rotation: Since the scanner geometry is fixed, the center of rotation is automatically calculated from the known geometrical parameters. To account for the case that geometrical changes are applied to the scanner that might slightly alter the position of the rotation axis, the center of rotation can also be set manually or determined visually from a series of test reconstructions.

- Tomoconsistency alignment: To correct for geometrical drifts and uncertainties, the projections can be shifted individually in an automated manner. The original projection and the image reprojected from preliminary reconstructions are compared to each other and consequently relatively shifted. The approach was implemented and described by Allner (2013).

- Corrupt projections: Processed projections that are of minor quality due to too strong instabilities of the system (i.e. detector blackout etc.) can be manually excluded from the reconstruction by just stating their number.
- Angular range: The angular range over which the projections were acquired can be set in the text-based log file. The projections are then evenly distributed between the given starting and ending angle. In principle, this option allows for reconstruction of 180 degree (plus fan angle) scans.
- Reconstruction method: The user can choose between conventional filtered back-projection, with Ramlak or Hamming filter for absorption and dark-field data and Hilbert filter for differential phase data, and statistical iterative reconstruction (SIR). In case of SIR, three parameters (number of iterations, λ_{Huber}, γ_{Huber}) have to be provided, which are discussed in more detail in Section 3.3.5. To facilitate repeated SIR with different parameters to find the optimal parameter for the particular dataset, a batch reconstruction option is included.

List of abbreviations

ADPR	adaptive differential phase recovery
ART	algebraic reconstruction technique
CCD	charge-coupled device
CNR	contrast-to-noise ratio
CT	computed tomography
DEI	diffraction enhanced imaging
DF	dark field
DFCT	dark-field computed tomography
DFI	dark-field imaging
DPC	differential phase contrast
EADPR	extended adaptive differential phase recovery
EM	expectation maximization
ESRF	European Synchrotron Radiation Facility
FBP	filtered backprojection
FDK	Feldkamp-Davis-Kress
FFT	fast fourier transform
FOV	field of view
GBI	grating-based imaging
GPU	graphics processing unit
IR	iterative reconstruction

LS	least-squares
LSF	line-spread function
MRI	magnetic resonance imaging
PC	phase contrast
PCCT	phase-contrast computed tomography
PCI	phase-contrast imaging
PET	positron emission tomography
PMMA	polymethyl methacrylate
PSF	point-spread function
PVA	polyvinyl alcohol
RL	Richardson-Lucy
SART	simultaneous algebraic reconstruction technique
SIR	statistical iterative reconstruction
SIRT	simultaneous iterative reconstruction technique
SNR	signal-to-noise ratio
SPECT	single photon emission computed tomography
SPR	statistical phase retrieval
TIFF	tagged image file format
WLS	weighted least-squares

Publications and scientific presentations

Here, all publications originating from the framework of this doctoral thesis are listed. Moreover, scientific oral and poster presentations are given in chronological order.

First-authored publications (peer-reviewed)

A. Velroyen, M. Bech, A. Malecki, A. Tapfer, A. Yaroshenko, M. Ingrisch, C.C. Cyran, S.D. Auweter, K. Nikolaou, M.F. Reiser, & F. Pfeiffer. Microbubbles as a scattering contrast agent for grating-based x-ray dark-field imaging. *Physics in Medicine and Biology.* 58(4), N37, 2013.

A. Velroyen, M. Bech, I. Zanette, J. Schwarz, A. Rack, C. Tympner, T. Herrler, C. Staab-Weijnitz, M. Braunagel, M.F. Reiser, F. Bamberg, F. Pfeiffer, & M. Notohamiprodjo. X-ray phase-contrast tomography of renal ischemia-reperfusion damage. *PlosOne*, doi:10.1371/journal.pone.0109562, October 2014.

A. Velroyen, A. Yaroshenko, D. Hahn, A. Fehringer, A. Tapfer, M. Müller, P.B. Noël, B. Pauwels, A. Sasov, A.Ö. Yildirim, O. Eickelberg, K. Hellbach, S.D. Auweter, F.G. Meinel, M.F. Reiser, M. Bech, & F. Pfeiffer. X-ray dark-field computed tomography of living mice. *submitted.*

A. Velroyen, M. Bech, A. Tapfer, A. Yaroshenko, M. Müller, P. Paprottka, M. Ingrisch, C.C. Cyran, S.D. Auweter, K. Nikolaou, M.F. Reiser, & F. Pfeiffer. Ex-vivo perfusion-simulation measurements of microbubbles as a scattering contrast agent for grating-based x-ray dark-field imaging. *submitted.*

Co-authored publications (peer-reviewed)

M. Thomsen, M. Poulsen, M. Bech, A. Velroyen, J. Herzen, F. Beckmann, R. Feidenhans'l, & F. Pfeiffer. Visualization of subcutaneous insulin injections by x-ray computed tomography. *Physics in Medicine and Biology.* 57(21), 7191, 2012.

J. Fu, A. Velroyen, R. Tan, J. Zhang, L. Chen, A. Tapfer, M. Bech, & F. Pfeiffer. A reconstruction method for cone-beam differential x-ray phase-contrast computed tomography. *Optics Express.* 20(19), 21512-21519, 2012.

A. Tapfer, M. Bech, A. Velroyen, J. Meiser, J. Mohr, M. Walter, J. Schulz, B. Pauwels, P. Bruyndonckx, X. Liu, A. Sasov, & F. Pfeiffer. Experimental results from a preclinical x-ray phase-contrast CT scanner. *Proceedings of the National Academy of Sciences of the United States of America.* 109(39), 15691-15696, 2012.

M. Bech, A. Tapfer, A. Velroyen, A. Yaroshenko, B. Pauwels, J. Hostens, P. Bruyndonckx, A. Sasov, & F. Pfeiffer. In-vivo dark-field and phase-contrast x-ray imaging. *Scientific Reports*, 3, 2013.

A. Yaroshenko, F.G. Meinel, M. Bech, A. Tapfer, A. Velroyen, S. Schleede, S.D. Auweter, A. Bohla, A.Ö. Yildirim, K. Nikolaou, F. Bamberg, O. Eickelberg, M.F. Reiser, & F. Pfeiffer. Pulmonary emphysema diagnosis with a preclinical small-animal x-ray dark-field scatter-contrast scanner. *Radiology.* 269(2), 427-433, 2013.

F.G. Meinel, F. Schwab, A. Yaroshenko, A. Velroyen, M. Bech, K. Hellbach, J. Fuchs, T. Stiewe, A.Ö. Yildirim, F. Bamberg, M.F. Reiser, F. Pfeiffer, & K. Nikolaou. Lung tumors on multimodal radiographs derived from grating-based x-ray imaging - a feasibility study. *Physica Medica: European Journal of Medical Physics.* 30(3), 352357, 2014.

F.G. Meinel, A. Yaroshenko, K. Hellbach, M. Bech, M. Müller, A. Velroyen, F. Bamberg, O. Eickelberg, K. Nikolaou, M.F. Reiser, F. Pfeiffer, & A.Ö. Yildirim. Improved diagnosis of pulmonary emphysema using in vivo dark-field radiography. *Investigative Radiology.* 49(10), 653-658, 2014.

J. Fu, X. Hu, A. Velroyen, M. Bech, M. Jiang, & F. Pfeiffer. 3D algebraic iterative reconstruction for cone-beam x-ray differential phase-contrast computed tomography. *PlosOne*, doi: 10.1371/journal.pone.0117502, March 2015.

K. Hellbach, A. Yaroshenko, F.G. Meinel, A.Ö. Yildirim, T.M. Conlon, M. Bech, M. Müller, A. Velroyen, M. Notohamiprodjo, F. Bamberg, S.D. Auweter, M.F. Reiser, O. Eickelberg, & F. Pfeiffer. In vivo dark-field radiography for

early diagnosis and staging of pulmonary emphysema. *Investigative Radiology*. In press, 2015.

A. Yaroshenko, K. Hellbach, A.Ö. Yildirim, T. Conlon, M. Bech, A. Velroyen, F.G. Meinel, S.D. Auweter, O. Eickelberg, M.F. Reiser, & F. Pfeiffer. X-ray dark-field longitudinal quantitative in vivo study of pulmonary fibrosis in small animals, *submitted*.

M. Müller, A. Yaroshenko, A. Velroyen, M. Bech, A. Tapfer, B. Pauwels, P. Bruyndonckx, A. Sasov, & F. Pfeiffer. Contrast-to-noise ratio optimization for a prototype phase contrast CT scanner. *submitted*.

Co-authored conference proceedings

M. Bech, A. Tapfer, A. Velroyen, A. Yaroshenko, B. Pauwels, P. Bruyndonckx, X. Liu, A. Sasov, J. Mohr, M. Walter, & F. Pfeiffer. Results from the first preclinical CT scanner with grating-based phase contrast and rotating gantry. *AIP Conference Proceedings (XNPIG)*, 1466, 130-136, 2012.

B. Pauwels, P. Bruyndonckx, X. Liu, A. Tapfer, A. Velroyen, A. Yaroshenko, M. Bech, F. Pfeiffer, & A. Sasov. First small-animal in-vivo phase-contrast micro-CT scanner. *SPIE Proceedings*. 85060J, 2012.

A. Yaroshenko, F.G. Meinel, M. Bech, A. Tapfer, A. Velroyen, S. Schleede, M. Müller, S.D. Auweter, A. Bohla, A.Ö. Yildirim, K. Nikolaou, F. Bamberg, O. Eickelberg, M.F. Reiser, & F. Pfeiffer. Preclinical x-ray dark-field radiography for pulmonary emphysema evaluation. *IEEE 10th International Symposium on Biomedical Imaging (ISBI)*. 370-373, 2013.

A. Yaroshenko, F.G. Meinel, K. Hellbach, M. Bech, A. Velroyen, M. Müller, F. Bamberg, K. Nikolaou, M.F. Reiser, A.Ö. Yildirim, O. Eickelberg, & F. Pfeiffer. Small-animal dark-field radiography for pulmonary emphysema evaluation. *SPIE Proceedings Medical Imaging*. 9033, 2014.

Oral presentations

Preliminary results from a first preclinical x-ray phase-contrast CT scanner, *SPIE Medical Imaging*, San Diego, USA, February 2012.

Preliminary results from a first preclinical x-ray phase-contrast CT scanner, *Frühjahrstagung der Deutschen Physikalischen Gesellschaft (DPG)*, Berlin, Germany, March 2012.

Microbubbles as a scattering contrast agent for x-ray dark-field imaging, *European Congress of Radiology*, Vienna, Austria, March 2013.

Novel results from a first preclinical x-ray phase-contrast and dark-field CT scanner, *IEEE Medical Imaging Conference*, Seoul, South Korea, November 2013.

Novel results from a first preclinical x-ray phase-contrast and dark-field CT scanner, *Annual Meeting Radiological Society of North America (RSNA)*, Chicago, USA, December 2013.

Poster presentations

First results from a preclinical x-ray phase-contrast CT scanner, *CIMST Summer School on Biomedical Imaging*, ETH Zurich, Switzerland, September 2011.

Reconstruction method for differential phase-contrast computed tomography measured in cone-beam geometry, *International Workshop on X-ray and Neutron Phase Imaging with Gratings (XNPIG)*, Tokyo, Japan, March 2012.

In-vitro measurements of microbubbles as a scattering contrast agent for grating-based x-ray dark-field imaging, *2nd Symposium on Biomedical Phase-Contrast Imaging (IMXP)*, Garmisch-Partenkirchen, Germany, January 2013.

In-vitro measurements of microbubbles as a scattering contrast agent for grating-based x-ray dark-field imaging, *Taking X-ray phase-contrast imaging into mainstream applications, Scientific Discussion Meeting, The Royal Society*, London, United Kingdom, February 2013.

Application of novel processing tools to improve the extraction of x-ray differential phase signals from mechanically unstable phase stepping, *European Congress and Exhibition on Advanced Materials and Processes (EUROMAT)*, Sevilla, Spain, September 2013.

Ex-vivo perfusion-simulation measurements of microbubbles as a scattering contrast agent for grating-based x-ray dark-field imaging, *2nd International Workshop on X-ray and Neutron Phase Imaging with Gratings (XNPIG) and 3rd Symposium on Biomedical Phase-Contrast Imaging (IMXP)*, Garmisch-Partenkirchen, Germany, January 2014.

Acknowledgments

The work of this thesis relied in many ways on the support and numerous contributions of others. I would like to express great gratitude to all of them.

First of all, I want to thank my academic supervisor Prof. Franz Pfeiffer for giving me the opportunity to work on such fascinating topics for my doctoral thesis. Thank you for sharing your knowledge on x-rays, providing your guidance, supporting every aspect that was necessary for my work, and for being very generous and encouraging concerning conference and summer school visits. You lay the foundation for the unique work atmosphere at the chair that I enjoyed so much.

I acknowledge and thank Prof. Martin Zacharias for being chairman.

I thank Dr. Martin Bech, my second supervisor, for many enlightening discussions and for patiently answering all my questions. Thank you for sharing your enthusiasm about solving puzzling problems and for always having an open door for me. Thanks for agreeing on being the second official referee of this thesis.

Thank you, Dr. Peter Noël from the Department of Radiology, Klinikum rechts der Isar, for being my official mentor in the framework of the TUM Graduate School, and for actually, and more importantly, being a true mentor. You taught me how the scientific community functions, and I could always talk to you no matter if it was about 'the integral of all errors' or anything beyond that.

My thesis was built on several fruitful collaborations with external people:

From our industrial partner Bruker microCT (formerly Skyscan), I thank Alexander Sasov, Bart Pauwels, Xuan Liu, Peter Bruyndonckx, Faisal Nadeem, and Jeroen Hostens for their dedication to the Skyscan 1190 project, and for their support and their answers to my questions.

I thank Sigrid Auweter and Claudia Staab-Weinjitz for their excellent organization and management of the projects in collaboration with the Institute of Clinical Radiology of the Klinikum Grohadern. Many thanks to the coordinator of the MAP Project Fabian Bamberg and the head of the institute Prof. Maximilian Reiser for

supporting the interdisciplinary collaboration. In the 'bubbles' project, I would like to thank Michael Ingrisch, Philipp Paprottka, Clemens Cyran, and Konstantin Nikolaou for input, discussions, materials, experimental work and proofreading the paper drafts. In the 'kidney' project, I thank Mike Notohamiprodjo for close collaboration on the data analysis and for writing the manuscript with me, Manuel Kolb for his help with the segmentation, and Christiane Tympner and Tanja Herrler for performing the histology. In the 'lung' project, I am very grateful to Katharina Hellbach for performing the experiments together with Andre, for her advice on the data analysis, and for scanning the histological sections. I thank Felix Meinel for initiating and planning the project, and Oliver Eickelberg and Önder Yildirim from the Helmholtz Zentrum for designing the study with us and for providing the mouse model.

I would like to thank the crew from the Karlsruhe Nano Micro Facility, a Helmholtz Research Infrastructure at Karlsruhe Institute of Technology, for support concerning the gratings necessary for the experiments in this thesis.

During my time at E17, I went to several beamtimes. I want to express my gratitude to the local support at the respective beamlines. I thank Irene Zanette, Alexander Rack, and Timm Weitkamp for help with the experiments at ID19 at the ESRF, Grenoble. Thanks also to Julia Herzen and Felix Beckmann from the Helmholtzzentrum Geesthacht for their guidance and support at the W2 (HARWII-II) beamline of DESY, Hamburg.

Regarding the contrast agent project, I thank Katrin Suppelt from Visualsonics, for providing the Vevo MicroMarker vials and for valuable advice on their handling. I thank Dr. Lars Dähne, Moritz Klickermann and Dr. Gabriella Egri from Surflay Nanotec GmbH, for performing size and concentration measurements of the PVA microbubbles and for their valuable advice and helpful answers to my numerous questions. Thanks to Åsa Barrefelt from the Karolinska Institute, Stockholm, for answering my questions on animal experiments with PVA bubbles.

I want to thank the whole E17 group for making me feel like being among friends rather than just colleagues. You all contribute to the great atmosphere at work by always being cooperative, supportive, and friendly. I enjoyed very much our group activities, such as the BBQs, dinners at Dieter's place, Christmas parties, seminar days etc. In the following, I would like to express my gratitude to some people in particular.

As part of the Triple-A-Double-M Team, I want to thank Arne, Andre, Mark and Martin B. for their concerted effort and dedication to get the best possible results from the scanner. Especially, I want to thank you, Arne, for bringing me into the group, for sharing your knowledge and thoughts on many things with me, and for

being a good friend.

This work is built on many lines of code written by other people at E17. Thank you for your work! I have to thank in particular Andreas M. for the simulations, Dieter H. for the iterative reconstruction (and the LaTeX template and cover design), Guillaume for the EM algorithm, and Andreas F. for the projectors. I also would like to thank Pierre Thibault for code and thoughts on the still unresolved iodine puzzle.

Since nothing would work without them, I am very grateful to Martin D., Dieter H., Andreas F., Sebastian A., Björn, and all the others that keep the IT infrastructure at the chair running and patiently helped me with any computer-related problems.

I want to thank Nelly and Klaus for their support in all administrative and organizational issues, and Hans and Rudi for their craftsmanship.

I shared many, many informative, funny, and absurd coffee breaks and discussions with my direct, next-door, and virtual office mates. They often made my day, so that I always liked to come to the office, even at times when projects could be frustrating. Thank you Alex, Andreas F., Arne, Barbara, Björn, Dieter H., Julia, Kai, Lorenz, Maite, Marco, Marian, Martin D., Mathias, Michael E., Sebastian A., Sebastian E., Thomas G., and all the others. With many of you I also had a lot of fun partying and sharing some memorable 'last beers at Barschwein' — thank you for those great times!

There are three people among my colleagues that I grew very close friends with during the years, namely Marian, Michael E., and Julia. Thank you for all the good times, adventures, travels, sushi, Soju, Mexikaner, Thalis, Tapas, coffees, shishas, chats, wellness, taxi rides, HipHop dances, sleepless nights, and hungover days we shared, and for enduring the tough moments together with me. Thank you that I could – and can – always count on you.

I want to thank my sister Helga for reviewing my code, for providing the recreational cats, and – most importantly – for listening when I was again convinced to have chosen the wrong subject of study. Thank you for being there for me. Ich möchte meinen Eltern dafür danken, dass sie mich mein Leben lang in jeder Hinsicht unterstützt haben, und insbesondere dafür, dass sie mein Studium inklusive Ortswechsel nach München ermöglicht haben.

I thank my love and my partner Matthias for being at my side all those years. You gave me support and freedom at the same time, and you made me stronger.